**University of Mohamed Khider – Biskra**

**Faculty of Exact Sciences and Science of Nature and life**

جامعة محمد خيضر ـ بسكرة

كلية العلوم الدقيقة

و علوم الطبيعة

و الحياة

Thesis presented to obtain the degree:

**Doctorat LMD**

Option**:**

**Physics of semiconductors**

Entitled:

# Study of Schottky diodes based on ultrawide-band gap semiconductors

Presented by:

**Labed Madani**

In front of the jury composed of:

| | | | |
|---|---|---|---|
| Meftah Amjad | Professor | U.M.K. Biskra | President |
| Sengouga Nouredine | Professor | U.M.K. Biskra | Supervisor |
| Rim You Seung | Professor | Sejong University | Co-Supervisor |
| Meftah Afak | Professor | U.M.K. Biskra | Examiner |
| Oussalah Slimane | Professor | CDTA research center Algiers | Examiner |

# Acknowledgement

Firstly, I would like to express my deepest gratitude to my supervisor Professor **Nouredine Sengouga** for his valuable guidance, support, motivation and for his patient during my PhD.

Also, my sincere thanks also to my co-supervisor Professor **You Seung Rim** for his support and motivation during my PhD.

I would also like to thank Professor **Afak Meftah** for her support and motivation.

I express my sincere gratitude and appreciation to my reading committee members, Professor **Meftah Amjad**, Professor **Oussalah Slimane**, and Professor **Meftah Afak** for their precious time to read my thesis and for accepting to judge it

Without forgetting, I would like to thank members of LMSM Lab headed by Professor **Toufik Tibermacine.**

Last but not the least, I would like to thank **my parents** for their love and patience.

## **Dedication**

I dedicate this work to the best parents "**Miloud**" and "**Zahia**".

# ملخص

في هذه المذكرة, تمت دراسة نوعين من ديود شوتكي نيكل/أكسيد الغاليوم احدهما مرسب بواسطة طريقة الرش القائم على المجال المغناطيسي المحصور (confined magnetic field based sputtering) وأما الاخر تم ترسيبه باستعمال التبخير بواسطة حزمة الكترونية (Electron-beam evaporation). في كلتا الحالتين أستعمل سيلفاكو لنمذجة القياسات التجريبية. أولا تم اقتراح نموذج لنمذجة انتشار ذرات النيكل في سطح أكسيد الغاليوم. في هذا النموذج ذرات النيكل تعوض ذرات الغاليوم و النتيجة تشكل مركب جديد و الذي هو $(Ni_xGa_{1-x})_2O_3$. هذا المركب لديه فاصل طاقي و ألفة الكترونية تختلف عن أكسيد الغاليوم, انتشار ذرات النيكل يؤدي الى تحيين فجوات الغاليوم مما يؤدي الى انخفاض تركيز العيوب السطحية. توافق جيد بين المحاكاة و القياسات التجريبية للتيار المباشر و العكسي مع اعتبار نموذج النفق من عصابة الى عصابة (BBT) و أثير تأين الذرات عند الاستقطاب العكسي (impact ionization). هذا التوافق الجيد بين المحاكاة و القياسات عند درجات الحرارة المرتفعة و المنخفضة تأكد فعالية النموذج المقترح. كذلك تم دراسة الديود شوتكي عند درجات حرارة مختلفة. عند درجة حرارة الغرفة خصائص الديود تميل عن القيم المثالية, هذا راجع بالدرجة الاولى الى تأثير العيوب الناتجة عن البلازما و القذف بذرات الارغون (Ar). التناقص في حاجز شوتكي($\phi_B$) و جهد العتبة ($V_{Th}$) بزيادة درجة الحرارة يعود الى التوزيعة الغوصية لحاجز شوتكي. زيادة معامل المثالية مع زيادة درجة الحرارة راجع لزيادة المقاومة على التسلسل و زيادة هذه الاخيرة يعود لزيادة مقاومة الطبقة $(Ni_xGa_{1-x})_2O_3$ المشكلة و زيادة مقاومة النيكل. عند درجة الحرارة المنخفضة, معامل المثالية الذي تم الحصول عليه من التيار الاجمالي يقارب 6.04. بينما قيمته المثالية تقارب 1.04 اذا تم استخراجه من مركبة تيار الفعل الحراري فقط. بعد دراسة هذا الديود تم اقتراح جملة من التحسينات منها ادراج طبقة بينية بين النيكل و أكسيد الغاليوم و ايضا استعمال أكسيد التيتانيوم ($TiO_2$) كطبقة سطحية للتقليل من تأثير الحقول العالية في حواف الديود و انتقالها للحامل (Substrate) بعيدا عن السطح. أخيرا تمت دراسة ديود شوتكي متحصل عليه باستعمال طريقة التبخير بحزمة الكترونية و استخراج الخصائص السطحية لهذا الديود والتي هي تركيز العيوب البينية, الالفة الالكترونية و دالة العمل لمعدن النيكل , هذه الدراسة لغرض دراسة تأثير اضافة طبقة الغرافين على التيار الكهربائي للديود لانه من المعلوم تأثر الغرافين بالبلازما و ذرات الارغون و هاذين الاخرين عنصران أساسيان في طريقة الرش القائم على المجال المغناطيسي المحصور لهذا اخترنا طريقة التبخير بحزمة الكترونية. وفي الاخير النتيجة كانت زيادة حاجز شوتكي بزيادة الفاصل الطاقي و دالة العمل للغرافين, هذه النتيجة تثبت امكانية التحكم في قيمة حاجز شوتكي من خلال التحكم في خصائص طبقة الغرافين.

# Abstract

In this thesis, Ni/β-Ga$_2$O$_3$ Schottky barrier diodes (SBDs) deposited by confined magnetic field based sputtering (CMFS) and Electron-beam evaporation (EBE), are modelled using SILVACO-Atlas and compared to experimental measurements. Firstly, Forward and reverse current of CFMS SBDs were studied. A model was developed to understand the role of Ni atoms diffusion in the surface of β-Ga$_2$O$_3$. In this model, Ni out diffusion combines with oxygen to form a new $(Ni_xGa_{1-x})_2O_3$ interfacial layer. This new compound is modelled as a semiconductor with different energy gap and affinity and less defects since Ni diffusion compensates Ga vacancy related defects. A good agreement between simulation and measurement for forward at high and low temperatures and reverse current with the consideration of band-to-band (BBT) and impact ionization for the reverse current. The achieved agreement demonstrates the soundness of the proposed model. In addition, temperature dependent SBD characteristics were studied. At room temperature, the deviation of SBD parameters from the ideal case is due to the effect of interfacial states due to plasma and Ar bombardment. It was found that the Schottky barrier height ($\phi_B$) and threshold voltage ($V_{Th}$) decrease with increasing temperature. However, the ideality factor (η) increases, this is related to the series resistance (R$_S$) increase. The R$_S$ increase is related to the $(Ni_xGa_{1-x})_2O_3$ and Nickel resistance increase with increasing temperature. At low temperature, an ideality factor of 6.04 was obtained from the total current. However, it was about 1.04 when extracted from the thermionic current component only. Then, optimizations based on the insertion of an undoped layer with different thicknesses at the interface between Ni and Si-doped β-Ga$_2$O$_3$SBD, and insertion of TiO$_2$ edge termination layer. These optimizations lead to displace the highest electric field at corners to the bulk and this means that the breakdown occurs away from the surface of the Schottky diode were studied. Finally, the E-beam SBD was studied. The interfacial properties of this SBD were extracted which are interfacial traps densities, surface electron affinity and Ni workfunction from modelling and comparison to measurements. An optimization is carried out by a graphene layer insertion between Ni and Si-doped β-Ga$_2$O$_3$ since in this deposition method no exposition to plasma and Ar atoms is used. Therefore the graphene layer is not damaged unlike in the CMFS deposition where the device is exposed to Ar and plasma. It was found $\phi_B$ systematically increased with the increase graphene bandgap and workfunction; these results demonstrate the possibility to control $\phi_B$ in a wide range by manipulating graphene properties.

**Table of Contents**

# List of figures

## List of tables

# Introduction

Wide bandgap compound semiconductors made a huge advance and extended functionality of both electronic and optoelectronic devices due to their high voltage operation, fast switching behaviour, and thermal stability [1,2]. Wide bandgap materials, such as GaN, InGaN and SiC were used in many applications in the last decade, in particular nitrides. Nowadays, research has concentrated on ultra-wide bandgap (UWBG) semiconducting materials of which the energy gap exceeds 4 eV [3]. There are several UWBG materials that attract particular attention, including AlGaN, AlN, diamond, and $\beta$-Ga$_2$O$_3$ [3]. $\beta$-Ga$_2$O$_3$ has excellent undoped properties such as a wide bandgap of ~4.8 eV, a high breakdown electrical field of ~8 MV/cm and a high saturation velocity of $1 \times 10^7 \, cm/s$ [3,4,5]. It is also a low cost and a large scale produced material compared to GaN, InGaN and SiC [3,5]. However, this material has a serious drawback of developing p-type [6,7], thus hindering its application in bipolar devices (p-n junction, BJT) [5]. Currently $\beta$-Ga$_2$O$_3$ is therefore mainly used in unipolar devices such as SBD [3,8], MOSFET [2], TFT [9] and field emission [10]). For SBDs (Schottky Barrier Diodes), high work function metals are required for Schottky contact with $\beta$-Ga$_2$O$_3$ [11] such as Nickel [12] and Platinum [13]. For metal deposition, electron beam evaporation (EBE) technique is commonly used. Usually before metal deposition for the Schottky contact, the $\beta$-Ga$_2$O$_3$ surface is etched. This operation is rendered difficult by the high strength of the $\beta$-Ga$_2$O$_3$ bond. Argon bombardment and plasma provide an enhanced physical etching quality, but also tend to introduce surface damage of $\beta$-Ga$_2$O$_3$ [4,14]. SBD degradation is therefore related to surface defects formed during etching. Kim et al [1] used confined magnetic field based sputtering (CMFS) method for Nickel deposition in SBDs which showed less degradation and high performance than their EBE counterparts which were related to the diffusion of Nickel atoms in the surface of $\beta$-Ga$_2$O$_3$ to reduce defects. In CMFS, plasma and Ar bombardment are simultaneously realized in contrast to EBE where plasma and Ar bombardment are separate processes.

In this Thesis, Ni diffusion in the surface of $\beta$-Ga$_2$O$_3$ in CMFS is numerically modelled as a defect layer (DL) made of combination of NiO and $\beta$-Ga$_2$O$_3$ (($Ni_xGa_{1-x})_2O_3$). The formation of $(Ni_xGa_{1-x})_2O_3$ is justified by checking the XPS depth profiling. This DL has different properties than $\beta$-Ga$_2$O$_3$ (defects, band gap and affinity). DL properties (thickness, defect content, band gap and affinity) effect on the electrical characteristics of Ni/$\beta$-Ga$_2$O$_3$ SBD was studied. To achieve this, numerical simulation is used

and the SBD characteristics are evaluated taking into account the proposed model. Then, we propose a new consideration of leakage models in β-$Ga_2O_3$ including band to band transport model (BBT) and the inversion layer formation between Ni and (001) $β\text{-}Ga_2O_3$ under high reverse voltage. The BBT model associated with the Selberherr's Impact ionization (SELB) model usually used for avalanche breakdown, gives good agreement with current-voltage measurement. Furthermore, optimizations of the leakage current, breakdown voltage and specific on-resistance are carried out with the insertion of an undoped $β\text{-}Ga_2O_3$ layer at the interface between Ni and Si-doped β-$Ga_2O_3$, and by adopting a $TiO_2$ insulator plate as edge termination. Improving and controlling Ni/β-$Ga_2O_3$ Schottky barrier height is achieved based on inserting a graphene layer at Ni/β-$Ga_2O_3$ interface and the outputs of the SBD are achieved by manipulating tunneling rate in the graphene layer by tuning the bandgap and the workfunction of the inserted graphene layer.

This thesis is organized as follows:

**Chapter 1** presents and discusses the electrical, optical, and electronic properties of β-Ga₂O₃ thin and thick films.

**Chapter 2** discuses β-Ga₂O₃ Schottky barrier diode technological developments and challenges.

**Chapter 3** presents Ni/β-Ga₂O₃ Schottky barrier diode fabrication and physical models for this device.

**Chapter 4** gives an overview on the software used in this thesis (SILVACO TCAD).

**Chapter 5** presents the results and the discussion of modeling CMFs and EBE SBD based on β-$Ga_2O_3$.

# Chapter 1:
# β-Ga$_2$O$_3$ material properties

## 1.1. Introduction

The aim of this chapter is to discuss the electrical, optical, and electronic properties of β-Ga₂O₃ thin and thick films, in addition to β-Ga₂O₃ Schottky barrier diode technological developments and challenges.

## 1.2. Polymorphs and crystal structure of Ga₂O₃

There are several polymorphs of $Ga_2O_3$, which were investigated in detail both experimentally and theoretically by many researchers including Roy at al.[15], Zinkevich and Aldinger[16], Penner et al.[17], Playford et al. [18], Yoshioka et al. [19], Bosi et al. [20], Delgado et al. [21] and Cora et al.[22]. Although as many as six polymorphs (α, β, γ, δ, ε, and κ) having different crystallographic systems has been reported for $Ga_2O_3$ as presented in **Table 1.1,** there are likely only four polymorphs: α, β, γ, and (δ/ ε/ κ). The δ-phase could be a mixture of β and ε phases, according to Playford et al. [18,23], while the ε phase is likely resembling the κ phase due to rotation grains formed on sapphire, as shown by Cora et al. [22].

# Chapter 1: β-Ga₂O₃ material properties

**Table 1. 1 Ga₂O₃ polymorphs and crystal structures.**

| Polymorph | System | Lattice parameters (Å) | Ref |
|---|---|---|---|
| α | Hexagonal | a=4.9825 | [24] |
| | | b=13.433 | |
| β | Monoclinic | a=12.214 | [3] |
| | | b=3.0371 | |
| | | c=5.7981 | |
| | | β=103.83 | |
| γ | Cubic | a=8.22 | [25] |
| δ | Cubic | a=9.491 | [19] |
| ε | Hexagonal | a=2.9036 | [18] |
| | | b=9.2554 | |
| κ | Orthorhombic | a=5.0463 | [22] |
| | | b=8.7020 | |
| | | c=9.2833 | |

Among the polymorphs, β phase is the most thermodynamically stable and can be grown directly from melt. **Figure 1.1** shows bulk β-Ga$_2$O$_3$ crystals obtained from melt by methods Optical Float Zone, Edge Fed Defined Growth, Czochralski, and Vertical Bridgman. The melting point of β-Ga$_2$O$_3$ is about of 1793 °C. The formation energy of the polymorphs have the following order β < ε < α < δ < γ [19].
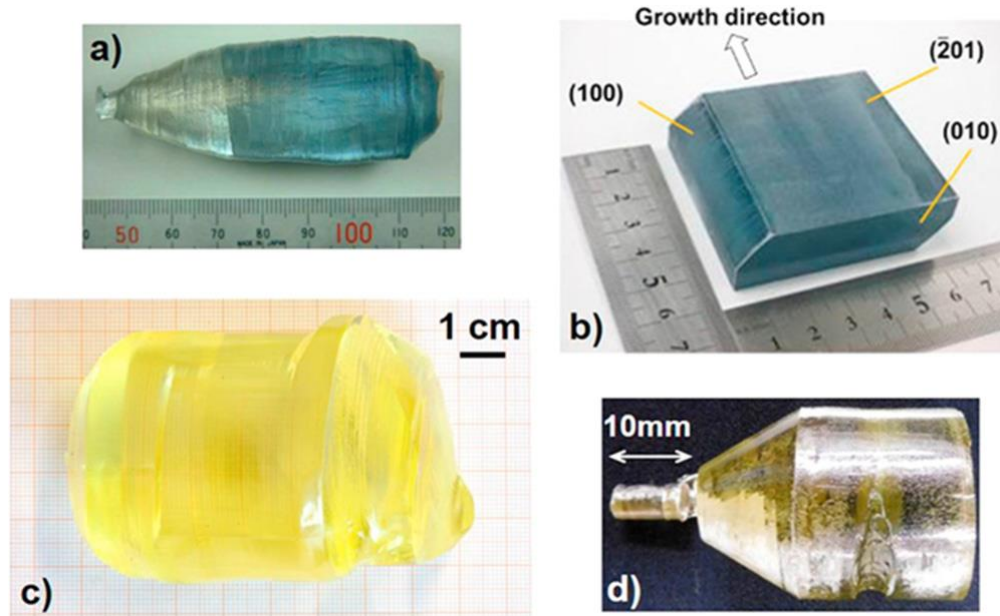
**Figure 1.1 Bulk β-Ga₂O₃ crystals obtained from the melt by the following methods: (a) Optical Float Zone, (b) Edge Fed Defined Growth, (c) Czochralski, and (d) Vertical Bridgman** [2].

Although other phases cannot be grown as bulk crystals from melt, flux or gas phase, they could be obtained as thin films or thick layers. For instance, $\alpha$-Ga$_2$O$_3$ phase was obtained on sapphire substrates by mist Chemical Vapour Deposition (mist-CVD) [26] (at 430- 470 °C), Halide Vapour Phase Epitaxy (HVPE) [27] (at 520- 600 °C) and Laser Molecular Beam Epitaxy (LMBE) [28]. Thin films of the $\gamma$-Ga$_2$O$_3$ phase were obtained by mist-CVD [29] (at 390- 400 °C) and Pulsed laser Deposition (PLD) [30] with the use of sapphire and spinel substrates. $\varepsilon$-Ga$_2$O$_3$ thin films were grown by HVPE on nitride. However, thin films growth of $\delta$-Ga$_2$O$_3$ phase has not been reported so far. As mentioned above, most stable and studied is the β-phase. Also all phases can be transformed into β-phase when annealed at high temperatures or other treatments. $\alpha$-Ga$_2$O$_3$ phase converts to β- Ga$_2$O$_3$ over 650 °C [22]. It was also demonstrated that epitaxial $\varepsilon$-Ga$_2$O$_3$ is relatively stable and converts to β-phase after prolonged annealing at T > 700- 800 °C [22] and Phase transition from $\gamma$ to β phase when it is treated at 750 °C for 3h [31]. Also $\alpha$-Ga$_2$O$_3$ is transformed into β phase when the calcination temperature increased from 400 to 800 °C [32]. When temperature increased up to 950 °C, a sudden and quick transformation from $\kappa$ to β phase occurs [23]. Other works studied these transformations to the β-phase and to other phases which are summarized in **Figure 1.2**. Hence, these transformations of most phases to β-phase explain the interest of researchers in this phase.

# Chapter 1: β-Ga₂O₃ material properties

β-Ga$_2$O$_3$ as mentioned above can be grown as bulk crystal and thin films. HVPE technique is used to grow β-Ga$_2$O$_3$ films heteroepitaxially by Oshima et al. [33] and Okur et al. [3,34] on Al$_2$O$_3$(0001), and homoepitaxially by Nomura et al. [35], Murakami et al. [36], Konishi et al. [37] and Thieu et al. [38] on β-Ga$_2$O$_3$ (001) substrates. Metal Organic Chemical Vapour Deposition (MOCVD) and Metal Organic Vapour Phase Epitaxy (MOVPE) were used to grow β-Ga$_2$O$_3$ films heteroepitaxially and homoepitaxially. In addition, CVD and mist-CVD are used for β-Ga$_2$O$_3$ deposition.There are also many attempts to deposit β-Ga$_2$O$_3$thin film using sol-gel techniques. For example Kokubun et al. [39] deposited thin films of β-Ga$_2$O$_3$ on (0001) sapphire substrate, but a polycrystalline film were formed at heat-treatment temperatures above 600°C. Ohya et al.[40] deposited Ga$_2$O$_3$ thin film on heat resistant glass by dip coating, the films were crystallized as β-Ga$_2$O$_3$ phase by heating at 700°C. However, the resistivity of the film was about $10^7$ Ω cm.
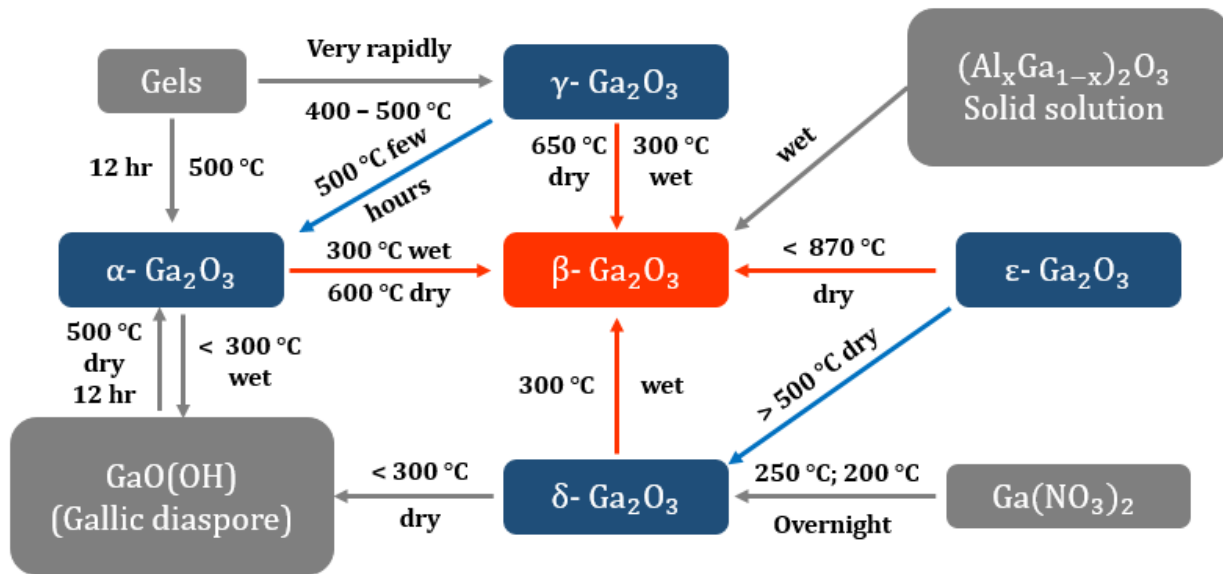


**Figure 1.2 Transformations of Ga₂O₃ crystalline phases and their conditions** [41].

In most works, β-Ga$_2$O$_3$ crystallizes in the base-centred monoclinic system. The unit cell as presented in **Figure 1.3** contains 20 atoms consisting of crystallographically inequivalent Ga$^{+3}$ and O$^{-2}$atoms. In this low symmetry structure Ga atoms are coordinated tetrahedrally and octahedrally (Ga1 and Ga2, respectively), while O atoms are coordinated three and fourfold (O1/O3 and O2, respectively). O1 shares two bonds with Ga2 and one bond with Ga1, O2 shares three bonds with Ga2 and one bond with Ga1, while O3 shares two bonds with Ga1 and one bond with Ga2. The lattice parameters of β-

Ga$_2$O$_3$ are listed in **Table 1.1.** There are two easy cleavage planes: the (100) plane formed by O3 atoms and (001) plane formed by O1 atoms[42,43].
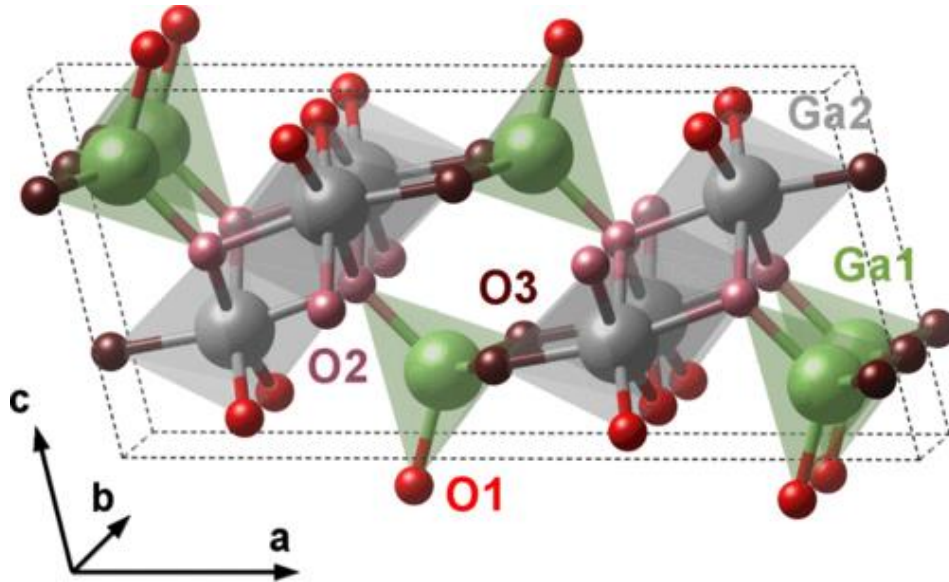


**Figure 1.3 Unit cell of β-Ga₂O₃. Gallium atoms Ga1 and Ga2 are coordinated tetrahedrally and octahedrally, respectively. Inequivalent O atoms have threefold (O1 and O3) and fourfold (O2) coordination** [42,44]**.**

## 1.3. Electronic band structure of β-Ga₂O₃

The electronic band structure defines intrinsic electrical and optical properties of a material hence the knowledge of which enables to conclude a proper device design with a desired functionality. Computational studies may provide hints to experimental research and explore structural, electronic and optical properties, such as trapping effect, intrinsic defects, doping, conductivity type, energy gap and its nature, and optical transitions, as well as material limitations. On the other hand, experimental results may validate a mathematical model for electronic structure. In the last decade, the electronic band structure of β-Ga$_2$O$_3$ was a subject of an intensive computation and measurements by Mohamed et al. [45], Yamaguchi [46], He et al. [47], Furthmüller et al. [48],Varley et al. [49–51], Zhang et al. [52] and other works. The band structure of β-Ga$_2$O$_3$ is shown in **Figure 1.4**. The top of the valence band (VB) is composed mainly by O$_{2p}$ states, which make it very flat. Very small dispersion of the VB maximum (VBM) results in a very high effective hole mass and consequently in a very low hole mobility making a possible p-type conductivity impractical [3]. β-

$Ga_2O_3$ can be regarded as a direct band gap semiconductor and the experimental bandgap is 4.8 ~ 4.9 eV [53].
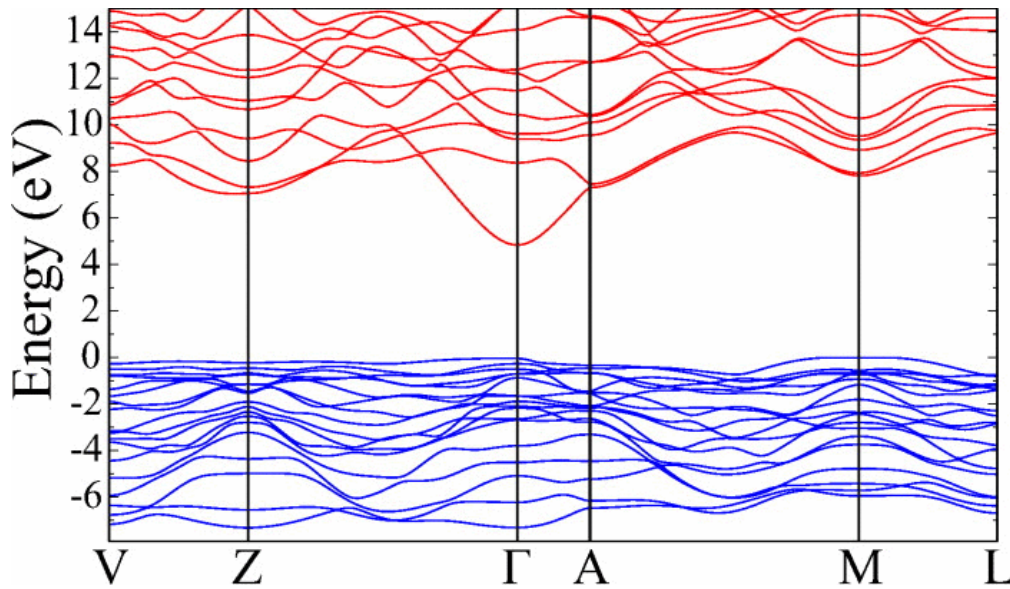


**Figure 1.4 β-Ga₂O₃ band structure calculated using the primitive unit cell of base-centered monoclinic**[49]**.**

## 1.4. Electrical properties

Electrical properties of β-$Ga_2O_3$ constitute a key factor in defining the operation and functionality of a fabricated electronic device, therefore their exploration and understanding is of high importance. These properties include all features that affect the flow and control of the electrical current. They may have either extrinsic (e.g. impurities and dopants) or intrinsic (e.g. crystal structure, electronic band structure) nature. This section discusses basic electrical properties of β-$Ga_2O_3$ bulk crystals and epi-layers. They include such properties as free electron concentration, electron mobility and its limit, and deep traps. Some of the properties are shown for as-grown materials and annealed, at room temperature and temperature-dependent.

## Chapter 1: β-Ga₂O₃ material properties

### 1.4.1. Free electron concentration, Hall mobility, and resistivity

The origin of the electrical conductivity of β-Ga$_2$O$_3$ was intensively studied in the case of both bulk crystals and layers. Experimental results revealed a decrease of the conductivity with oxygen partial pressure in a growth or annealing system. On the other hand, insufficient oxygen concentration lad to an increase of the electrical conductivity. Numerical and experimental studies showed that oxygen vacancies act as deep donors, which cannot directly contribute to the electrical conductivity. Instead, interstitial hydrogen or hydrogen-gallium vacancy complexes were found as shallow donors. Additionally, some tetravalent ions, i.e. Si, Sn and Ge have been proved theoretically and experimentally to form shallow donor states. The underlying electrical conductivity of β-Ga$_2$O$_3$ seems to have a multiple origin, such as native defects resulting from growth conditions (growth method, temperature and atmosphere), residual impurities (always present) and intentional doping. The electrical state of β-Ga$_2$O$_3$ relates firstly to whether the material is layer or bulk crystals, and related to the deposition methods and experimental conditions. For bulk β-Ga$_2$O$_3$, the crystals obtained by Verneuil method were electrically insulating when grown under oxidizing conditions and semiconducting under reducing conditions, and the obtained free electron concentration and Hall mobility at room temperature were $1 \times 10^{18} cm^{-3}$ and $80\ cm^{-3}V^{-1}s^{-1}$, respectively, but when annealed at high temperature for several hours at oxidizing conditions the semiconducting crystals turned into the insulating state[54].

Ueda et al.[55] demonstrated the strong dependent of conductivity of β-Ga$_2$O$_3$ crystals obtained by optical floating zone method on the O$_2$/N$_2$ratio in the growth atmosphere, and the crystals were electrically insulating when obtained under pure O$_2$. The maximum conductivity measured was $38\ \Omega^{-1}cm^{-1}$, with the electron concentration of $5 \times 10^{18} cm^{-3}$.

In contrast, Galazka et al. [3,56] demonstrated a surface insulating formation when the crystals grown with Czochralski and annealed at high temperature (≥ 1000 °C) in oxidizing atmosphere but the bulk remains semiconducting as presented in **Figure 1.5** and the electron mobility is in principle unchanged. On the other hand, annealing of as-grown crystals in the presence of H$_2$ for 10 h does not affect the free electron concentration after annealing at temperatures up to 900°C, at which a strong decomposition precedes. However, after annealing in the presence of H$_2$ those samples, which were previously annealed in O$_2$ at 1000 °C for 20 h, the electron concentration increases to the same values as that of as-grown crystals after annealing at temperatures 300 – 700°C. After annealing at

temperatures above 700 °C, the electron concentration decreases, again by about one order of magnitude as **Figure 1.5** shows. Annealing in the presence of $H_2$ has a high impact on the Hall mobility, which gradually decreases or increases with annealing temperature depending on whether the crystal samples were as grown or previously annealed in the presence of $O_2$. In addition, the free electron depends on the doping concentration of bulk $\beta\text{-Ga}_2O_3$, for example, Villora et al. [57] revealed a linear dependence of the free concentration on the Si doping concentration as presented in **Figure 1.6.**
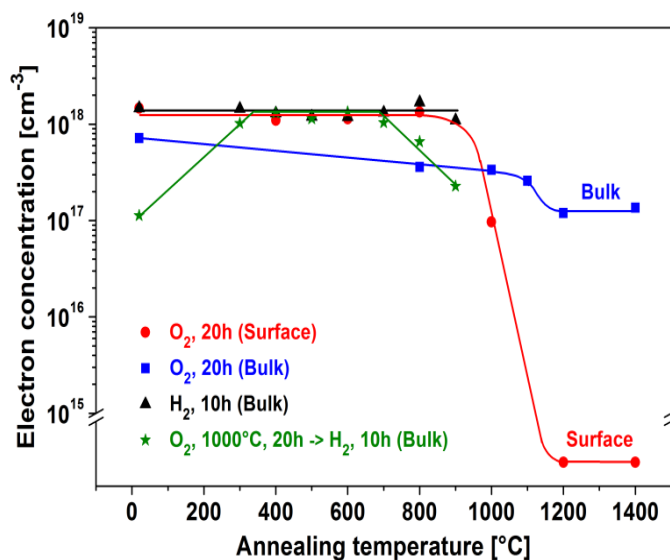


**Figure 1.5 Free electron concentration of Czochralski-grown β-Ga₂O₃ crystals as a function of annealing temperature and atmosphere** [3].
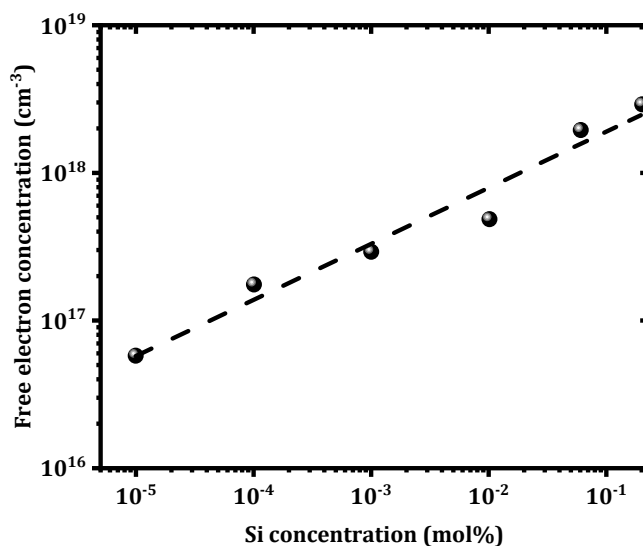


**Figure 1.6 Free electron concentration as a function of a nominal Si concentration** [3,57].

# Chapter 1: β-Ga₂O₃ material properties

In contrast to bulk crystals, the hetero- and homoepitaxially grown layer with no intentional doping have typically very high resistivity ($\geq 10^6 \Omega$.cm) and such layers can be regarded as electrical insulators. To enhance the conductivity, an intentional doping with shallow donors (typically $Sn^{+4}$ and $Si^{+4}$) was used, of in most deposition methods, the common feature of such layers is low electron mobility, which could be measured only at very high dopant concentration and a peak mobility of about 40 $cm^2V^{-1}s^{-1}$ was measured at doping concentration above $1 \times 10^{18} cm^{-3}$. Even so, homoepitaxial layers grown on (100) substrate showed very poor electrical properties, and different models developed to explain the reason for this behaviour. The model developed by Schewski et al.[58] for understanding the insulating nature of the deposited layer using MOVPE on (100) substrate, stated that the poor electrical properties are related to planar defects in the form of twin lamellae in addition to the surface morphology which is characterized by the three dimensional islands. They found the enhancement of the electrical properties with increasing miscut-angle of the substrate due to the density of twin lamellae decreases with increasing miscut-angle of the substrate up to 6° towards (001) [42,58]. This effect does not occur in (010) and (001) orientations, indeed, homoepitaxial growth of β-Ga₂O₃ layers on (010) and (001) native substrates exhibited electrical properties similar to that of bulk crystals, independent on epitaxial growth method and dopant type. The summary of basic electrical properties of homoepitaxial β-Ga₂O₃ layers grown on (010) native substrates is presented in **Table 1.2**.

**Table 1.2 Basic electrical properties of homoepitaxial β-Ga₂O₃ layers grown on (010) substrates [3].**

| Epitaxial technique | Dopant | Concentration ($cm^{-3}$) | Mobility ($cm^2.V^{-1}.s^{-1}$) |
|---|---|---|---|
| MOVPE | Si | $1 \times 10^{17}$ - $8 \times 10^{19}$ | 50 - 130 |
|  | Sn | $4 \times 10^{17}$ - $8 \times 10^{19}$ |  |
| MBE | Sn | $2 \times 10^{16}$ - $8 \times 10^{19}$ | 120 |
| MBE | Sn | $1 \times 10^{17}$ - $8 \times 10^{18}$ | 10 - 80 |
| CVD | Si | $1.2 \times 10^{18}$ | 72 |
| Mist-CVD | Sn | $1 \times 10^{18}$ - $5 \times 10^{20}$ | 10 - 45 |
| PLD | Si | $2.6 \times 10^{19}$ - $1.7 \times 10^{20}$ | 19 - 27 |

### 1.4.2. Native deep traps in β-Ga₂O₃

Native point defects in $\beta$-$Ga_2O_3$ are Ga vacancies ($V_{Ga}$) at tetrahedral (Ga1) and octahedral (Ga2) sites as well as oxygen vacancies at threefold coordinated sites (O1 and O2) and fourfold coordinated sites (O3). The calculated oxygen vacancy ($V_O$) formation energies are 3.31, 2.7 and 3.57 eV for O1, O2, and O3, respectively, leading to a conclusion that they are deep donors and do not directly contribute to the electrical conductivity. Oxygen vacancies occur as neutral ($V_O$) and double ionized vacancies ($V_O^{\bullet\bullet}$) with $V_O$ dominating at low oxygen partial pressure, P(O$_2$), up to 0.01 bar, and their concentration decreases with P(O$_2$). On the other hand, $V_{Ga}$ form deep levels at 1.62 and 1.83 eV below the conduction band minimum (CBM) for $V_{Ga1}$ and $V_{Ga2}$, respectively, and act as deep acceptors. Moreover, $V_{Ga}$ concentration increases with P(O$_2$) leading to a conductivity compensation. The calculations show that intrinsic defects alone cannot be responsible for the electrical conductivity of $\beta$-$Ga_2O_3$. However, the situation dramatically changes in the presence of intentional dopants or residual impurities.

Deep traps in $\beta$-$Ga_2O_3$ depend on the deposition method and experimental conditions, but the deep level E$_2$ was present in all measured samples and in the most cases, it was a dominating trap with a concentration between $1\times10^{13}$cm$^{-3}$ and $1\times10^{14}$cm$^{-3}$ , this trap is at 0.75 eV below the conduction band minimum. On the origin of this trap level, Ingebrigtsen et al.[59] found an extrinsic origin, associated with Fe$^{+3}$impurities substituting Ga$^{+3}$ in the crystal lattice. Other, less frequent traps are E$_3$ and E$_4$ with comparable concentration to E$_2$ and an energy level 1.04 eV and 1.48 eV below the conduction band minimum respectively, and E$_1$ having a concentration of one order of magnitude lower than that of E$_2$ and E$_3$ and located at $E_c - 0.55$ eV. **Figure 1.7** shows DLTS spectra of four different samples: two spectra for bulk samples having different surface orientations and the two other thin film deposited by MBE and HVPE[59].
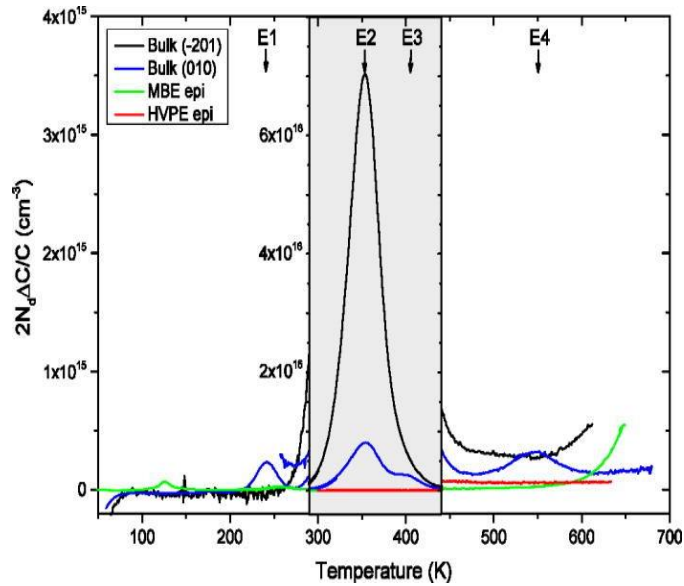
**Figure 1.7 DLTS signal versus temperature for (010) and ($\overline{2}$01) oriented bulk, as well as MBE and HVPE samples**[59].

## 1.5. Optical properties

Optical properties of β-Ga$_2$O$_3$ were intensively studied for both bulk crystals and layers, as their understanding and control (e.g. through intentional doping) expend the area of optoelectronic applications. Galazka et al. [56] studied the optical properties of β-Ga$_2$O$_3$ obtained by the Czochralski method. Transmittance spectra of as-grown crystal obtained for different free electron concentrations are shown in **Figure 1.8.** In each case there is a steep absorption edge at about 260 nm and good transparency in the visible and near infrared region (NIR) especially at low electron concentration. The transmittance increases when the free electron concentration in the single crystal decreased.
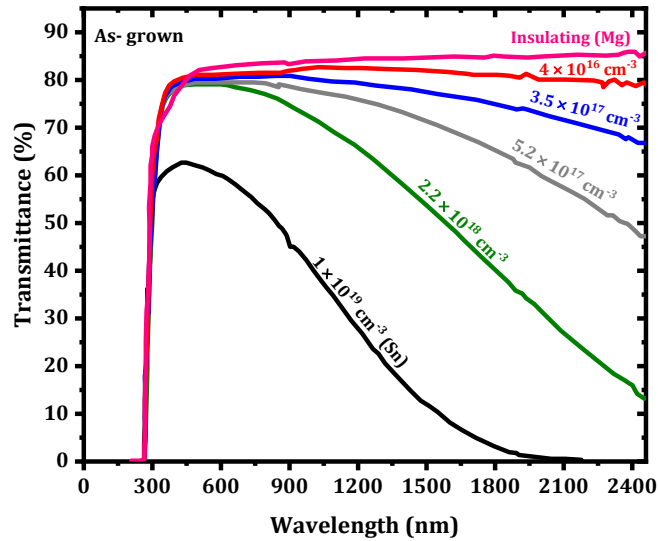
**Figure 1.8 Transmittance spectra of as grown β-Ga₂O₃ single crystals obtained by Czochralski method with various free electron concentrations** [56].

**Figure 1.9** shows a β-$Ga_2O_3$ single crystal ended with spiral (left hand side) and having $1 \times 10^{18} cm^{-3}$ free electrons concentration. The absorption is significant not only in the NIR, but also in the red part of the visible spectrum-giving rise to the blue coloration. Therefore, to grow large β-$Ga_2O_3$ single crystals by Czochralski method the free electron concentration should be kept at the lowest possible level preferentially not exceeding the value $1 \times 10^{18} cm^{-3}$. **Figure 1.9** further depicts a crystal shape improvement from a spiral to a straight cylinder by lowering the free electron concentration in the obtained crystal (middle) or inducing insulating state when doped with Mg (right-hand side).

**Figure 1.9 β-Ga$_2$O$_3$ single crystals obtained by the Czochralski method showing a transition from a spiral to a straight cylinder shape by lowering the free electron concentration from 2×10$^{18}$ cm$^{-3}$ (left) to 4×10$^{16}$ cm$^{-3}$ (middle) and to insulating state by doping with Mg (right)** [56].

# Chapter 2:

# β-Ga₂O₃ Schottky barrier diode development and challenges

## 2.1. Introduction

As mentioned in the previous chapter, Gallium oxide ($\beta\text{-Ga}_2\text{O}_3$) has a serious drawback of developing p-type [6,7], thus hindering its application in bipolar devices (p-n junction, BJT)[2,41]. Currently β-Ga₂O₃ is therefore mainly used in unipolar devices (SBD [3,8], MOSFET [2], TFT [9] and field emission [10]).

SBDs are the main components of switches or rectifiers. The device performance is described by different parameters such as the ideality factor ($n$), the Schottky barrier height ($\phi_B$), the forward current at a specific bias, the on-resistance ($R_{on}$), the leakage current and the breakdown voltage ($V_{br}$). Research on metal–semiconductor (M–S) contacts are very necessary because Schottky contacts with controllable Schottky barrier heights ($\phi_B$) and Ohmic contacts with low series resistance are the basic requirements for achieving acceptable device performances. Recently, the research on β-Ga₂O₃ SBDs have dramatically increased. The main development progress of $\beta\text{-Ga}_2\text{O}_3$ SBD is shown in **Figure 2.1**. With the development of the epitaxy technology, the SBD structure has developed from the initial substrate-based simple structure to the substrate and epitaxial film-based complex structure. The epitaxial drift layer is used in SBDs due to its high purity, which provides a low on-resistance and a high breakdown voltage.

Advanced terminal structures including filed plate and trench have appeared to reduce the surface electric field and the leakage current of the SB. Due to the difficulty in developing p-type $\beta\text{-Ga}_2\text{O}_3$, another p-type semiconductor, for example $Cu_2O$, can be used as a guard ring termination for the SBD [41] as presented in **Figure 2.1**. For SBDs, high work function metals are required for Schottky contact with β-Ga₂O₃ [11] such as Nickel [12], Platinum [13], Copper, Iridium, Tungsten[60] and Gold [1,4,41]. However, there are still some challenges in developing high performance SBDs, including surface treatment of $\beta\text{-Ga}_2\text{O}_3$, controlling SBD output characteristics and understanding transport mechanisms.
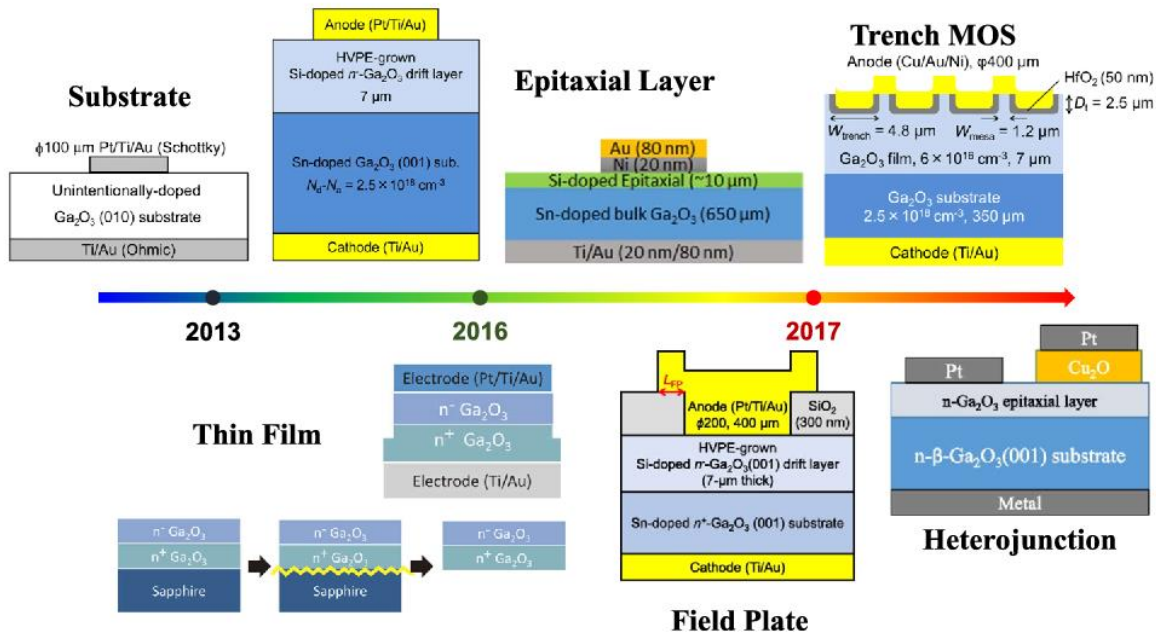
**Figure 2. 1 Development of β-Ga₂O₃ SBD in recent years** [41].

## 2.2. Challenge of surface treatment

Electron-Beam evaporation (EBE) techniques are used for contacts deposition. Before metal deposition, the surface of the substrate or the drift layer must be treated and prepared to remove the surface contaminations and hence reduce surface traps. Conventional techniques based on the chemical etching are commonly used for preparation and cleaning the surface of β-Ga₂O₃. The chemical solutions used include HCl, $H_2SO_4$, $HNO_3$, HF, $H_2O_2$: $H_2SO_4$: $H_2O$=1:4:1, KOH, and NaOH [61]. However, due to high bond strength, it is difficult to wet etch high-quality $β-Ga_2O_3$. Therefore, Argon (Ar) bombardment and plasma provide an enhanced physical component to the etching and are needed to help break bonds, also providing practical and controlled etch rates and good selectivity. But these tend to introduce surface damage, leading to increased leakage, lower breakdown voltages, and ideality factors in forward current considerably higher than unity. Previous studies have shown that the β-Ga₂O₃ surface is sensitive to damage during plasma exposure under high ion density conditions, leading to the introduction of generation-recombination centers that degrade the Schottky characteristics [62,63]. The degradation is related in most works to the increase in Ga vacancies in the surface of HVPE $β-Ga_2O_3$ film. Polyakov et al. [4] studied and analyzed the traps when

17

the surface of $\beta$-$Ga_2O_3$ SBD were subjected to Ar inductively coupled plasma (ICP) treatment for surface preparation before Ni deposition. The exposure of HVPE $\beta$-$Ga_2O_3$ films to ICP Ar plasma increases the density of deep electron traps $E_2^*$ ($E_c - 0.8$ eV) and $E_3$ ($E_c - 1.05$ eV) in the top ~100 nm of the films as presented in **Figure 2.2** and creates in this region a high concentration of deep acceptors with optical threshold near 2.3 eV and 3.1 eV. These deep traps cause the apparent built in voltage in C-V characteristics to strongly decrease from 1 V to −0.02 V and give rise to higher reverse leakage current and to an increase in the ideality factor as shown in **Figure 2.3**.
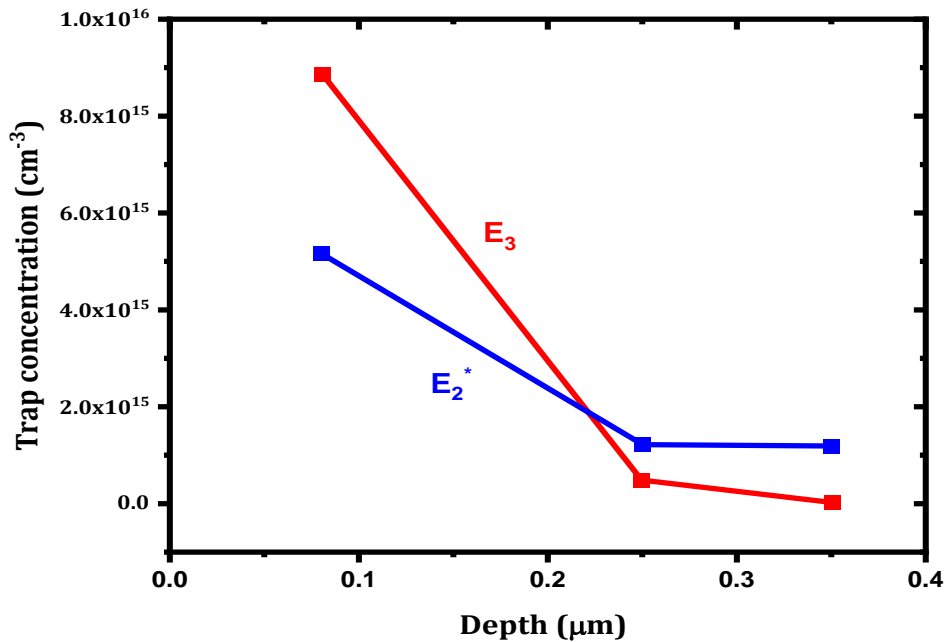


Figure 2. 2 $E_2^*$ and $E_3$ **Traps concentration distribution in the surface of HVPE β-Ga₂O₃** [4].

The introduction of these trap states also leads to a strong decrease in the diffusion length of non-equilibrium charge carriers from 450 nm in reference samples to 150 nm with Ar plasma exposure. Kim et al.[1] used confined magnetic field based sputtering (CMFS) method for Nickel deposition in SBDs and **Figure 2.4 (a)** shows the deposited SBD, which showed less degradation, high performance and high thermal stability than their EBE counterparts, which were related to the diffusion of Nickel atoms in the surface of β-Ga₂O₃. CMFS process generates oxygen (O) and gallium (Ga) vacancies near the β-Ga₂O₃ surface. CMFS can confine a plasma and magnetic field to the faced two targets, in contrast to DC sputtering method, which has unstable plasma discharge due to the change of magnetic field. Slow deposition with low working pressure, leads to the formation of high film density comparison

to DC sputtering and EBE. In addition, it is characterized by a high target utilization comparison with DC sputtering method.
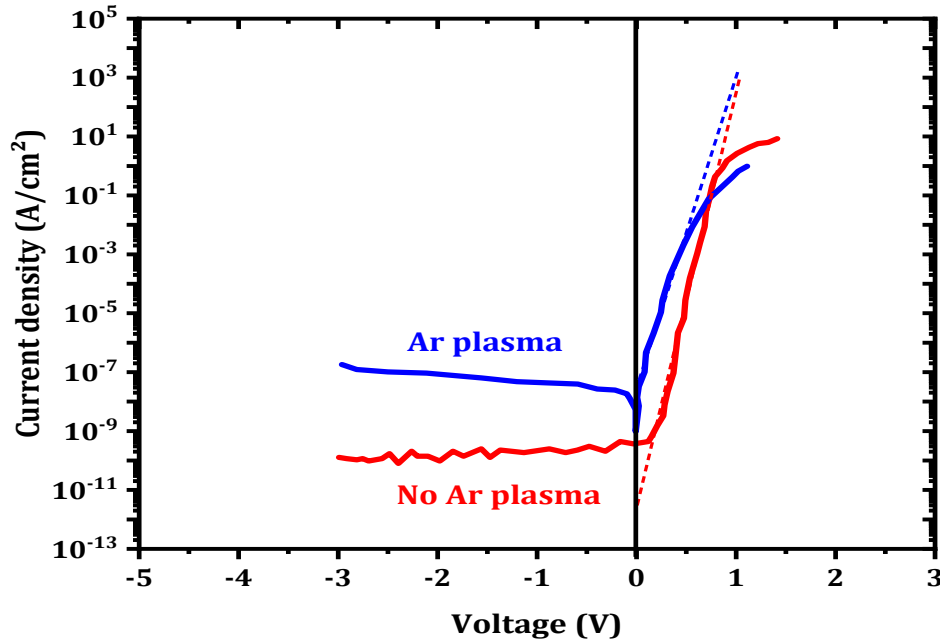


**Figure 2. 3 Effect of Ar plasma on the forward J-V characteristics** [4].

Ni atoms substitute Ga vacancies, when this structure is annealed at temperature higher than 400°C. A shallow interfacial layer was formed by the diffusion of Ni into β-Ga₂O₃ after post-annealing treatment, which significantly influenced the electrical performance of the CMFS-Ni/β-Ga₂O₃ SBDs. In CMFS, the deposition and the surface preparations are simultaneously realized in contrast to EBE where the preparation (using Ar and plasma) and the deposition of metal are separate processes if plasma used for surface preparation before Schottky contact deposited. **Figures 2.4 (b)** and **(c)** show the schematic and processing images of the CMFS-Ni deposition respectively. This techniques based on the cleaning the surface of the drift using the formed plasma. Ar atoms bombard the Ni target and extract Ni atoms, which are transported and deposited in the surface of the β-Ga₂O₃ drift layer. In addition to the high thermal stability, the leakage current of the CMFS-SBDs was only 10% of the leakage current using EBE Ni-based SBDs. Furthermore, CMFS was used to vary the Schottky barrier height and the ideality factor changed from 0.84 to 1.33 eV and 1.20 to 1.04, in EBE and CMFS respectively. Part of the work carried in this thesis is an extensive modeling in order to understand

the role of CMFS technique in improving the SBD performance and reveal the transport mechanisms of the obtained SBD.
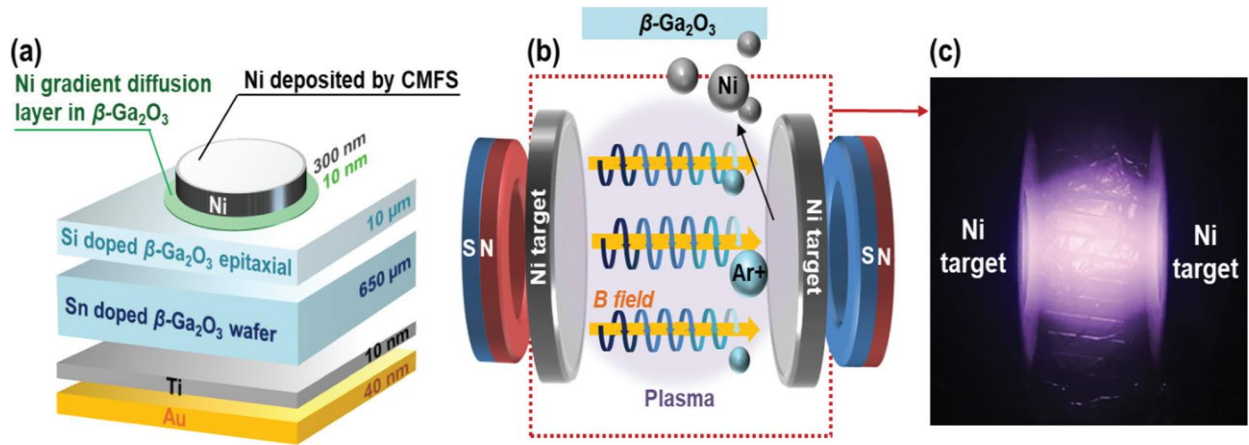


**Figure 2. 4 (a) Ni/β-Ga₂O₃ SBD schematic. Ni Schottky contacts were deposited by CMFS. The gradient Ni-doped β-Ga₂O₃ interfacial layer was formed after post-annealing. (b) Plasma generation with effective ionization mechanism and (c) processing images of CMFS-Ni deposition [1].**

## 2.3. Controlling SBD outputs parameters

As mentioned above, control of the Schottky barrier height ($\phi_B$) and ideality factor are important in controlling its switching properties, in addition to the proposed idea of the annealing SBD deposited by CMFS in different temperature [1]. The other proposed idea for controlling $\phi_B$ is based on the choice of the Schottky metal material as Farzana et al. [11] showed that the metal choice (Pd, Ni, Pt and Au) on (010) β- Ga₂O₃ SBD affected. The obtained $\phi_B$ for each metal are 1.27, 1.54, 1.58 and 1.71 eV respectively and the obtained ideality factors are presented in **Figure 2.5**. Comparison between the metal workfunction variation and the obtained $\phi_B$, a deviation from the Schottky-Mott relation for Au is noticed.
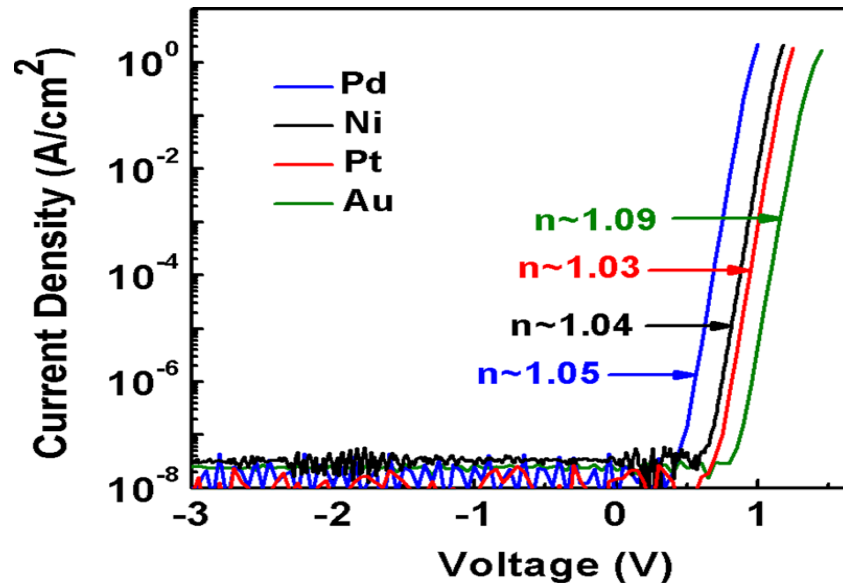
**Figure 2. 5 J-V characteristics of unintentionally doped (010) β-Ga₂O₃ Schottky diodes measured at 300K for four different metals, Pd, Ni, Pt, and Au[11].**

Yao et al. [60]used W, Cu, Ni, Ir and Pt with workfunctions of 4.55, 4.65, 5.15, 5.27 and 5.65 eV respectively and the obtained $\phi_B$ from capacitance-voltage characteristics are 1.94, 1.61, 1.61, 2.3 and 1.9 eV respectively. It is also observed that, $\phi_B$ does not show a universal trend with the metal workfunction indicating that surface/interface states due to defects and crystal orientation, crystal quality and their passivation with different types of surface treatment or metal deposition techniques can play a very important role in its determination. Higher threshold voltage is also obtained. Among the proposed solutions for these problems is a layer deposition between the metal and β-Ga₂O₃ with known properties. Bhattacharyya et al. [64] studied the modulation and enhancement of $\phi_B$ for different β-Ga₂O₃ orientaions and different metals when an ultra-thin SiO₂ is inserted at the metal/β-Ga₂O₃ interface. The SBD surface is improved but it was not the best way to control $\phi_B$. Harada et al. [65] reported systematic variations of $\phi_B$ in metal/PdCoO₂/ β-Ga₂O₃ SBD when Pt, Cr, Ni and Ti are used for Schottky contact as presented in **Figure 2.6 (b)** with an increase in the thickness of the PdCoO₂ inter-layer. This inter-layer consists of ionic Pd⁺ and $[CoO_2]^-$ sublattices alternatingly stacked along the normal of the Schottky interface as presented in **Figure 2.6 (a)**. This polar layered structure of PdCoO₂ spontaneously induces interface dipoles that increase $\phi_B$. The effect of PdCoO₂ on the SBDs' characteristics is presented in **Figure 2.7**.
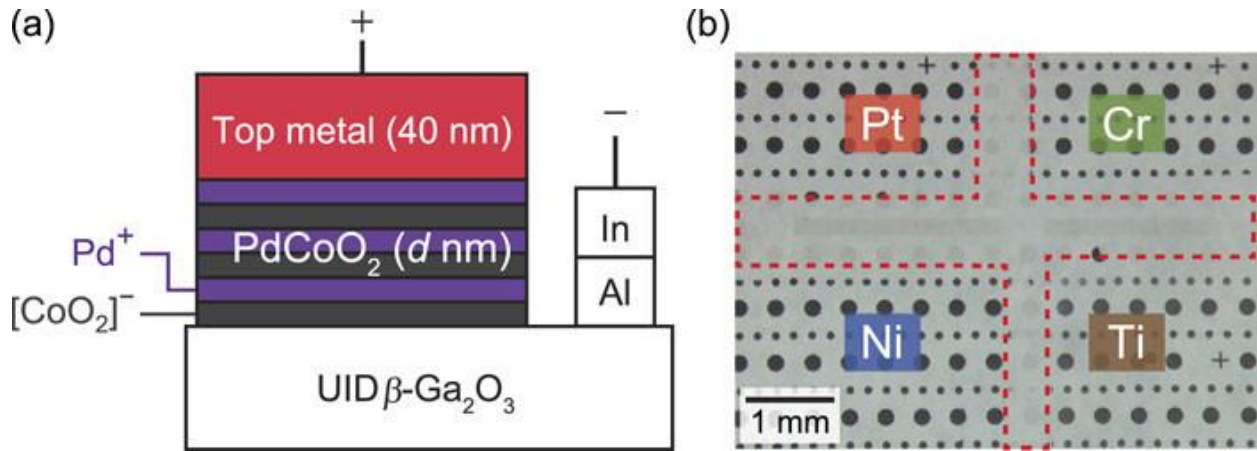
**Figure 2. 6 (a)** Cross-sectional device structure of the metal/PdCoO₂/β-Ga₂O₃ Schottky junction. The layered crystal structure of PdCoO₂ is shown with Pd⁺ and [CoO₂]⁻ sublattices. **(b)** Optical microscopy image of the sample. Four different top metals (Pt, Ni, Cr, and Ti) were deposited. The red dotted line region enclosed does not contain top metals and thus corresponds to the bare PdCoO₂/β-Ga₂O₃ devices [65].
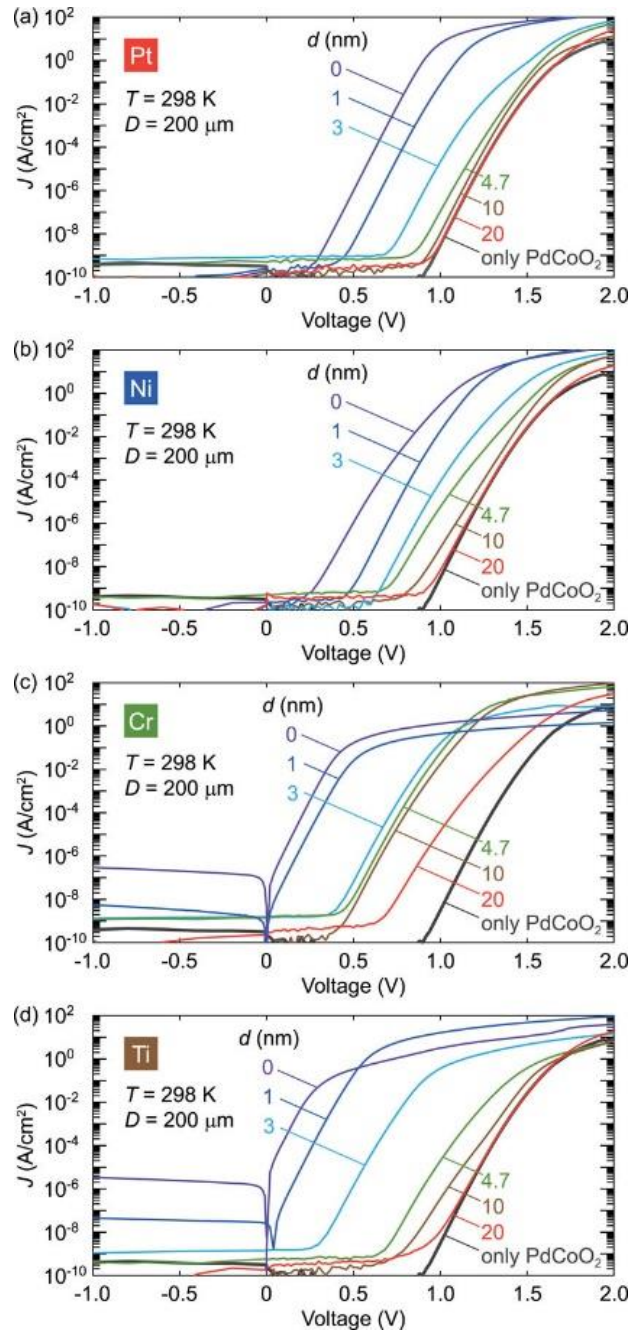
**Figure 2. 7 Room temperature J–V characteristics of (a) Pt, (b) Ni, (c) Cr, and (d) Ti/PdCoO₂ /β-Ga₂O₃ Schottky devices. The diameters (D) of the Schottky diodes are 200 μm. The colored numbers are the d values[65].**

The results demonstrated the possibility of tuning $\phi_B$ in a wide range of variation from 0.7-1.9 eV, as presented in **Figure 2.8**.
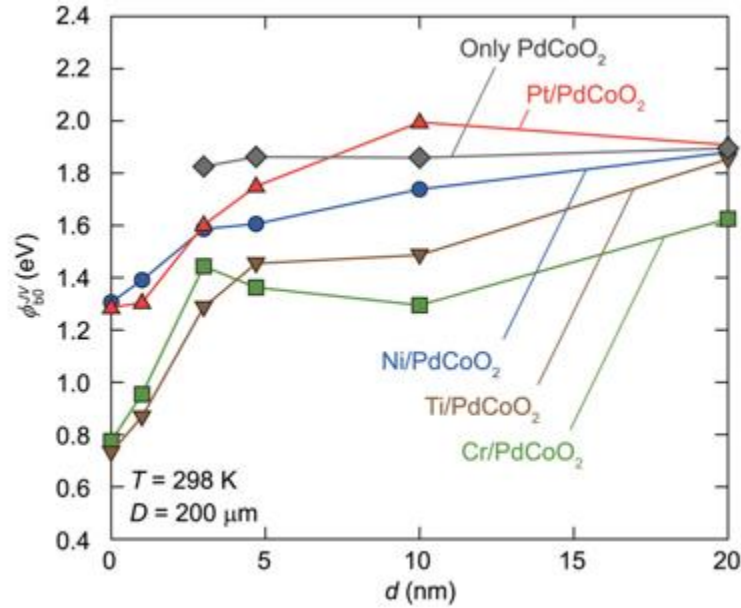
**Figure 2. 8 Schottky barrier height variation versus PdCoO₂ thickness for different metals contacts [65].**

## 2.4. Reverse bias transport mechanisms

In addition to the Schottky barrier height-engineering challenge, there are other challenge related to the exact modeling and understanding of leakage current of β-Ga$_2$O$_3$ SBD under high reverse voltage. Main reported modeling studies of the leakage transport mechanisms in β-Ga$_2$O$_3$ SBD considered thermionic emission (TE) and thermionic field emission (TFE) under high reverse voltage [66,67]. In addition, due to the presence of trap states located near the metal/β-Ga$_2$O$_3$ interface, Zhou et al. [68] used Poole–Frenkel emission (PFE) mechanism to analyse the leakage current for Pt/($\overline{201}$) β-Ga$_2$O$_3$. PFE refers to the emission of electrons from trap state into a continuum of electron states, which could be associated with the presence of defects. **Figure 2.9** (a) shows leakage current of Pt/$\beta$-$Ga_2O_3$SBD at different operation temperatures. A good fitting was obtained in a wide temperature range when PFE was used. Therefore, it can be concluded that emission of electrons from metal into the defect-related trap states should be the dominant leakage current mechanism.

The PFE refers to the emission of electrons via a trap state into a continuum of electron states, which could be associated with the presence of defects. **Figure 2.9 (b)** plot log (J/E) versus $\sqrt{E}$ for the Pt/β-

Ga$_2$O$_3$ SBD measured a various temperatures. The linear dependence of log (J/E) on $\sqrt{E}$ is a good for the PFE mechanism of the leakage current in the devices as expected as [68]:

$$\log\left(\frac{J}{E}\right) = \frac{q}{2.3K_BT}\sqrt{\frac{q.E}{\pi\varepsilon_s}} - \frac{q\phi_B}{2.3K_BT} + \log\ (C) \tag{2.1}$$

Where, $E$, K$_B$, $\phi_B$, $\varepsilon_s$ and C are electric field, Boltzmann constant, the static dielectric constant and constant respectively.
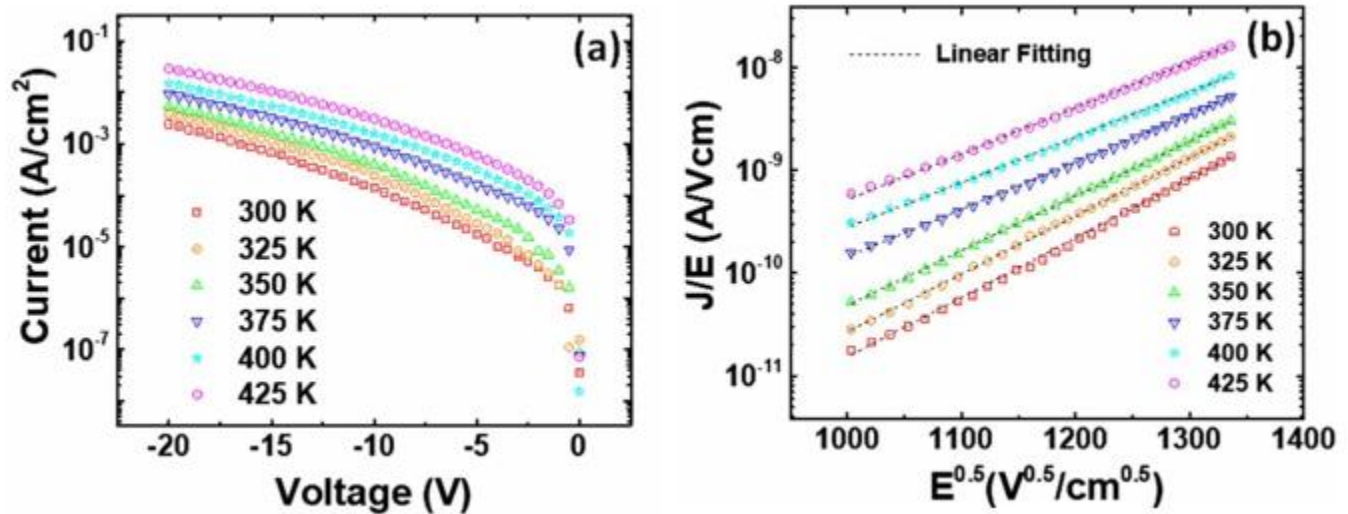


**Figure 2. 9 (a) Leakage current of Pt/β-Ga₂O₃ SBD at different operation temperatures and (b) leakage current is fitted using Poole-Frenkel[68].**

In addition, another important transport mechanism is used for leakage current understanding, which is trap-assisted tunneling (TAT). As shown in **Figure 2.10** temperature-dependent leakage current of two different SBDs (diodes with different β-Ga$_2$O$_3$ orientations) at -6 V with th consideration TAT mechanism with trap activation energy 42 meV. TAT mechanism is based has a dominant effect, where the electrons in the metal first thermally exited to the trap states and then tunnel through $\phi_B$ as shown in the inset of **Figure 2.10**.
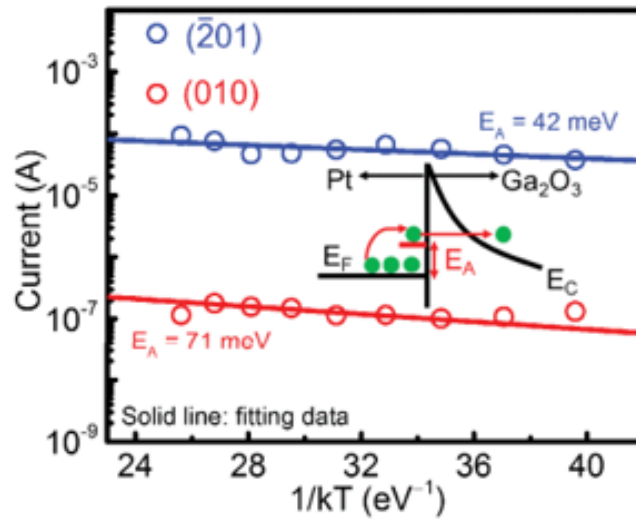
**Figure 2. 10 Arrhenius plot of reverse leakage current of two SBDs at -6 V. The inset is TAT mechanism mode[69].**

Li et al. [66] included tunneling process , thermionic emission (TE) and field emission (FE) models under high reverse voltage in addition to the doping effect and image force lowering (IFL) model. The reverse I–V characteristics was very well-fitted using TE, FE, effective doping density of about $1.45 \times 10^{18}$cm$^{-3}$ and IFL effect as shown in **Figure 2.11**.
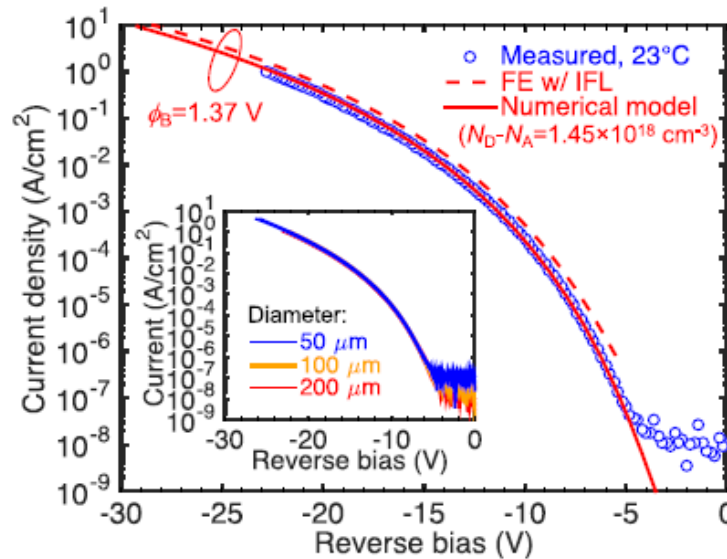


**Figure 2. 11 Measured reverse J–V characteristics at room compared with numerical model with the consideration of TE, FE, IFL and doping effect[66].**

Other work published the domination of TE rather than PFE. Hu et al. [70] studied the reverse current emission mechanism of the Mo/β-Ga$_2$O$_3$ Schottky barrier diode through the temperature dependent current-voltage (I-V) characteristics. The variation of reverse current with the electric field indicates that the TE is the dominant carrier transport mechanism under reverse bias rather than the PFE. Other works combined all the mentioned models [71].

## 2.5. Low temperature transport mechanisms and high ideality factor interpretation

Improving and interpreting β-Ga₂O₃ SBD characteristics at different temperatures are of prime interest and focus. Because the current–voltage ($J$–$V$) characteristics of Schottky diodes measured at room temperatures do not provide satisfactory information about the conduction process and the nature of the barrier, the low-temperature dependent J–V characteristics facilitate understanding the different aspects of the conduction mechanisms. The thermionic emission (TE) current transport mechanism has widely been used to extract Schottky diode parameters. Further, an ideality factor higher than 2 at low temperature is found. The high ideality factor is maybe related to the effect of inhomogeneities at a real MS interface[72,73] and also to the deviation from TE model in forward bias region. Therefore, thermionic field-emission model is proposed[74]. Arslan et al.[75] found a high ideality factor at low temperature for (Ni/Au)/AlInN/AlN/GaN SBD and they related these high values to the effect of tunneling mechanism among the dislocations intersecting the space-charge region. In last few years, there was an increasing interest to study temperatures dependent SBD parameters. For example, Redy et al.[76] examined the temperature-dependent $I$–$V$ characteristics of Au/Ni/β-Ga₂O₃ SBD using thermionic emission mechanism. A 2.76 ideality factor was obtained at 100 K. Also, Sheoran et al.[77] studied Au/Ni/β-Ga₂O₃ SBD. The authors investigated their $I$–$V$ and capacitance-voltage ($C$–$V$) characteristics in a temperature range of 78–350 K. They also obtained an ideality factor of about 3.46 at 100 K with the consideration of thermionic current. In the mentioned works, they related this high value to the effect of barrier inhomogeneities at the Ni/β-Ga₂O₃ interface. However, at low temperature tunneling effect has a very important effect on modeling SBD[78]. Therefore, the tunneling effect must be considered for extract SBD parameters, expect for ideality factor parameter, which is thermionic emission coefficient.

# Chapter 3:

# Ni/β-Ga₂O₃ Schottky barrier diode fabrication and modeling

## 3.1. Introduction

Molecular beam epitaxy (MBE) and metal-organic chemical vapor deposition (MOCVD) have been used to homoepitaxially grow thin films of high structural quality β-$Ga_2O_3$. MBE is an excellent technique for β-$Ga_2O_3$ deposition, but its ultra-high vacuum levels required and the relatively low growth rates (< 1 μm/h) are disadvantages. MOCVD, on the other hand, can be pushed to growth rates as high as 10 μm/h. However, the of metalorganic precursors nature of group-III elements, material grown by MOCVD suffer from high impurities [27,79]. Therefore, among the proposed technique for drift layer of SBD deposition is Halide Vapor Phase Epitaxy (HVPE)[1,4,36,80]. In addition to the drift layer deposition, another important factor for high performance SBD is the quality of the deposited metal. Electron-Beam evaporation (EBE) technique is used in this respect. But due to the high strength of the β-Ga₂O₃ bond, Argon bombardment and plasma provide an enhanced physical etching quality although they tend to introduce surface damage of β-Ga₂O₃ [4,14]. In contrast to the mentioned technique, Confined Magnetic Field based Sputtering (CMFS) shows a good quality and high stability [1], as will be seen in the next chapter. Therefore, the development of high quality SBD is still an ongoing work.

However, due to the high cost, long time and experimental difficulty, technology aided design (TCAD) simulation is opening a new area of research for the development of new devices with low cost and reduced time. Another major motivation for using simulation is the possibility of controlling physical phenomena for better interpretations of the obtained results, as will be seen in the next chapter.

In this chapter, SBD deposition techniques are presented and the physical models used for the simulated SBD are discussed.

## 3.2. Schottky barrier diode deposition details

The Schottky diodes simulated in this work were fabricated on a 650 μm-thick Sn-doped bulk β-Ga$_2$O$_3$ ($N_d$-$N_a \approx 1 \times 10^{18}$ cm$^{-3}$) single crystal wafers with (001) surface orientation. An epitaxial n type β-Ga$_2$O$_3$ drift layer (10 μm-thick, lightly doped Si) was grown on the bulk β-Ga$_2$O$_3$. The doping concentration ($N_d$-$N_a$) of the drift layer was about $3 \times 10^{16}$ cm$^{-3}$ as revealed by capacitance–voltage (C–V) measurement (4284A LCR meter, Agilent). Ti/Au electrode (10/40 nm) was deposited by EBE as an ohmic contact. Ni film (300 nm) was deposited on the drift layer by using CMFS for the Schottky contact. The Schottky metal patterns was formed using a shadow mask, and it had a circular shape with a radius of 150 μm. **Figure 3.1 (a)** and **(b)** show optical top-view images before and after contact deposition respectively. The device formed was annealed at a temperature of about 400 °C in Ar (at a pressure of 100 mTorr) for 1 min using a rapid thermal annealing (RTA) process.
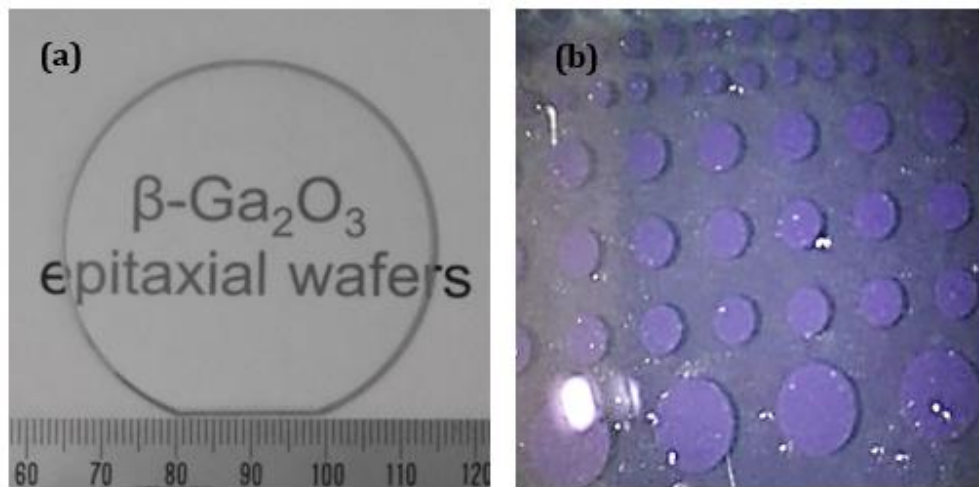


**Figure 3. 1 Optical top-view images (a) before and (b) after contact deposition.**

### 3.2.1. Deposition of Si doped β-Ga₂O₃ drift layer

Usually MBE, PLD, sol-gel, MOCVD, and mist CVD methods can be used for the drift layer deposition. MBE method performs crystal growth in a high vacuum chamber; but it is difficult to grow β-Ga$_2$O$_3$ single crystal thick films. In general, when the growth temperature is increased, a high-quality film can be obtained. However, since the re-evaporation of the source gas increases, a sufficient film formation rate cannot be obtained, which is not suitable for mass production. PLD is

not suitable for large area films growth  due the film formation low rate, so it takes a long time to grow a thick film and therefore not suitable for mass production.  As for the sol-gel, MOCVD and mist CVD methods, it is relatively easy to increase the diameter, but impurities in the raw material are transferred to the $\beta$-Ga$_2$O$_3$single crystal film during the epitaxial growth. Therefore, it is difficult to obtain a high-purity single crystal film. HVPE technique is therefore used, in this work, for drift layer deposition with a high quality and large diameter and controlled doping concentration.

**Figure 3.2** shows a vertical sectional view of an HVPE reactor. The HVPE reactor includes gases introduction ports for N$_2$, O$_2$, Cl$_2$ and dopant gas (SiCl$_4$). In addition to the heating units used for reactions activation for example for decomposition and oxidation and other chemical reactions, a vessel containing a raw Ga used for the formation of GaCl in the presence of  Cl$_2$. The vessel located in the first reaction region (R1) is heated to maintain the raw material predetermined temperature. Next, Cl$_2$ gas is introduced to generate GaCl  by the reaction of Ga with Cl$_2$. Using the transport carrier's gas, GaCl is transported from the first reaction (R1). Because of high temperature, GaCl is decomposed and then oxidized in the presence of O$_2$. Si doped $\beta$-Ga$_2$O$_3$is obtained by heating the source of Si atoms, which is SiCl$_4$ gas on the Sn doped $\beta$-Ga$_2$O$_3$ substrate and the doping concentration is controlled by adjusting the SiCl$_4$ gas.
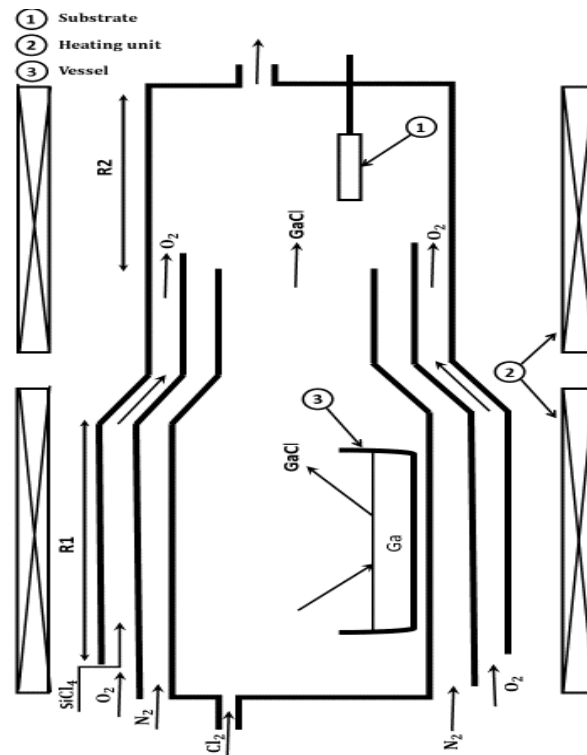


**Figure 3. 2 Vertical sectional view of the vapor phase growth reactor [79].**

### 3.2.2. Deposition of Ni Schottky contact

The Ni Schottky contact is realized by the CMFS deposition method.  The sputtering processes were carried out under the following conditions. Before sputtering, the base pressure was maintained at a high vacuum of $1 \times 10^{-6}$ Torr using a turbo-molecular pump and a rotary pump. A DC power supply was used as the sputtering power source. **Figure 3.3 (a)** and **(b)** show the CMFS reactor and its schematic.
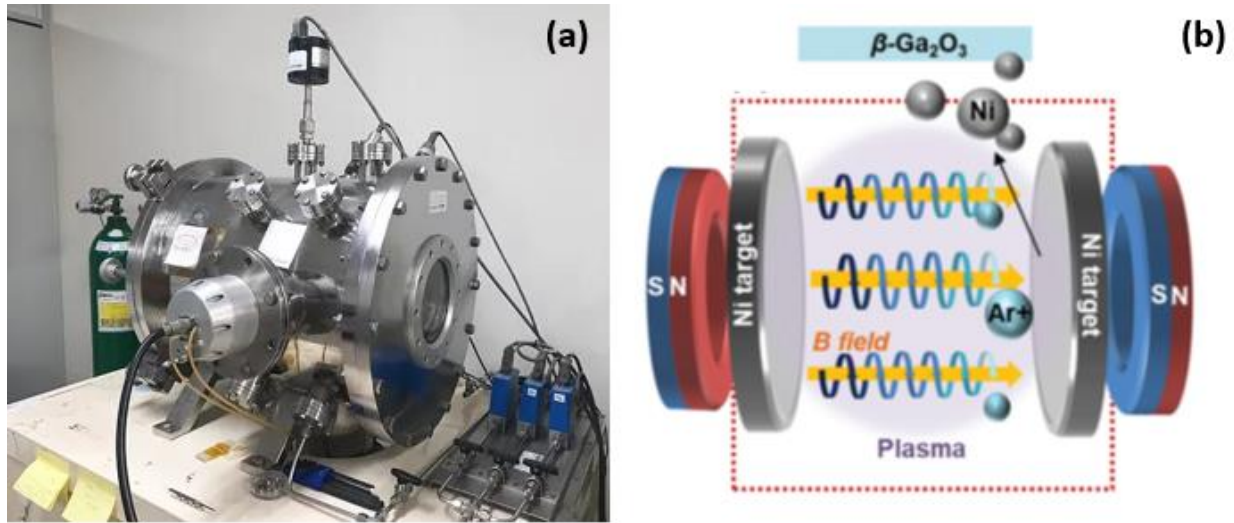


**Figure 3. 3 (a) CMFS reactor and (b) its schematic.**

An open type of permanent magnetic arrangements inserted into two cathodes was used as shown in **Figure 3.3 (b)**. Among common structural characteristics, they have two cathodes with opposite magnetic poles and plasma generated between the two targets. Substrate and epitaxial film-based (Si-doped $\beta$-Ga$_2$O$_3$ deposited on Sn-doped $\beta$-Ga$_2$O$_3$) placed at the center between the two targets as the schematic shows in **Figure 3.3 (b)** Ar working gas was used for plasma generation and Ni target bombardment. Comparing CMFS with DC sputtering, the latter has unstable plasma discharge due to the change of magnetic field and lower sputter yield while the first utilizes high target. For EBE, a low film density with comparison with CMFS and DC sputtering and low uniformity by magnetic field are produced.

## 3.3. The physical models of Ni/β-Ga₂O₃ Schottky barrier diode

The Schottky barrier height ($\phi_B$) is the most important property of a Metal/Semiconductor interface that decides its electrical characteristics. In-depth discussions and explanations of $\phi_B$ usually begin with a consideration of the Schottky-Mott rule. According to Schottky-Mott rule, $\phi_B$ is given by [81]:

$$\phi_{Bn,0} = \phi_{Ni} - \chi_{Ga_2O_3} \tag{3.1}$$

Where $\phi_{Ni}$, and $\chi_{Ga_2O_3}$ are Nickel workfunction and β-Ga₂O₃ electron affinity respectively. Ever since Ni/β-Ga₂O₃ Schottky diodes became available for experimental investigation in the last years, it was clear that the idealistic, non-interacting picture of the Ni/β-Ga₂O₃ interface suggested by the Schottky-Mott rule was not satisfied. Furthermore, there is no clear dependence of the SBH on the metal work function. The absence of a strong dependence of $\phi_{Bn}$ on the metal work function was an unexpected due to the presence of new phenomena. Among the proposed phenomena were the Fermi level pinning and image force lowering [81].

### 3.3.1. Fermi level pinning

The Fermi level pinning in SBD is related to interface states at the Ni/β-Ga₂O₃ interface. These surface interface states producing energy levels within the Ni/β-Ga₂O₃ interface is expected. When Schottky contact is formed, free electrons are transported from the n-type β-Ga₂O₃ to the Ni metal. These free electrons leave ionized donors behind, which produce electric fields, and hence a potential barrier that opposes electron migration. Equilibrium is reached when these two balance each other out. This is an ideal Schottky contact case. Now, consider the case where we have a substantial density of surface states as shown in **Figure 3.4.** Most of the states have a very high probability of being occupied by an electron [81,82]. Therefore, surface states are additional source of electrons by an emission process and providing free carriers to the Ni metal in order to reach equilibrium. Now, the case where we have a very high density of states, and a high density of surface states, electrons produced by these surface states are comparable to electrons transported from the β-Ga₂O₃conduction band. The more extreme case where the number of electrons emitted from the surface states is greater than the number of electrons transported over to the conduction band of β-

Ga$_2$O$_3$. In this case, the number of electrons emitted by the surface states will be enough to reach equilibrium. So, the Fermi level position is fixed to the energy where the surface state density peaks. This is the Fermi level pinning and it takes away a very important degree of freedom of engineering semiconductor devices. This is detrimental since it is a major source of degradation of semiconductor devices. Therefore, cleaning up this surface has been a major topic in the development of semiconductor devices in order to reduce surface states as much as possible. Due to this effect, the extracted SBD parameters differ from the ideal case defined by the Schottky-Mott rule and the ideality factor deviation from unity ($\eta \neq 1$). The ideality factor and the barrier height can be described in terms of interface states by [81,83–85]:

$$n = \left[ 1 + \sum_t \frac{q\delta_t N_{ss}(t)}{\varepsilon_i} \right] \qquad (3.2)$$

$$\phi_B = \phi_B^0 - \sum_t \frac{q\delta_t Q(t)}{\varepsilon_i} \qquad (3.3)$$

Where the index t expresses the sum to the traps type, while $N_{ss}(t)$, $\delta_t$, $Q(t)$ and $\varepsilon_i$ are the densities of states, the thickness, the trapped charge per unit area and the dielectric constant of the interfacial layer, respectively.
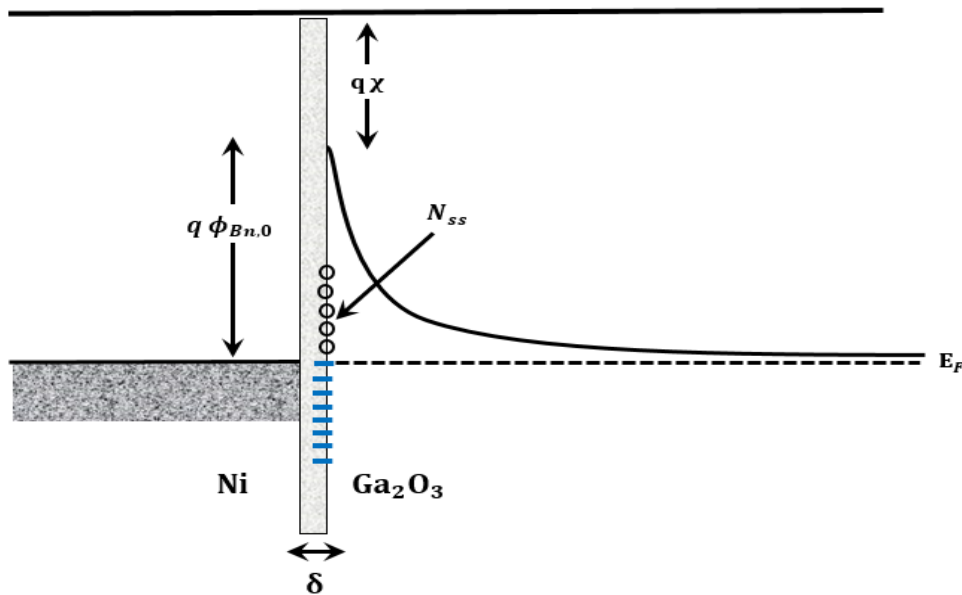


**Figure 3. 4 Energy-band diagram of Ni/β-Ga₂O₃ junction with an interfacial layer and interface states.**

### 3.3.2. Image-force lowering

The presence of free electron carriers in β-Ga$_2$O$_3$ near the Ni contact leads to the creation of an attractive force by the electrostatic effect and thus an electric field exists. This field induces a potential difference and therefore a change in the energy diagram. Because the created force is attractive, the potential difference created is negative, thus corresponds to a lowering of the existing barrier as presented in **Figure 3.5**. This lowering is known as the image-force lowering or the Schottky effect. The reduction of Schottky barrier height from the Schottky-Mott rule is given by [86]:

$$\phi_B = \phi_B^0 - \Delta\phi_B \qquad (3.4)$$

$$\Delta\phi_B = \sqrt{\frac{q|E|}{4\pi\varepsilon_s}} = \frac{q}{\varepsilon_s}\sqrt{\frac{(N_d - N_a)}{4\pi}w} \qquad (3.5)$$

Where $E$, $\varepsilon_s$, $N_d - N_a$ and $w$ are the electric field, the static dielectric constant, the net doping concentration and the depletion region width respectively.
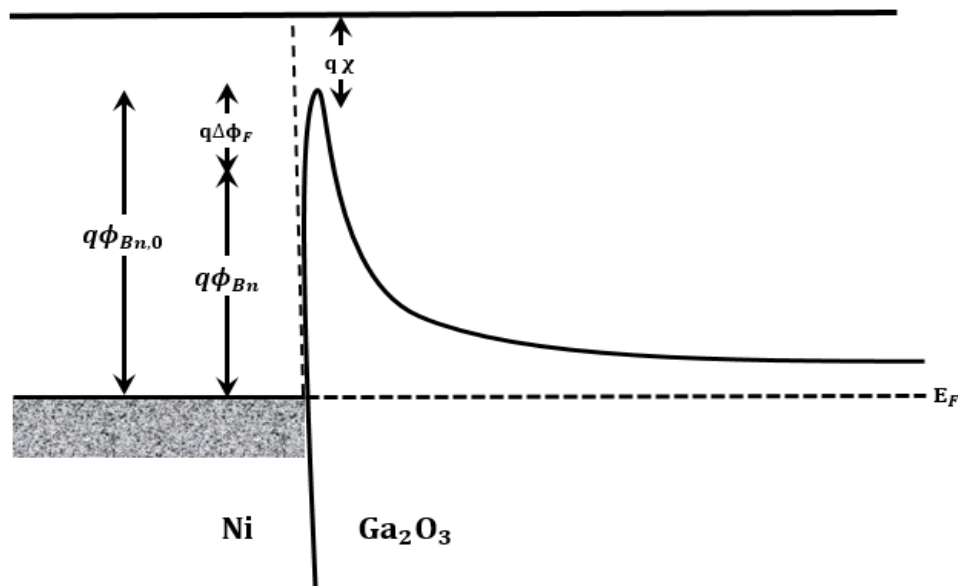


**Figure 3. 5 The energy band diagram incorporating the image force lowering effect in Ni/β-Ga₂O₃ Schottky contact. The barrier height at thermal equilibrium is qϕ$_{B,n}$ The barrier lowering is qΔϕ$_F$.**

### 3.3.3. Carrier recombination models

### 3.3.3.1. Shockley-Read-Hall recombination (SRH)

An allowed energy state within the forbidden bandgap, also called a trap, may act as a recombination center, capturing both electrons and holes. The Shockley–Read–Hall theory of recombination assumes that a single recombination center, or trap, exists at an energy $E_t$ within the bandgap. There are four basic processes, shown in **Figure 3.6** that may occur at this single trap. We will assume that the trap is an acceptor-type trap; that is, it is negatively charged when it contains an electron and is neutral when it does not. The four basic processes are [82,86]:

- **Process 1:** The capture of an electron from the conduction band by an initially neutral empty trap.
- **Process 2:** The inversion of process 1, the emission of an electron that is initially occupying a trap level back into the conduction band.
- **Process 3:** The capture of a hole from the valance band by a trap containing an electron (or we may consider the process to be the emission of an electron from the trap into the valance band).
- **Process 4:** The inversion of process 3, the emission of a hole from a neutral trap into the valance band (or we may consider the process to be the capture of an electron from the valance band into the trap).
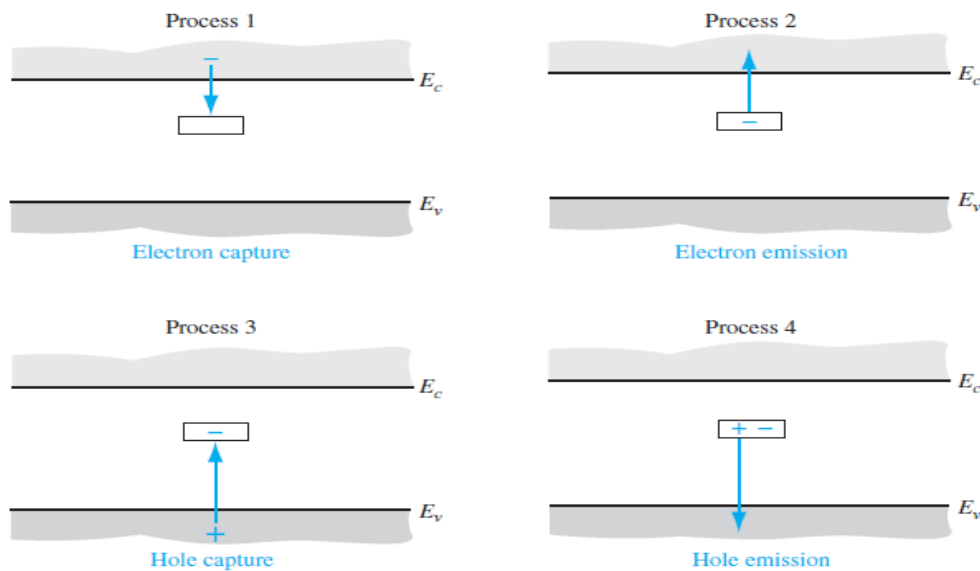


**Figure 3. 6 The basic trapping and emission processes for the case of an acceptor type trap [82].**

In process 1, the rate at which electrons from the conduction band are captured by the trap is proportional to the density of electrons in the conduction band and the density of empty trap states. We can then write the electron capture rate as [82,86]:

$$R_{cn} = C_n N_t [1 - f_F(E_t)] n \qquad (3.6)$$

Where $R_{cn}$, $C_n$, $N_t$, n and $f_F(E_t)$ are capture rate $(cm^{-3} s^{-1})$, capture coefficient which is proportional to electron-capture cross section, total concentration of trapping centers, electron concentration in the conduction band and Fermi function at the trap energy, respectively. The Fermi function at the trap energy is given by [82,86]:

$$f_F(E_t) = \frac{1}{\left[1 + \exp\left(\frac{E_t - E_F}{K_B T}\right)\right]} \qquad (3.7)$$

Which is the probability that a trap will contain an electron. The function $[1 - f_F(E_t)]$ is then the probability that the trap being empty.

For process 2, the rate at which electrons are emitted from a filled trap back into the conduction band is proportional to the number of filled traps. The emission rate is then given by [82,86]:

$$R_{en} = E_n N_t f_F(E_t) \qquad (3.8)$$

Where $E_n$ and $f_F(E_t)$ are the emission constant and the probability that the trap is occupied respectively.

In thermal equilibrium, the rate of electron capture from the conduction band and the rate of electron emission back into the conduction band must be equal. Then [82,86]:

$$R_{cn} = R_{en} \qquad (3.9)$$

Therefore the following equation results [82,86]:

$$C_n N_t [1 - f_{F0}(E_t)] n_0 = E_n N_t f_{F0}(E_t) \qquad (3.10)$$

Where $f_{F0}(E_t)$ denotes the thermal-equilibrium Fermi function and $n_0$ is the equilibrium electron density. Using the Boltzmann approximation for the Fermi function, we can find $E_n$ in terms of $C_n$ as[82,86]:

$$E_n = n' C_n \qquad (3.11)$$

Where n' is given by [82,86]:

$$n' = N_c \exp\left(-\frac{(E_c - E_t)}{K_B T}\right) \qquad (3.12)$$

The parameter n′ is equivalent to an electron concentration that would exist in the conduction band if the trap energy $E_t$ coincided with the Fermi energy $E_F$.

In non-equilibrium, excess electrons exist, so that the net rate at which electrons are captured from the conduction band is given by [82,86]:

$$R_n = R_{cn} - R_{en} \tag{3.13}$$

Which is just the difference between the capture rate and the emission rate. Combining equations (2.6) and (2.8) with (2.13) gives [82,86]:

$$R_n = C_n N_t [1 - f_{F0}(E_t)]n - E_n N_t\, f_{F0}(E_t) \tag{3.14}$$

We may note that, in this equation, the electron concentration $n$ is the total concentration, which includes the excess electron concentration. The Fermi energy in the Fermi probability function needs to be replaced by the quasi-Fermi energy for electrons. The constants $E_n$ and $C_n$ are related by equation (3.11), so the net recombination rate can be written as [82,86]:

$$R_n = C_n N_t \big[ n\big(1 - f_F(E_t)\big) - n'\, f_F(E_t) \big] \tag{3.15}$$

A similar analysis of processes 3 and 4 gives the net rate at which holes are captured from the valance band is given by [82,86]:

$$R_p = C_p N_t [p\, f_F(E_t) - p'\, (1 - f_F(E_t))] \tag{3.16}$$

Where $C_p$ is a constant proportional to the hole capture rate, and p′ is given by [82,86]:

$$p' = N_v \exp\left(-\frac{(E_t - E_v)}{K_B T}\right) \tag{3.17}$$

In a semiconductor in which the trap density is not too large, the excess electron and hole concentrations are equal and the recombination rates of electrons and holes are equal. If we set equation (2.16) equal to equation (3.17) and solve for the Fermi function, we obtain [82,86]:

$$f_F(E_t) = \frac{C_n n + C_p p'}{C_n(n+n') + C_p(p+p')} \tag{3.18}$$

We may note that $n'p' = n_i^2$. Then, substituting equation (3.18) back into either equation (3.15) or (3.16) gives [82,86]:

$$R_n = R_p = \frac{[C_n C_p(n.p - n_i^2)]}{[C_n(n+n') + C_p(p+p')]} \tag{3.19}$$

Equation (3.19) is the recombination rate of electrons and holes due to the recombination center at $E = E_t$.

### 3.3.3.2. Auger recombination

The Auger recombination is a bimolecular recombination where, the released energy during the recombination of an electron and a hole is not an emission of a photon but, instead, it is transferred to a third particle (electron or a hole). The energy is eventually transferred non-radiatively from the hot third carrier via phonon emission to the lattice. Auger Recombination is commonly modelled using the expression[82,86]:

$$R_{Auger} = \gamma_n(p.n^2 - n.n_i^2) + \gamma_p(n.p - p.n_i^2) \tag{3.20}$$

Where $\gamma_n$ and $\gamma_p$ are the Auger coefficients ($cm^6/s$).

### 3.3.4. Mobility models

### 3.3.4.1. Concentration and temperature dependent mobility

Electrons and holes are accelerated by electric fields, but lose momentum as a result of various scattering processes. These scattering mechanisms include lattice vibrations (phonons), impurity ions, other carriers, surfaces, and other material imperfections. Since the effects of all of these microscopic phenomena are lumped into the macroscopic mobilities introduced by the transport equations, these mobilities are therefore functions of the local electric field, lattice temperature, doping concentration, and so on. The concentration dependent mobility parameter is the model that links the mobility to the concentration of dopants. This model includes the effects of lattice scattering, impurity scattering (with screening from charged carriers), carrier-carrier scattering, and impurity clustering effects at high concentration as follow:

$$\frac{1}{\mu_{n,p}} = \frac{1}{\mu_{n,pL}} + \frac{1}{\mu_{n,p\ DAP}} \tag{3.21}$$

$\mu_{n,p}$ are the total electron and hole mobilities, $\mu_{n,pL}$ are the electron and hole mobilities due to lattice scattering, $\mu_{n,p\ DAP}$ are the electron and hole mobilities due to donor (D), acceptor (A), screening (P) and carrier-carrier scattering.

### 3.3.4.2. Parallel electric field dependent mobility

As carriers are accelerated in an electric field, their velocity will begin to saturate when the electric field magnitude becomes significant. This effect has to be accounted for by a reduction of the effective mobility since the magnitude of the drift velocity is the product of the mobility and the electric field component in the direction of the current flow. This model expresses the parallel electric field mobility dependence as [87]:

$$\mu_n(E) = \mu_{n0} \left[ \frac{1}{1+\left(\frac{\mu_{n0}E}{v_{satn}}\right)^{\gamma_n}} \right]^{\frac{1}{\gamma_n}} \tag{3.22}$$

$$\mu_p(E) = \mu_{p0} \left[ \frac{1}{1+\left(\frac{\mu_{p0}E}{v_{satp}}\right)^{\gamma_p}} \right]^{\frac{1}{\gamma_p}} \tag{3.23}$$

Where $v_{satn}$ and $v_{satp}$ are the electron and hole saturation velocities $\gamma_n$ and $\gamma_p$ are constants, $\mu_{n0}$ and $\mu_{p0}$ are the total electron and hole mobilities.

### 3.3.5. Bandgap models

### 3.3.5.1. Bandgap narrowing

In the presence of heavy doping, greater than $1 \times 10^{18} cm^{-3}$, experimental work has shown that the bandgap of β-Ga₂O₃ becomes doping dependent [88]. As the doping level increases, a decrease in the bandgap separation occurs, where the conduction band is lowered by approximately the same amount as the valence band is raised. In this model the intrinsic concentration variation versus the bandgap narrowing is given by [89]:

$$n_{ie}{}^2 = n_i{}^2 \exp\left(\frac{\Delta E_g}{K_B T}\right) \tag{3.24}$$

Where $n_{ie}$ and $n_i$ are the intrinsic concentration after and before lowering and $\Delta E_g$ is the bandgap lowering respectively.

The variation of $\Delta E_g$ with doping is given by [89]:

$$\Delta E_g = a.\left\{ \ln\left(\frac{N}{b}\right) + \sqrt{\left(\ln\left(\frac{N}{b}\right)\right)^2 + c} \right\} \tag{3.25}$$

Where $a, b, c$ are bandgap narrowing parameters and $N$ is the doping concentration.

### 3.3.5.2. Bandgap variation with temperature

Band gap changes with higher temperature mainly arise from the change of the lattice constant. Experimental results show that the band gaps of most semiconductors decrease with increasing temperature. The variation of the band gap with temperature is given by[86]:

$$E_g(T) = E_g(0) - \frac{\alpha.T^2}{T+\beta} = E_g(300) + \alpha \left[ \frac{300^2}{300+\beta} - \frac{T^2}{T+\beta} \right] \qquad (3.26)$$

Where $E_g(300)$ is the room temperature bandgap and $\alpha$ and $\beta$ are parameters related to β-Ga₂O₃.

### 3.3.6. Impact ionization model

The Selberherr's impact ionization model is used to describe the avalanche breakdown effect. The avalanche breakdown process occurs when electrons and/or holes, moving across the space charge region, acquire sufficient energy from the electric field to create electron–hole pairs by colliding with atomic electrons within the depletion region. The avalanche process is schematically shown in **Figure 3.7**. The newly created electrons and holes move in opposite directions due to the electric field and thereby create a reverse-biased current. In addition, the newly generated electrons and/or holes may acquire sufficient energy to ionize other atoms, leading to the avalanche process. For most PN junctions, the predominant breakdown mechanism is the avalanche effect [82].
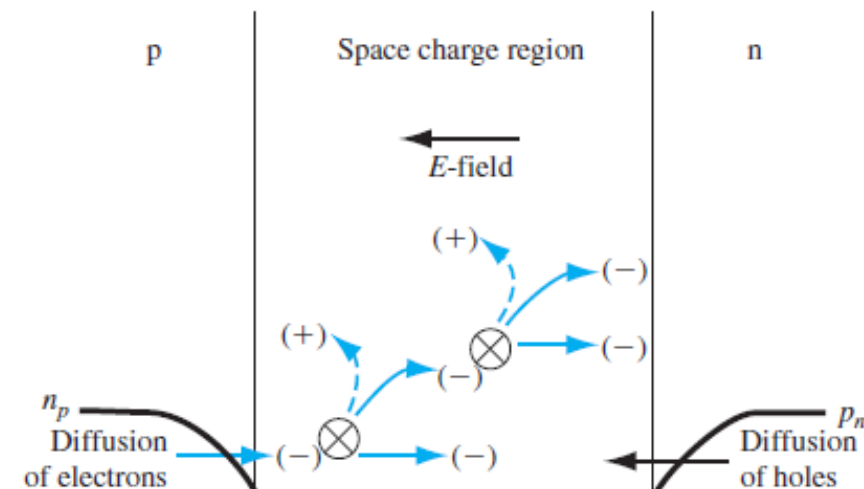


**Figure 3. 7 Avalanche breakdown process in a reverse-biased PN junction**[82].

Selberherr's Impact ionization (SELB) model used for avalanche breakdown is defined through the following coefficients for electrons and holes [90]:

$$\alpha_n = A_n \exp\left(-\left(\frac{B_n}{E}\right)^{\beta_n}\right) \tag{3.27}$$

$$\alpha_p = A_p \exp\left(-\left(\frac{B_p}{E}\right)^{\beta_p}\right) \tag{3.28}$$

Where $E$ is the electric field in the current direction and $A_n$, $A_p$, $B_n$, $B_p$, $\beta_n$ and $\beta_p$ are fitting parameters.

### 3.3.7. Incomplete ionization

Generally, the simulation is carried out at room temperature, where, in most cases, the semiconductor is considered in the full impurities ionization state. However, as temperature is decreased, full ionization of impurities can no longer be assumed. In this case, the dependence of ionized impurities on temperature is modelled using Fermi-Dirac statistics. The ionized donor and acceptor impurity concentrations are given by[82,86]:

$$N_d^+ = \frac{N_d}{\left[1 + g_d.\exp\left(\frac{(E_{Fn} - (E_c - E_{B,d}))}{K_B T}\right)\right]} \tag{3.29}$$

$$N_a^+ = \frac{N_a}{\left[1 + g_a.\exp\left(\frac{(E_v - (E_{Fp} + E_{B,a}))}{K_B T}\right)\right]} \tag{3.30}$$

Where $E_{B,d}$ and $E_{B,a}$ are the dopant activation energies, $g_d$ and $g_a$ are the conduction and valance band degeneracy factor, $N_d$ and $N_a$ are the net compensated n-type and p-type doping, respectively.

### 3.3.8. Transport models

In a Schottky junction, the current is mainly due to majority carriers. Unlike the p-n junction where the minority carriers are the responsible for the current. The current transport can be described by three theories depending on the semiconductor properties (thermionic emission theory, diffusion theory and tunneling). The thermionic emission locates the current limitation at the interface between Ni and Si-doped $\beta$-Ga$_2$O$_3$ especially when the free carriers have enough energy to surmount the barrier height. On the other hand, the diffusion theory locates the current limitation in

the depletion region. However, when the carrier's energy is lower than the barrier height, there is a probability to penetrate this barrier through tunneling.

### 3.3.8.1. Thermionic emission

As mentioned above, thermionic emission is a majority carrier current which is always associated with Schottky barrier height. The critical parameter is the barrier height and not the shape of the barrier [86]. The thermionic emission characteristics are derived by assuming that the barrier height is much larger than $K_B T$, so that the Maxwell–Boltzmann approximation applies and that thermal equilibrium is not affected by this process [82,86]. The thermionic current is the sum of the current density due to electrons flow from β-Ga₂O₃ to Ni and the current density due to electrons flow from Ni to β-Ga₂O₃. After some approximations the thermionic current is given by [78]:

$$J_{Th} = J_s \left( \exp \left( \frac{q(V - R_s J)}{\eta K_B T} \right) - 1 \right) \tag{3.31}$$

Where $J_s$ is the saturation current density, $q$ is the elementary charge, $R_s$ is the series resistance and $\eta$ is the ideality factor. $K_B$ and $T$ are Boltzman constant and the absolute temperature (K), respectively. In this conduction mechanism, $J_s$ is given by [78]:

$$J_s = A^* T^2 \exp\left(-\frac{q\phi_B}{K_B T}\right) \tag{3.32}$$

Where $A^*$ is the Richardson constant (41.11 A.$cm^{-2} K^{-2}$ for β-Ga₂O₃ [1]) and $\phi_B$ is the Schottky barrier height.

### 3.3.8.2. Diffusion

The diffusion theory also assumes that the barrier height is much larger than $K_B T$, and the carrier concentrations at the interface Ni/β-Ga₂O₃ and at the border of the depletion region, are unaffected by the current flow (i.e. they have their equilibrium values), and finally, β-Ga₂O₃ must be non-degenerate. The current density is given by [82,86]:

$$J_n = q\mu_n n(x, y, z) E(x, y, z) + qD_n \nabla n \tag{3.33}$$

Where q, $\mu_n$, n, $E$ and $D_n$ are elementary charge, electron mobility, internal electric field and diffusion coefficient respectively.

### 3.3.8.3. Tunneling

Tunneling is a quantum-mechanical phenomenon. In classical mechanics, carriers are completely confined by the potential walls. Only those carriers with excess energy higher than the barriers can escape, as in the case of thermionic emission discussed above. In quantum mechanics, an electron can be represented by its wavefunction. The wavefunction does not terminate abruptly on a wall of finite potential height and it can penetrate into and through the barrier. The probability of electron tunneling through a barrier of finite height and width is thus not zero.

The tunnelling model was considered using Universal Schottky Tunneling (UST) model and the tunneling current is given by [86]:

$$J_T = \frac{A^* T_L}{K_B} \int_\epsilon^\infty \Gamma(E') \ln\left(\frac{1+F_s(E')}{1+F_m(E')}\right) dE' \tag{3.34}$$

The tunnelling generation rate ($G_T$) is the given by[91]:

$$G_T = \frac{1}{q} \nabla J_{TE} \tag{3.35}$$

Where $A^*, T_L, K_B, \epsilon, F_s(E')$ and $F_m(E')$ are effective Richardson's coefficient, lattice temperature, Boltzmann constant, electrons energy, and the Maxwell-Boltzmann distribution in β-Ga₂O₃ and Ni, respectively and $\Gamma(E')$ is the tunnelling probability, which is given by [86]:

$$\Gamma(\epsilon) = \exp\left[-2\frac{\sqrt{2m^*}}{\hbar} \int_{x_1}^{x_2} \sqrt{E_c(x) - \epsilon} \, dx\right] \tag{3.36}$$

Here, $E_c(x)$ and $(x_1, x_2)$ are the potential energy distribution of Schottky barrier diode and classical turning points, respectively.

### 3.3.8.4. Band to band tunneling (BBT)

If a sufficiently high electric field exists within a device, local band bending may be sufficient to allow electrons to tunnel, by internal field emission, from the valence band into the conduction band as presented in **Figure 3.8**. An additional electron is therefore generated in the conduction band

and a hole in the valence band. This generation mechanism is implemented into the right-hand side of the continuity equations. The tunneling generation rate is [92–94]:

$$G_{BBT} = B_1 . E^{B_2} e^{-(\frac{B_3}{E})}$$

(3.37)

Where $B_1$, $B_2$ and $B_3$ are Band-to-Band model parameters and $E$ is the local electric field.
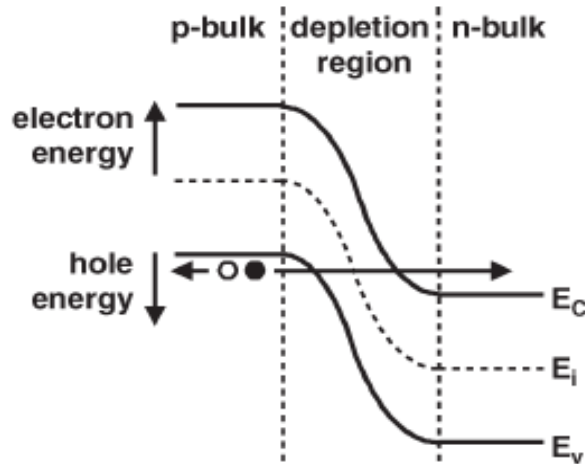


**Figure 3. 8 Schematic representation of the band-to-band tunneling process[94].**

### 3.3.9. Self-Heating

The thermal behaviour of power semiconductor devices is a main cause affecting their reliability and performance. Wachutka [95] proposed a model based on the laws of phenomenological irreversible thermodynamics and it is consistent with the physical models usually considered in the isothermal drift diffusion approximation. The "classical" isothermal device equations are extended and completed by a generalized heat conduction equation involving heat sources and sinks which, besides Joule and Thomson heat, reflect the energy exchanged through (radiative and non-radiative) recombination and optical generation. Thus the extended model also applies to direct semiconductors (e.g., optoelectronic devices) and accounts for effects caused by the ambient light intensity. Furthermore, it fully allows for low temperature since the case of incomplete ionization of donors and acceptors (impurity freeze-out) is properly incorporated in the theory. By adopting this model, the lattice heat flow equation will be added to the dynamic continuity equations for electrons and holes flow [95]:

$$c \left( \frac{\partial T}{\partial t} \right) = div \left( k . \vec{\nabla} T \right) + H$$

(3.38)

Where "$c$" is the heat capacitance per unit volume, "$k$" is the thermal conductivity, and "$H$" is the heat generation rate, which is given by[95]:

$$H = H_J + H_{PT} + H_{GR} \tag{3.39}$$

Where $H_J$, $H_{PT}$ and $H_{GR}$ are the joule generation, Peltier recombination heating and Thompson cooling respectively.

# Chapter 4

# Silvaco TCAD simulation

## 4.1. Introduction

For over three decades, Silvaco has solved semiconductor design challenges by offering affordable and competitive EDA (Electronics Design Automation) software, proven design IP (intellectual property), and world class support to engineers and researchers across the globe. Silvaco solutions span from atoms to systems: starting with simulation of material behavior impacting semiconductor devices, to design and analysis of transistor circuits, and lastly providing IP blocks for systems-on-chip (SoC) designs. Silvaco TCAD is a powerful devices design simulator that provides better physics insight with realistic parameters observations, including electrical, optical and thermal properties. It is a physically based two and three-dimensional device simulator and provides insight into the internal physical mechanisms associated with device operation.

## 4.2. Silvaco overview

Silvaco Atlas contains a large number of useful modules among the most used as interactive tools DeckBuild and Tonyplot, process simulator Athena, device simulator Atlas, structure and mesh editor DevEdit as presented in **Figure 4.1**.
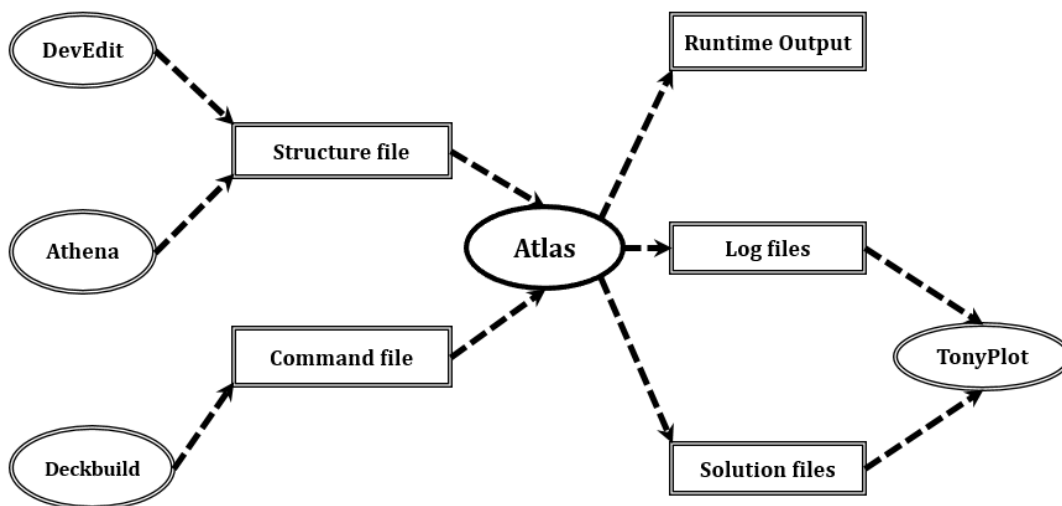


**Figure 4. 1 Simulation flow diagram of Silvaco TCAD.**

- **Deckbuild:** is an interactive, graphic runtime environment for developing process and device simulation input decks. It is the main window of SILVACO where all simulators can be controlled.

- **Atlas:** is a physically based device simulator module, which predicts the electrical characteristics that are associated with specified physical structures and bias conditions. This is achieved by approximating the operation of a device onto a grid (discretizing). The transport of carriers through this device can be simulated by applying a set of differential equations, derived from Maxwell's laws in this grid. This means that Atlas provides a platform to analyse AC, DC and time domain responses for all semiconductor based technologies in two and three dimensions. Atlas is also used for device generation.

- **TonyPlot:** is a graphical post-processing tool for use with all Silvaco simulators and is an integral part of the Interactive Tools. TonyPlot can operate stand-alone or along with other interactive tools, such as DECKBUILD. It provides scientific visualization capabilities including xy plots with linear and logarithmic axes, polar plots, surface and contour plots.

### 4.2.1. Deckbuild

It is the graphic interface between the user and simulators. It consists of two windows. One for input deck creation and editing, in this window the simulators can be called and controlled using Deckbuild commands. The second window is for simulators outputs and results and simulation details (**Figure 4.2**).
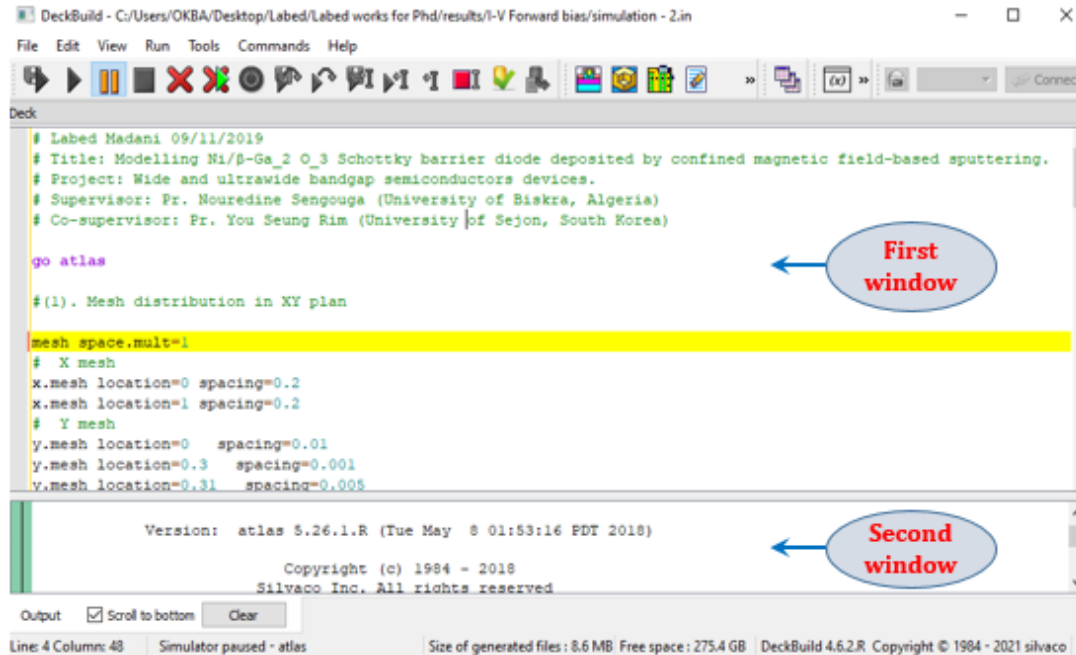
**Figure 4. 2 Deckbuild two windows.**

### 4.2.2. Device generation and simulation using Atlas

As presented in **Figure 4.1**, Atlas is the core part of Silvaco TCAD simulation, Atlas run inside DeckBuild and start with the line "go Atlas" and comments in Deckbuild are preceded by "#". The order in which statements occur in an Atlas input file is important. There are five groups of statements that must occur in the correct order (**Figure 4.3**). Otherwise, an error message will appear which may cause incorrect operation or termination of the program. The order of statements within the mesh definition, structural definition, and solution groups is also important. Otherwise, it may also cause incorrect operation or termination of the program.

| Group | | Statements |
|-------|---|------------|
| 1. Structure Specification | ▬▬▬▬ | Mesh<br>Region<br>Electrode<br>Doping |
| 2. Material Models Specification | ▬▬▬▬ | Material<br>Models<br>Contact<br>Interface |
| 3. Numerical Method Selection | ▬▬▬▬ | Method |
| 4. Solution Specification | ▬▬▬▬ | Log<br>Solve<br>Load<br>Save |
| 5. Results Analysis | ▬▬▬▬ | Extract<br>TonyPlot |

**Figure 4. 3 Flow chart and command groups of Atlas.**

### 4.2.2.1. Structure specification

The first step in device specification is to determine the mesh profile in the device. A mesh refers to a collection of elements whose union defines the device (**Figure 4.4**). It is established by overlapping two sets of parallel lines perpendicular to each other to form a network, which has the device shape. The intersections of lines are called nodes, while the spaces between them called elements. Accurate simulation requires a smooth mesh that can resolve all significant requirements of the solution. Numerical efficiency requires a rough mesh that minimizes the total number of grid points thus a fast simulation. Another condition must be taken in consideration is the maximum number of nodes supported by the software; in Silvaco TCAD (Atlas), a two-dimensional simulations may support up to 100,000 nodes. Three-dimensional simulations may support up to 20,000,000 nodes and 40,000,000 elements, with no more than 100,000 nodes in a single plane and a maximum of 2,000 planes in the z direction[96].
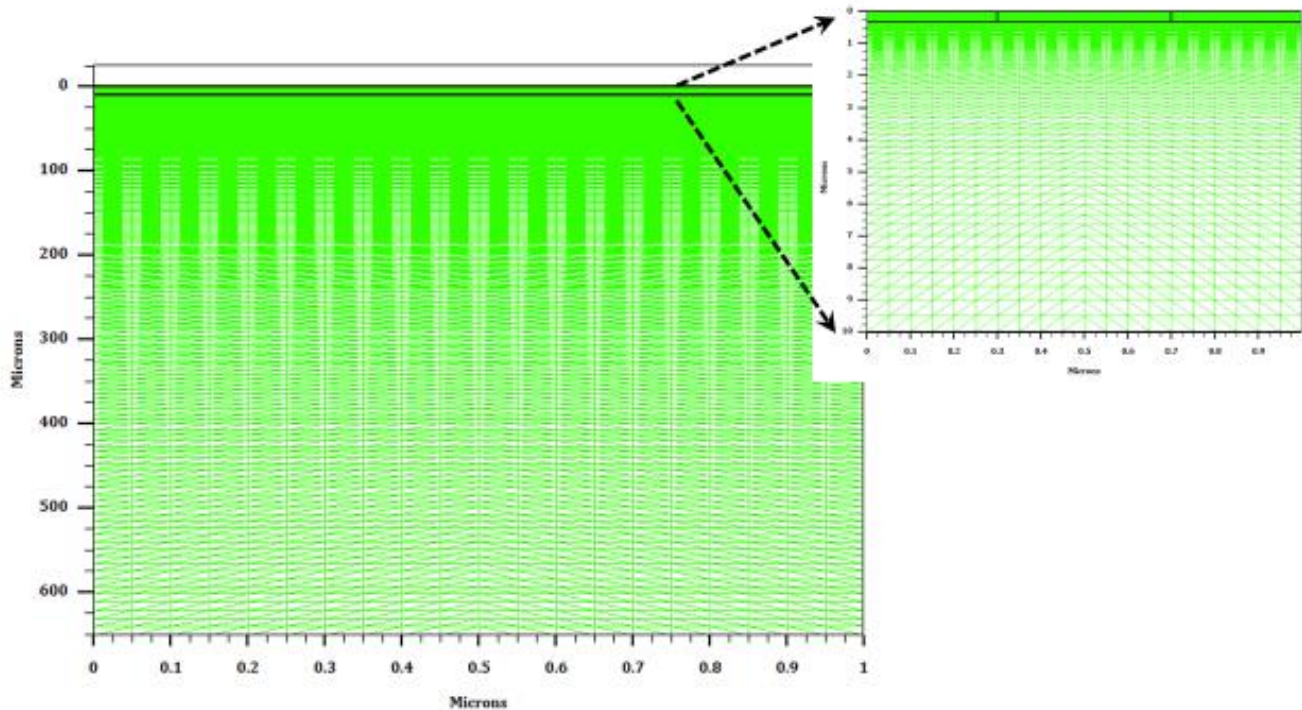
**Figure 4. 4 Mesh Profile in a simulated device.**

**Figure 4.4** shows the device's mesh of the considered example, which can be generated using the following code:

```
# X mesh
x.mesh location=0      spacing=0.5
x.mesh location=20     spacing=0.5
# Y mesh
y.mesh location=0      spacing=0.01
y.mesh location=0.3    spacing=0.001
y.mesh location=0.31   spacing=0.005
y.mesh location=10     spacing=0.5
y.mesh location=660    spacing=10
```

Where "spacing" specifies the mesh spacing at the mesh locations specified by "location" parameter. The next step is the layers specification, the structure presented in **Figure 4.5**, which can be realised by using the following code:

region number=1 user.material=air x.min=0 x.max=20 y.min=0\     y.max=0.3

region number=2 user.material=GaxOyNiz x.min=0 x.max=20 y.min=0.3\   y.max=0.31

region number=3 user.material=Ga2O3Si x.min=0 x.max=20 y.min=0.31\ y.max=10

region number=4 user.material=Ga2O3Sn x.min=0 x.max=20 y.min=10\   y.max=660
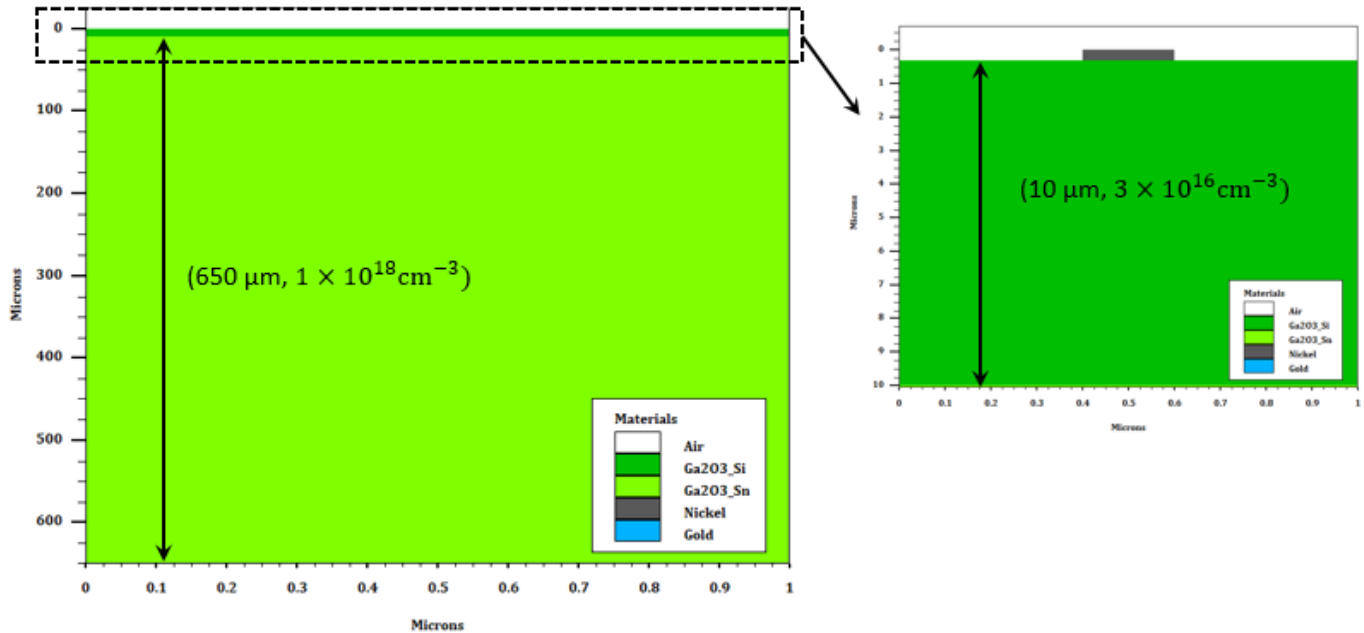


**Figure 4. 5 Device layers specification.**

The Schottky barrier is known as the barrier height at the junction for the injection of electrons from the metal to the semiconductor conduction band, and it is equal to the difference between the metal work function and the electron affinity of semiconductor. Therefore, the metal work function defines if the contact is rectifying or Ohmic.

The command "contact" is used to tell Atlas how to treat the electrode. In the default condition, an electrode in contact is assumed Ohmic. If the electrode is wanted to be treated like a Schottky contact, then the appropriate work function must be defined according to the following Silvaco Atlas code:

Electrode name=anode material=nickel x.min=5 x.max=15 y.min=0\ y.max=0.3 workf=5.35

electrode name=cathode material=gold bottom

The simplest method for doping profile specification; presented in the following code:

doping conc=3e16 n.type uniform x.min=0 x.max=20 y.min=0.3\ y.max=10

doping conc=1e18 n.type uniform x.min=0 x.max=20 y.min=10\ y.max=660

Which means an n type uniform doping profile of the specified layer locations.

Finally, the presence of deep defects may significantly influence the electrical characteristics of the device. Two methods are used to introduce deep levels in Atlas, depending on their spatial distribution: the "trap" statement activates bulk traps at discrete energy levels within the bandgap of the semiconductor with a uniform distribution and sets their parameter values. While the "doping" statement can be used to introduce a non-uniform traps distribution.

Deep levels can be defined using their activation energy, emission and capture cross section for electrons and holes and their density. These are the required parameters to define traps in Atlas, in addition to their type and location. The following line of code is an example of the Atlas syntax for traps definition:

trap acceptor x.min=0 x.max=20 y.min=0.3 y.max=0.31 e.level=0.8 \ density=5.2e15 degen=1 sign=0.5e-12 sigp=0.5e-14

In this line of code, the first word (trap) is the statement and the rest are parameters that describe the trap. Where: "acceptor" specifies the traps type, "x.min, x.max, y.min, y.max" specify the edges of the region where the traps are located. "e.level" specifies the energy level position of traps relative to the conduction band in the case of acceptor traps or valence band in the case of donor traps. The unit here is the electron Volt (eV). "density" specifies the density of the traps centers in ($cm^{-3}$), "degen" specifies the degeneracy factor and "sign, sigp" specify the capture cross sections for electrons and holes respectively (in Atlas, Either the cross section or lifetime parameters can be used to define the capture parameters).

**Note:**

The back slash '\' at the end of the line of code informs Atlas that the next line of code should be considered as a part of the one preceding it. This is a useful tool to make the code more organized.

## 4.2.2.2. Materials and models specification

After specifying of the structure, the material characteristics must be specified, especially when material is not defined in the materials Silvaco library. The following line of code is an example of the Atlas syntax for material definition:

material mat=Ga2O3Si EG300=4.8 affinity=4 user.default=GaN \ USER.GROUP=SEMICONDUCTOR MUN=300 MUP=10 nc300=3.7e18 nv300=5e18 \ permittivity=11 VSATN=1e7 TAUN0=1e-9 TAUP0=1e-9 d.tunnel=1e-6

Where, "material mat" is the name specification of the material, "EG300" is the semiconductor bandgap in eV, "affinity" is the electron affinity in eV, "MUN, MUP" are the electron and hole mobilities in $cm^2s^{-1}V^{-1}$, "nc300, nv300" are referred to the effective density of states for electrons and holes respectively in $cm^{-3}$. "permittivity" is relative dielectric permittivity of the material, "VSATN" is the saturation velocity for electrons (cm/s), (TAUN0, TAUP0) are Specifies SRH lifetime for electrons and holes and "d.tunnel" specifies the maximum tunneling distance for the universal Schottky tunneling model in cm.

To get the simulation to the realistic level, a lot of complex dependencies of the device properties must be taken into consideration such as the mobility variation as a function of carriers' concentration. These complexities are not necessary in some cases. To avoid the additional calculations, Atlas provides independent models to describe every device property dependence alone, that can be activated separately. The accuracy of the results obtained depends on the models used in the simulation process. Physical models are specified using the "models" statement. An example of it:

models temp=300 FERMIDIRAC kla srh bgn fldmob heat.full Auger \ Arora UST print \
BBT.STD bb.a=8e7 bb.b=9e6 bb.gamma=2.6 \
incomplete inc.ion \
impact SELB AN1.val=0.79e6 BN1.val=2.92e7

Where every parameter of the parameters enables a specific model and the models presented in details in the previous sections, for example:

- "FERMIDIRAC": Specifies that Fermi-Dirac carrier statistics used.

- "srh": Specifies Shockley-Read-Hall recombination using fixed lifetimes (See section 3.3.3.1 "Shockley-Read-Hall recombination").

- "Auger": Specifies that Auger recombination (See section 3.3.3.2 "Auger recombination").

- "bgn": Bandgap narrowing model (See section 3.3.5.1 "Bandgap narrowing model").

- "fldmob": Parallel electric field dependent mobility (See section 3.3.4.2 "Parallel electric field dependent mobility").

- "heat.full": Enables all thermal sources and sinks (Joule heat, generation recombination heat, and Peltier Thomson heat) (See section 3.3.9 "Self-heating model").

- "UST": Enables the universal Schottky tunneling model (see section 3.3.8.3 "Tunneling theory").

- "BBT.STD": Specifies a standard band-to-band tunneling model (see section 3.3.8.4 "Band to Band tunneling theory").

- "incomplete": Accounts for incomplete ionization of impurities in Fermi-Dirac statistics (see section 3.3.7 "Incomplete ionization model").

- "SELB": Selects the impact ionization model described by Selberherr (See section 3.3.6 "Selberherr's impact ionization model").

- "print": Prints the status of all models, a variety of coefficients, and constants.

- "Arora": Specifies the low-field carrier mobility to impurity concentration and temperature.

There are also other models considered in different ways for example:

- The thermionic emission model can turned on by specifying any of the following parameters of the CONTACT statement: SURF.REC, E.TUNNEL, VSURFN, VSURFP, or BARRIERL.

- The Barrier Lowering Model can be turned on with the "BARRIER" parameter in the CONTACT statement.

- Fermi level pinning model can be activate automatically when metal/Semiconductor interfacial traps are considered.

In addition to the definition of the model, the parameter of the model must be specified. For example, the parameters "bb.a", "bb.b" and "bb.gamma" are the parameters related to Band to Band tunneling model, which are just the parameters $B_1$, $B_2$ and $B_3$ of equation (3.38) respectively, which are

specified in the models group. Other parameters can be defined on the MATERIAL statement for example the SRH lifetime for electrons and holes (TAUN0, TAUP0).

### 4.2.2.3. Numerical method selection

The device electrical properties are modelled using numerical solutions of fundamental partial differential equations that link the electrostatic potential with the carrier densities. For each mesh point of a given device, Atlas solves a system of three partial differential equations, which are the Poisson's equation and the holes and electrons equations of continuity. Atlas produces numerical solutions by calculating the values of the unknowns at each grid point of the device. An internal discretization process converts the original continuous model into a discrete nonlinear algebraic system. The discrete algebraic system is solved using an iterative process that refines the solution. The solution is obtained if the convergence is satisfied. Otherwise, the solution is stopped after either number of predefined iterations or after a solution failure is obtained. In this case, the system is considered as a non-convergent system. The nonlinear iterative method starts from an initial guess. Corrections are calculated by solving a linear version of the problem. The linear sub-problems are solved by using direct or iterative techniques. Atlas provides several numerical methods to calculate the solutions of semiconductor device problems. There are three types of solution techniques: (a) decoupled (GUMMEL), (b) fully coupled (NEWTON) and (c) BLOCK. The first method is the GUMMEL type, which is useful where the system of equations is weakly coupled but has only linear convergence. This method will solve for each variable in turn keeping the other variables constant (their most recently computed values), repeating the process until a stable solution is achieved. GUMMEL iteration typically tolerate relatively poor initial guesses, it converges relatively slowly.

The second method is NEWTON, which is useful when the system of equations is strongly coupled and has quadratic convergence. Unlike GUMMEL method, each iteration of the NEWTON method solves a linearized version of the entire non-linear algebraic system (the total system of unknowns together). This method requires a more accurate initial guess to obtain convergence and causes Atlas to spend extra time solving for quantities, which are essentially constant or weakly coupled. Therefore, each iteration takes a relatively long time (compared to GUMMEL) but it requires fewer iteration.

The final method is the BLOCK method, which can provide faster simulation times in situations where the NEWTON method struggles. BLOCK iterations involve solving subgroups of equations in various sequences. For example, in non-isothermal drift-diffusion simulation, specifying the BLOCK method means that NEWTON's method is used to solve the three basic equations (holes and electrons and Poisson's equations), after which the heat flow equation is solved in a decoupled step.

The solution can also be done using a combination of the previous mentioned methods by starting the solution with the GUMMEL method then switching to BLOCK or NEWTON if convergence has not occurred within a certain number of iterations. By adopting this strategy, GUMMEL method can refine initial guess to a point from which NEWTON iteration can converge.

Numerical methods are given in the METHOD statements of the input file. An example of a "METHOD" statement is:

METHOD GUMMEL NEWTON

### 4.2.2.4. Solution specification

After specifying the device structure, materials properties and physical models, the simulation is ready to be taken to the next step (the solution). This section of the input deck of Atlas is where the simulation does its calculations to solve for the device specified. It is divided up into four parts: LOG, SOLVE, OUTPUT and SAVE.

- **The "Log" statement:** The "LOG" statement creates a save file where all results of a run will be saved; Any DC, transient or AC data generated by "SOLVE" statements after the "LOG" statement will be saved. An example of "LOG" statement in which data is saved into file named "Schottky.log" is:

  LOG OUTFILE = Schottky.log

- **The "SOLVE" statement:** The "SOLVE" statement calculates information at one or more bias points for D.C. or A.C. First, a simplified initial solution must be run (which solves only Poisson's equation) to get an initial guess for the final solution. An example of "SOLVE" statement for a D.C analysis that ramps the anode voltage from 0.0 V to 2.0 V with 0.01 V steps:

  solve init

  solve vanode=0 vstep=0.01 vfinal=2 name=anode

- **"OUTPUT" and "SAVE" statements:** Some of the obtained results have different values along the structure (distribution) such as electron and hole densities, potential …etc. this requires a structural presentation. For that purpose, Atlas provides the possibility of saving these data into a structure file (.str) using the "save" statement. An example of the "save" statement which stores the data into a file named (Schottky.str) is:

  save outf= Schottky.str

### 4.2.2.5. Results analysis

After saving the results and the structure, the next step is the analysis of the obtained results through the extraction of the saved files. The extraction is based on two methods, the first is the extraction as data and the other type is through Figures.

For data extraction, "EXTRACT" command is provided within the DeckBuild environment. It allows to extract device parameters. The command has a flexible syntax that allows to construct specific EXTRACT routines. EXTRACT operates on the previous solved curve or structure file. By default, EXTRACT uses the currently open log file. To override this default, the name of a file to be used by EXTRACT is specified before the extraction routine. For example, the following command is used for current versus voltage extraction:

extract name="IV" curve(v."anode",i."cathode") outfile="IV.dat"

For plotting the results, TonyPlot graphical post processing tool is used. The commend "tonyplot" is used in Deckbuild after saving data and structure. Then the name of the file is specified as presented in the following example:

tonyplot Schottky.str

tonyplot IV.dat

The first command is used for the structure plot and the second for current versus voltage data plot. **Figures 4.6 (a)** and **(b)** show the plotted simulated structure and Current density variation versus the applied forward voltage using TonyPlot graphical post processing tool.
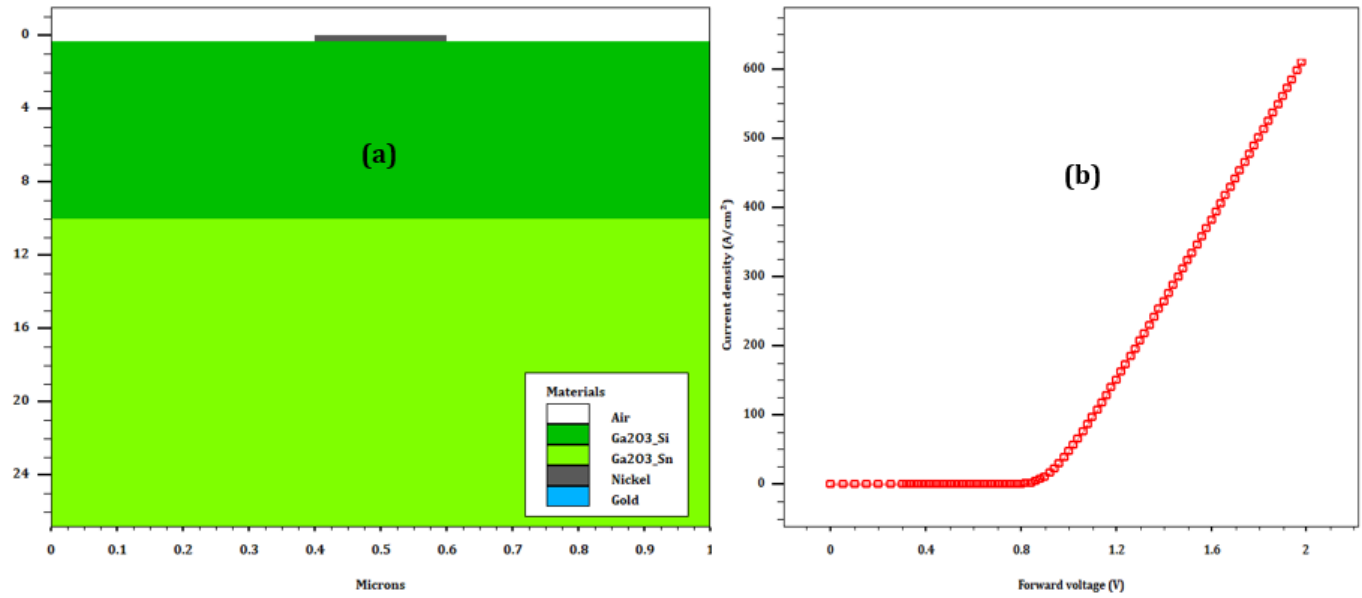
**Figure 4. 6 (a) The plotted simulated structure and (b) the extracted current density versus the applied forward voltage.**

# Chapter 5:

# Results and discussion

## 5.1. Introduction

This chapter presents the results of the work carried out and it is divided into two main parts. The first is modelling forward and reverse characteristics of a Schottky barrier diode (SBD) deposited by confined magnetic field based sputtering (CMFS) at high and low temperature. For this modelling a defect layer (DL) made of combination of NiO and β-Ga₂O₃ $((Ni_xGa_{1-x})_2O_3)$ was introduced. In addition, the effect of Ni workfunction and traps' concentration related to plasma and Ar bombardment were studied. Then an optimization based on the insertion of undoped layer at Ni/β-Ga₂O₃ interface and TiO₂ as an edge termination layer was carried out. The second part is to model another SBD deposited by EBE. The Ni workfunction, Ni/β-Ga₂O₃ interfacial traps' concentration and β-Ga₂O₃ surface electron affinity effects are modelled. Then, an optimization based on the insertion of a graphene layer was studied.

## 5.2. Modelling and optimization of Ni/β-Ga₂O₃ SBD deposited by CMFS

The β-Ga₂O₃ Schottky barrier diode (SBD) structure, based on an experimental structure is investigated as mentioned in Chapter two. It consists of a 300 nm thick Nickel, a Si-doped β-Ga₂O₃ layer deposited on a Sn-doped β-Ga₂O₃ substrate by HVPE which is used as a drift layer. This layer is used due to its high purity and provides a low resistance, a low on-resistance and a high breakdown voltage. A schematic representation of this SBD structure is shown in **Figure 5.1**. The thicknesses of Si-doped β-Ga₂O₃ and Sn-doped β-Ga₂O₃ are 10 and 650 $\mu m$ while their doping are $1 \times 10^{18}$ and $3 \times 10^{16}$ $cm^{-3}$, respectively.
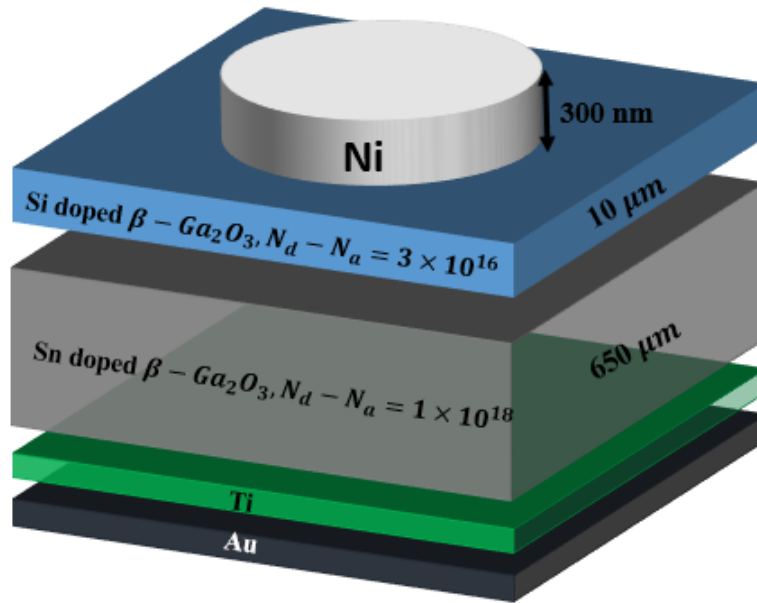
**Figure 5. 1 A schematic representation of the of β-Ga₂O₃ Schottky barrier diode (SBD) structure.**

### 5.2.1. Forward bias modelling

### 5.2.1.1. Effect of defective layer thickness

Plasma and Ar bombardment lead to the formation of gallium and oxygen vacancies in Si-doped β-Ga₂O₃ which manifest as surface defects (traps) in addition to the native bulk traps. The parameters of such traps are presented in **Table 5.1** [4].

The region in which these defects are created is referred to as a defected layer (DL) and is believed to be responsible for SBD degraded electrical characteristics [4]. Experimentally, the depth of surface traps depends on the ion impact energy (ICP power). Increasing ion energy leads to an increased penetration of Ar atoms which in turn causes an increase of the depth of surface traps, thus the DL thickness. This DL is different from β-Ga₂O₃ and therefore has different parameters (energy gap; affinity, etc...).

Its effect on the SBD electrical characteristics is therefore simulated in this work (by considering that defects of **Table 5.1** are localised in this DL and the SBD bulk). The effect of this DL thickness is shown in **Figure 5.2**. This result confirms the observation of [4], in which electrical characteristics degradation is related to this DL formation. In [4], etching is realised by the classical method based

## Chapter 5: Results and discussion

on exposing Si: β-Ga₂O₃ surface to plasma and Ar bombardment followed by metal contact deposition by EBE. In contrast to this method, CMFS is based on simultaneous etching and deposition. The SBD electrical characteristics, in this case, are therefore less degraded which is attributed to a thinner DL. In CMFS, Nickel atoms thermally diffuse to the Si-doped β-Ga₂O₃ layer during annealing as shown in **Figure 5.3**.

**Table 5. 1 Traps related to exposing β-Ga₂O₃ to plasma and Ar [4].**

| Traps | Trap level $(E_c - E)$ (eV) | Trap concentration $(cm^{-3})$ | Capture cross section $\sigma_n$ (cm²) | $\sigma_n/\sigma_p$ |
|---|---|---|---|---|
| **Near surface traps** | 0.8 | $5.2 \times 10^{15}$ | $2 \times 10^{-14}$ | 100 |
| | 1.05 | $8.9 \times 10^{15}$ | $2 \times 10^{-14}$ | 100 |
| | 2.3 | $2 \times 10^{15}$ | $1.5 \times 10^{-14}$ | 100 |
| | 3.1 | $4 \times 10^{16}$ | $5.6 \times 10^{-14}$ | 100 |
| **Bulk traps** | 0.7 | $5.4 \times 10^{13}$ | $2 \times 10^{-14}$ | 100 |
| | 0.8 | $4.2 \times 10^{14}$ | $2 \times 10^{-14}$ | 100 |
| | 1.05 | $3.2 \times 10^{13}$ | $2 \times 10^{-14}$ | 100 |
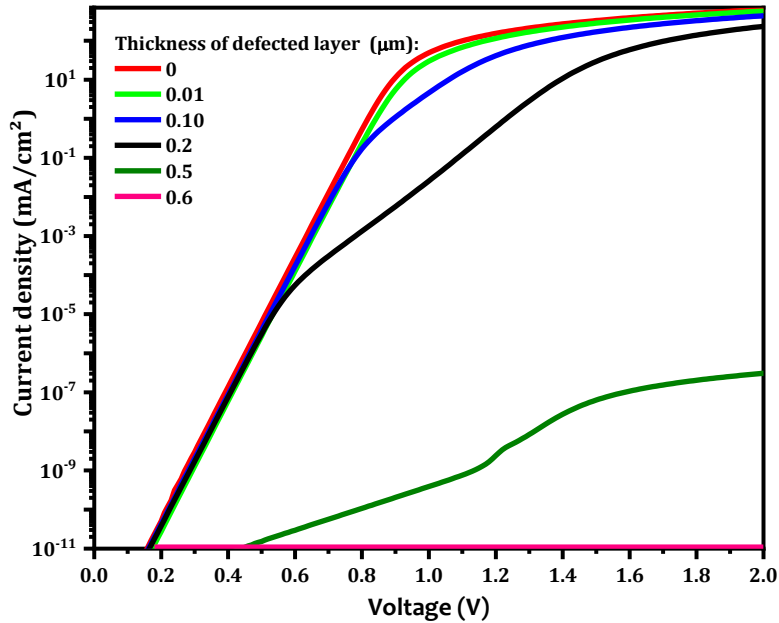
**Figure 5. 2 SBD simulated J-V characteristics for different interfacial layer thickness.**

A model is proposed in this work to explain the reduction of the DL thickness in CMFS. The relation between DL parameters and SBD electrical characteristics are consequently numerically simulated and compared to experimental measurements. In [1] the structure was examined by XRD for the formation of NiO related peaks, but could not be found due to the very thin interfacial layer. This fact was also confirmed using XPS depth profiling. As sputtering time in XPS is increased, O1s peak was gradually increased and shifted to higher energy. This is attributed to the change and transition between NiO and β-Ga$_2$O$_3$. Therefore, NiO is not the end product but it is an intermediate step in the formation of the proposed new material ((Ni$_x$Ga$_{1-x}$)$_2$O$_3$).

The formation of this material is also justified by the fact that diffused Ni atoms occupy Ga vacancies. These vacancies are amongst the defects created by plasma and Ar bombardment. Nonetheless, the formation of this new material is not certain (it is just a proposal), it can be for example of the form Ni$_x$Ga$_y$O$_z$. In any case, it is a material with different parameters and properties (gap and affinity which are important features in the operation of semiconductor devices). What is certain is that Ni diffuses in β-Ga$_2$O$_3$ as shown in SEM and TEM images presented in **Figure 5.3** [1] and may create acceptor levels (minority traps). Therefore and before detailing the development of the proposed model, the formation of a compensated β-Ga$_2$O$_3$ layer by the diffusion of Ni is tested (since Ni creates acceptor levels in β-Ga$_2$O$_3$ [1]). Ni usually crates an acceptor trap level at E$_v$+0.14, with a density of ⌣1.2×10$^{14}$

cm$^{-3}$ [97]. As shown in **Figure 5.4**, it is clear that the considered minority trap does not have a considerable effect. This result is due to the low compensation layer thickness (10 nm) compared to the SBD thickness (660 µm) and the low minority hole density in β-Ga$_2$O$_3$. So this assumption, and the formation of a heterojunction (p-type NiO/n-type Ga$_2$O$_3$), is excluded.
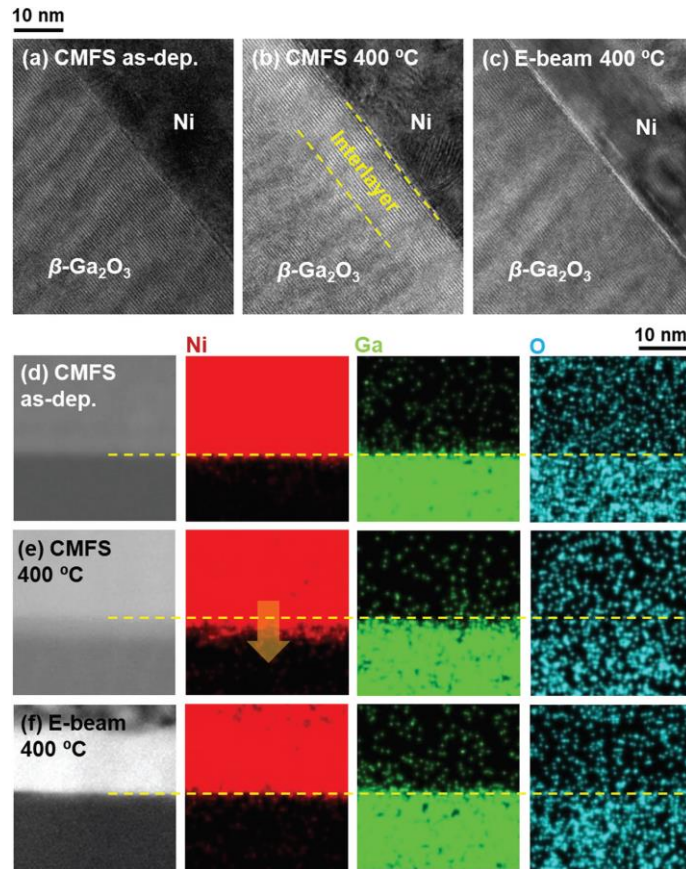


**Figure 5. 3 The cross-sectional TEM images of the Ni/β-Ga$_2$O$_3$ SBDs. (a) As-deposited CMFS sample and (b) after post-annealing at 400 °C. (c) The image of the 400 °C annealed sample, which the Ni was deposited by the EBE. (d–f) The EDS mapping images corresponding to the TEM images (a–c), respectively[1].**
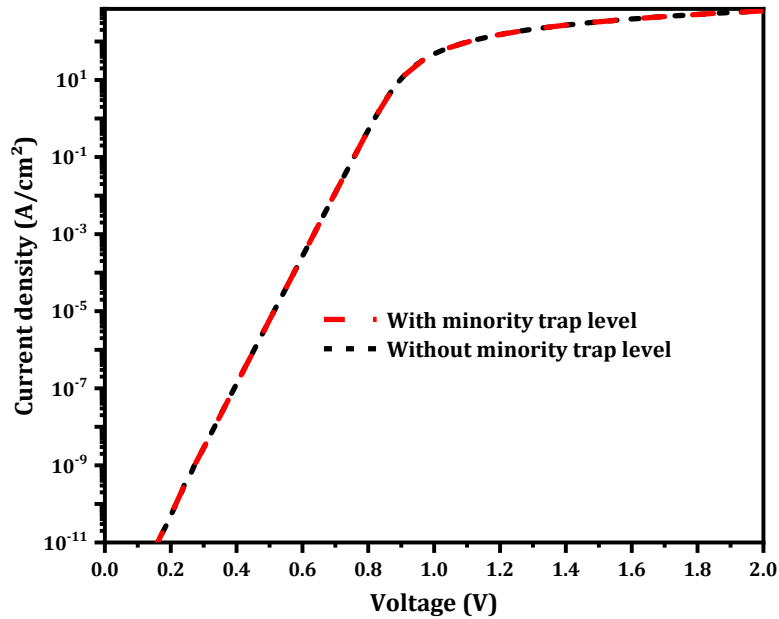
**Figure 5. 4 Simulated J-V characteristics with and without acceptor compensation in surface of the SBD.**

### 5.2.1.2. Effect of band gap and affinity of defected layer

Now a model is developed to explain the reduced J-V characteristics degradation of the CMFS SBD. The diffusion of Nickel atoms lead to the formation of an interfacial layer in the surface of β-Ga$_2$O$_3$. Ni atoms occupy Gallium vacancies, then interact with oxygen of β-Ga$_2$O$_3$ to form an Ni-O bound. In principle NiO is probably formed [98,99]. Then, NiO interacts with β-Ga$_2$O$_3$ to induce the formation of an $(Ni_xGa_{1-x})_2O_3$ compound at the interface. This idea is similar to that of $(Ga_{1-x}Al_x)_2O_3$ formation as presented in [100]. According to several references, Ni$_2$O$_3$ phase is only observed for temperatures above 500 K [101], or by special operations such as gamma irradiation [102]. In our work the diffusion of Ni atoms in the surface of Ga$_2$O$_3$ occurred at 400 °C. Furthermore, the formation enthalpy of Ni$_2$O$_3$ is -489.5 Kj/mol [103] which is greater than that of NiO which is equal to -239.7 Kj/mol [104]. Hence the possibility of NiO formation is more than Ni$_2$O$_3$ but this does not mean the absence of Ni$_2$O$_3$. This new formed compound definitely has different properties than NiO and β-Ga$_2$O$_3$. It is assumed here that bandgap and affinity of $(Ga_{1-x}Ni_x)_2O_3$ follow the simplified Vegard's law for compounds (neglecting higher order terms), thus:

$$T(x) = xT_{NiO} + (1-x)T_{Ga_2O_3} \tag{5.1}$$

Where $T$ is the bandgap/affinity and $x$ is the NiO fraction. Therefore, the bandgap and affinity of $(Ga_{1-x}Ni_x)_2O_3$ vary linearly with the NiO fraction. Probably, this compound formation explains the observation of Kim et al. [1] in which pure NiO is not formed in the interfacial layer.

## Chapter 5: Results and discussion

Now, the effect of NiO fraction on the SBD J-V characteristics is studied, and these are shown in **figure 5.5**. The current density in the high voltage region decreases with increasing NiO fraction in the compound. This is due to the increase of the series resistance. The simulated curves are shifted to the left because of the effect of the work function and the purpose of numerical simulation is to find the best fit. Numerical simulation cannot consider all parameters simultaneously, rather they are tested separately. The initial work function is 5.2 eV and this is a standard value given in most publications (for example Baker et al[105], Farzana et al[106] and Yao et al. [60] ). It was found that the best work function is 5.35 and not 5.2 eV (**Figure 5.6**). This best value is also acceptable according to literature. Also in this case, the most affected part of the curve is the series resistance region as shown in **Figure 5.6**.

An agreement between experimental and simulation results is observed for voltages higher than 1.1 V for NiO fraction of $0.08 < x < 0.1$. This small value of $x$ explains the fact that NiO is not revealed by SEM images of [1]. The origin if the kink around 1 V is due to traps as will be explained when their effect is studied in details later. For lower voltages the agreement is not achieved. Hence other possible causes (for example the Ni work function) are investigated.
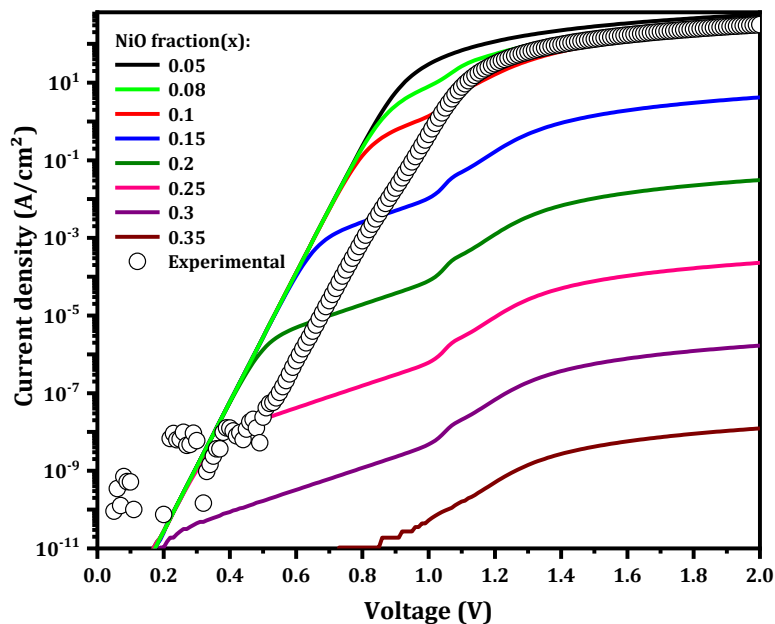


**Figure 5. 5 Simulated J-V characteristics for different NiO fractions and comparison with measurement.**

### 5.2.1.3. Effect of Nickel work function

In addition to Ni diffusion, oxygen and gallium atoms diffuse from β-Ga₂O₃ to Nickel as shown in **Figure 5.3**. It is expected, therefore, that Nickel work function will be affected. As shown in **Figure 5.6**, the best agreement between simulation and measurement is achieved for $\phi_m = 5.35$ eV. The small deviation from measurement is due to considered interfacial traps parameters (**Table 5.1**) which may not be accurate.
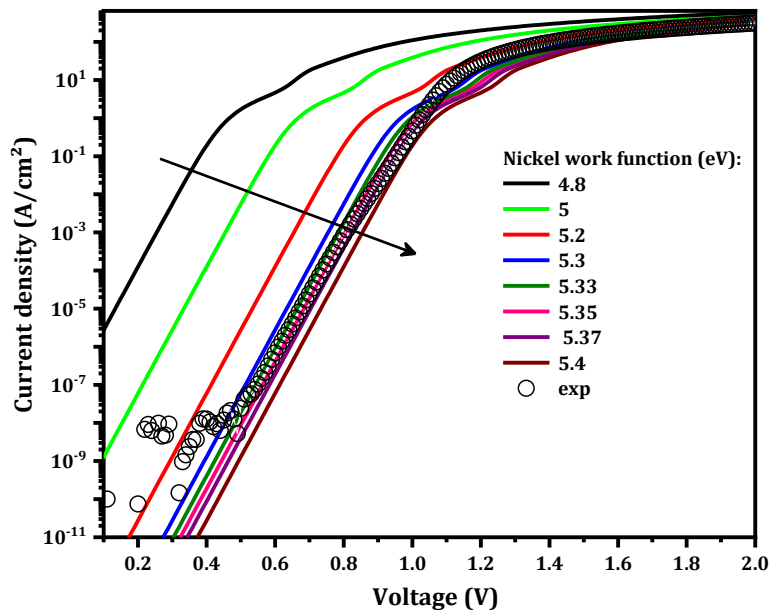


**Figure 5. 6 Simulated J-V characteristics for different Nickel work function and comparison with measurement at room temperature.**

### 5.2.1.4. Effect of the concentration of traps related to plasma and Ar bombardment

The concentration of the $(E_c - 1.05)$,$(E_c - 2.3)$ and $(E_c - 3.1)$ traps, in the DL, effect on the SBD J-V characteristics is studied. The choice of these traps is due to the fact that they either increase or are newly created by plasma and Ar bombardment and reduced by annealing. This effect is shown in **Figure 5.7** (a), (b) and (c), for the three traps respectively. First whenever any of the trpas parameters is changed, a kink appears. It is well known that the applied voltage can change the relative position of the trap with respect to the Femi level. This voltage (1 V) appears to be the value where the trap level crosses the Fermi level and hence changes its occupation. Well below or above this voltage, the

trap occupation does not change. That is, traps respond around and not below or above this voltage (knee).

First, it is observed that the third trap has the biggest effect. For all defects, a small density is enough to give acceptable comparison of simulations to measurements. The best densities of the three traps that gave the best comparison are $1 \times 10^{13} cm^{-3}$, $1 \times 10^{13} cm^{-3}$ and $1 \times 10^{14} cm^{-3}$ respectively and this comparison is shown in **Figure 5.8**. The comparison is not good at low voltages because of the measured J-V curve fluctuation which is due to the low current density which is outside the measurement domain of the measurement apparatus (4200A-SCS, Keithley).
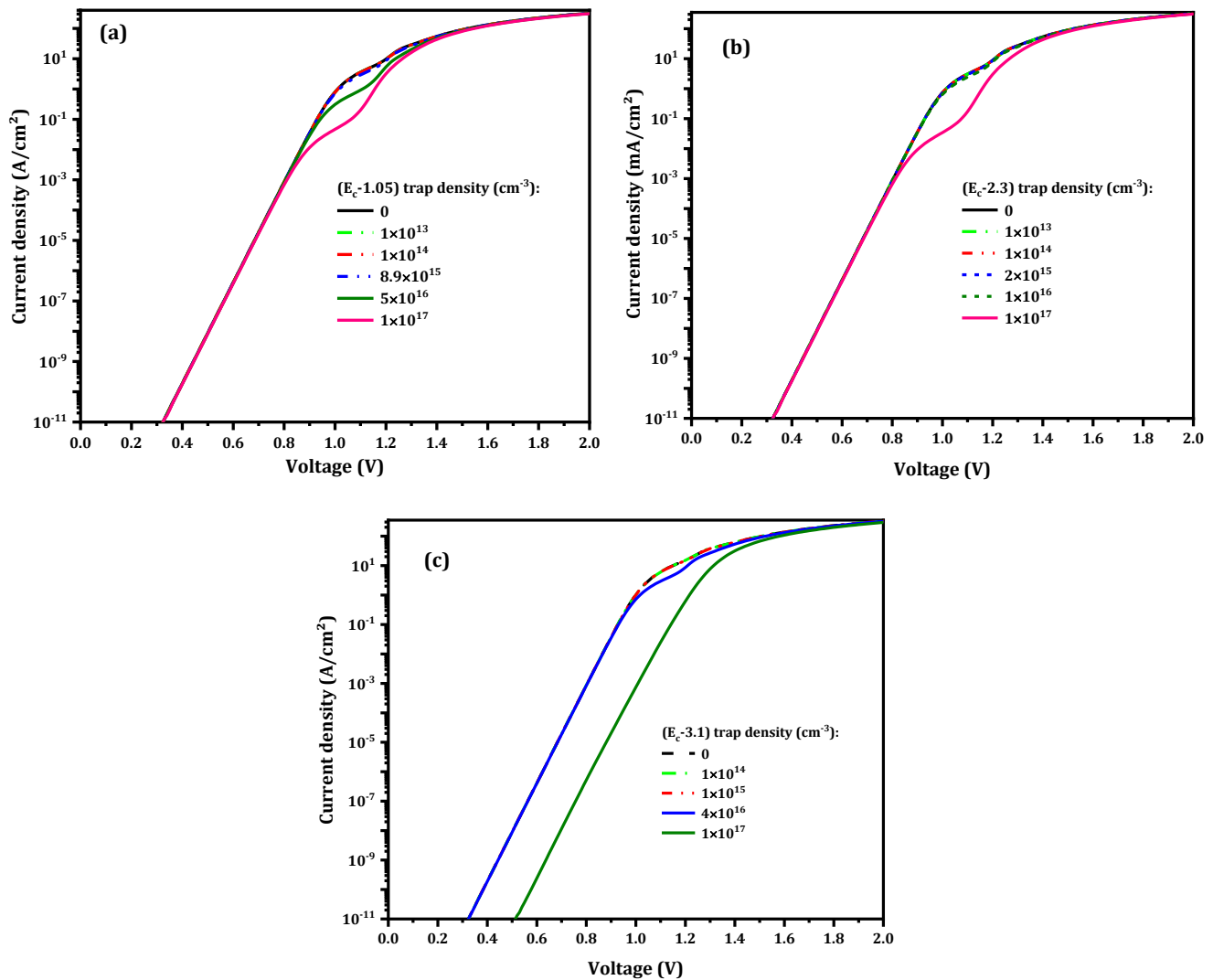


**Figure 5. 7 Effect of the traps density on the SBD electrical characteristics: (a) $E_c - 1.05\ eV$, (b) $E_c - 2.3\ eV$ and (c) $E_c - 3.1\ eV$ traps.**
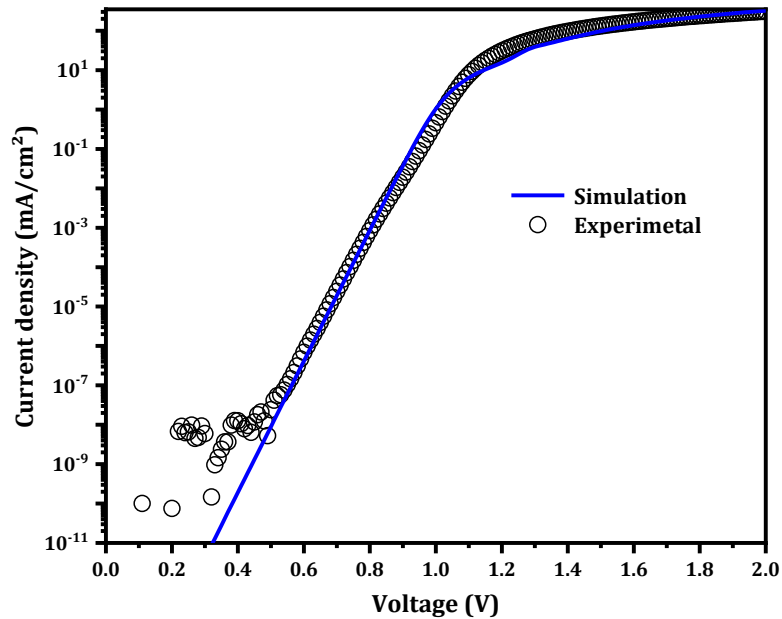
**Figure 5. 8 Comparison between simulation and experimental results at T=300 K.**

### 5.2.1.5. Temperature effect

All previous simulations were carried out at room temperature (300 K). Now, the temperature effect is studied. The simulated J-V characteristics are compared to measurements at different operation temperatures are shown in **Figure 5.9**. The agreement is very good at room temperature for the whole voltage domain as presented in **Figure 5.8**. But when temperature is increased, a deviation of simulations from measurements in the high voltage region (series resistance region) is observed and in most temperatures the simulation current is greater than measurement. This deviation is due to two reasons. The first is the effect of traps since as the temperature is increased, other traps "not considered in the simulation" may be activated because there are a possible additional traps (other tan considered in this work, **Table 5.1**) as reported in the review article of Galazka [3] . The second reason is the effect of the series resistance. The series resistance is usually related to the resistivity of the used layers of the SBD; that of the metal (Ni) and the semiconductors layers (Si doped $\beta$-Ga$_2$O$_3$ and Sn doped $\beta$-Ga$_2$O$_3$). Therefore, the increase in the series resistance as the temperature increases is greater for measurement then for simulation. This is due to the increase in the resistivity of the metal which is not studied in detail. There is also another possibility that the temperature coefficient of Ni is not constant all over the temperature range. Another possible cause is the fact that traps or at

least some of them may not be uniformly distributed. The main focus of the present this work is the Ni/β-Ga2O3 interface.
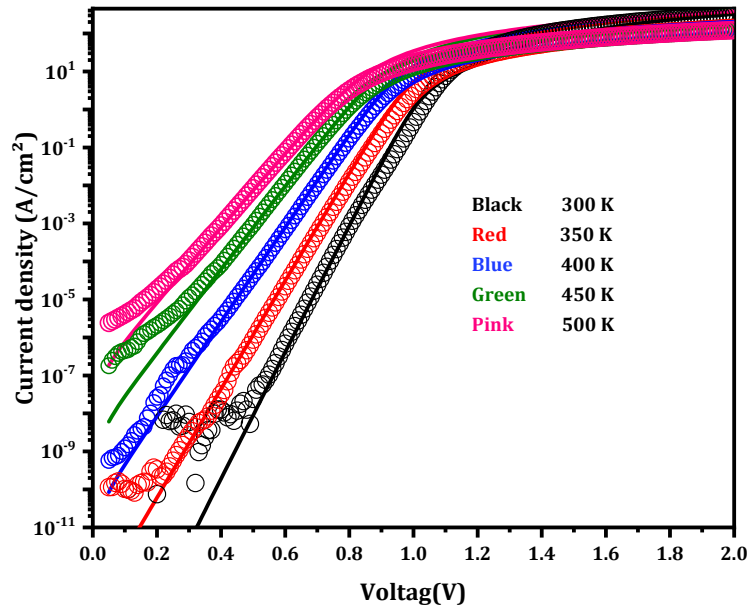


**Figure 5. 9  Simulated (solid lines) and measured (symbols) SBD electrical characteristics at different temperatures.**

### 5.2.1.6. Low temperature modeling

**Figure 5.10** shows a semi-logarithmic plot of simulated Ni/β $Ga_2O_3$ SBD forward-current density-voltage characteristics of with and without tunneling compared with measurements at 100 K with the consideration of $(Ni_xGa_{1-x})_2O_3$ compound and DL with tunneling mass of 0.03m0. At this temperature, the current-voltage characteristics are dominated by tunneling for voltages lower than 1.2 V. However, for higher voltages (series resistance region) thermionic emission dominates. A good agreement between simulation and measurement is therefore achieved when both Tunneling and Thermionic emission are considered. An ideality factor of 6.04 was obtained from the total current.

The high ideality factor value is related to the tunneling effect in agreement with the literature where high values at low temperatures are extracted [76,77]. However, an ideality factor of about 1.04 was extracted from the thermionic current component only.
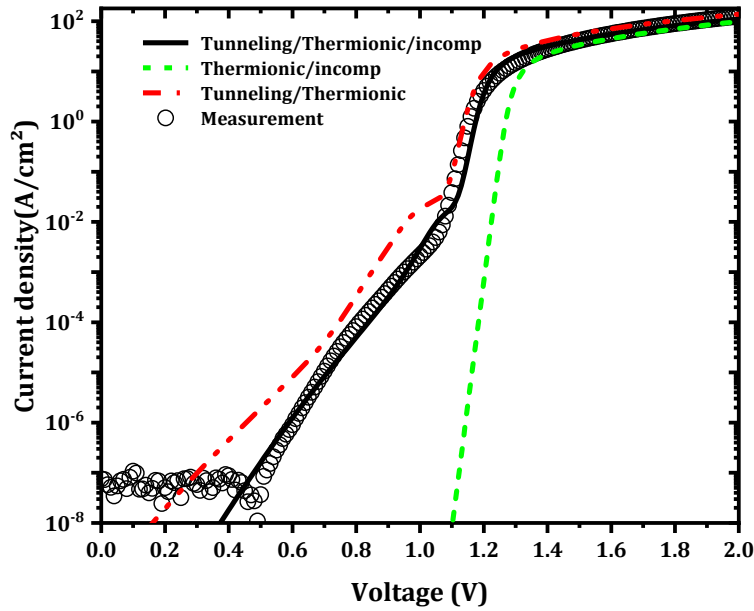
**Figure 5. 10 Simulated current-voltage characteristics with and without tunneling mechanism and compared to measurement.**

### 5.2.2. Leakage current modelling (reverse bias)

Now the reverse characteristics are modelled with special emphasis on the breakdown phenomena, which is one of the most important parameters in diodes or what is known as figures of merit.

Usually an inversion phenomenon is observed when the SBD is reverse biased, that is the semiconductor becomes p-type[86]. The electron concentration is decreased in the surface of Si-doped $\beta$-Ga$_2$O$_3$ with increase reverse voltage, this decrease is related to the drift of electron from the surface to the bulk in contrast to the free hole because of increase internal electric field for high reverse voltage[86]as presented in **Figure 5.11**. This phenomena is expected by the following equation shows the variation of free electron and hole concentration with reverse voltage[86]:

$$n = n_i \exp\left(\frac{q.V}{K_B T}\right) \tag{5.2}$$

$$p = n_i \exp\left(\frac{-q.V}{K_B T}\right) \tag{5.3}$$

Where $n_i$ and V are intrinsic concentration and reverse applied voltage, with increase reverse voltage, the free electron concentration decreased and free hole concentration increased according to

equations (3.2) and (3.3). So, under high voltage and with the formation of the mentioned inversion layer, the SBD behaves as a p-i-n diode. In the uniform electric field limit, the widely used Kane's model to determine the BBT generation rate G per unit volume is given by [92,93]:

$$G_{BBT} = B_1 . E^{B_2} e^{-(\frac{B_3}{E})} \qquad (5.4)$$

Where $B_1, B_2$ and $B_3$ are Band to Band model parameters and, for β-Ga$_2$O$_3$ equal to $2 \times 10^7 (cm^{-1} \cdot V^{-2} \cdot s^{-1})$, 2.5 and $9 \times 10^6 (V \cdot s^{-1})$ respectively. $E$ is the local electric field. **Figure 5.11** summarizes transport mechanisms (TE, UST, BBT and drift mechanism) at high reverse biased Ni/β-Ga$_2$O$_3$ SBD including the formation of the p-i-n structure near the surface of β-Ga$_2$O$_3$.
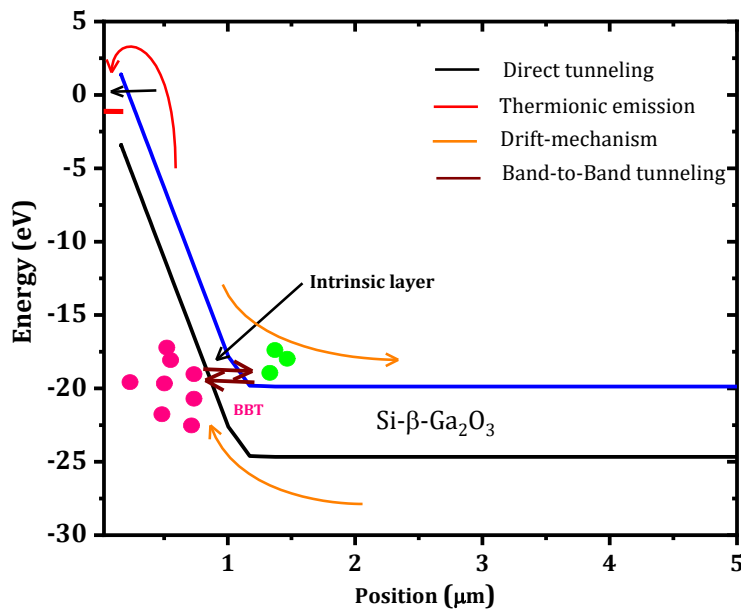


**Figure 5. 11 The energy band diagram of the Ni/β-Ga₂O₃ SBD showing the different models (TE, UST and BBT) used in the simulation of its reverse characteristics.**

In addition to the mentioned traps, (Ni$_x$Ga$_{1-x}$)$_2$O$_3$ interface formation and workfunction consideration, different models are considered in calculating the SBD electrical characteristics, their corresponding current-voltage behaviour compared to measurements are shown in **Figure 5.12** at room temperature.

## Chapter 5: Results and discussion

First, the point below which the simulated current is the same (region I) (whatever the model taken into account) and above which the current depends on the model taken into account is when inversion of the $\beta\text{-}Ga_2O_3$ surface occurs (region II). This voltage point is $\approx$-50 V (**Figure 5.12**).
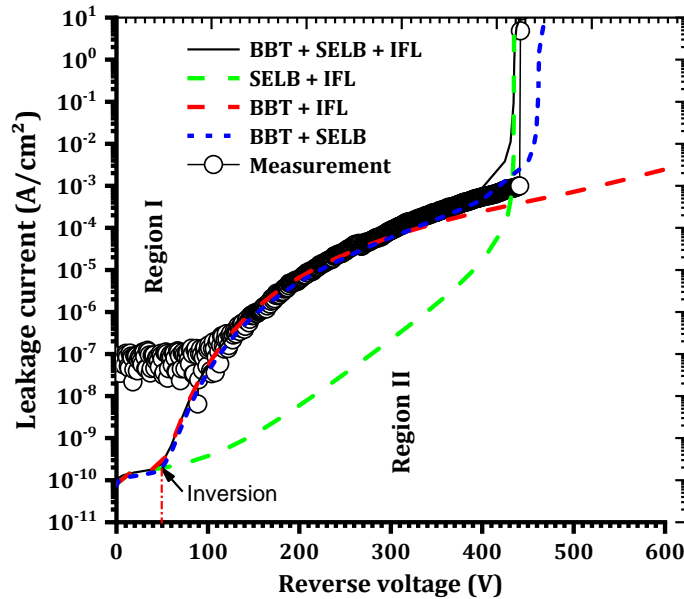


**Figure 5. 12 Simulated reverse current-voltage characteristics using BBT, SELB, and IFL models compared to measurements of Ni/β-Ga₂O₃ SBD at room temperature.**

For this, the carriers' concentration is plotted in **Figure 5.13** for a reverse voltage of -20 V (a) and 300 V (b). It is very clear that for -20 V (before inversion occurs) the carrier concentration (electrons and holes) is well below the intrinsic density at the $\beta\text{-}Ga_2O_3$ surface (0-0.3 µm) indicating a depletion region formation. However, for voltages higher than the inversion point, the carries' concentration (electrons and holes) is well above the intrinsic density at the $\beta\text{-}Ga_2O_3$ surface indicating the disappearance of the depletion region. Furthermore, hole concentration is higher than that of electrons indicating a p-type region formation. Beyond this region the first decreases while the second increases forming a short intrinsic region and then the normal initial n-region.
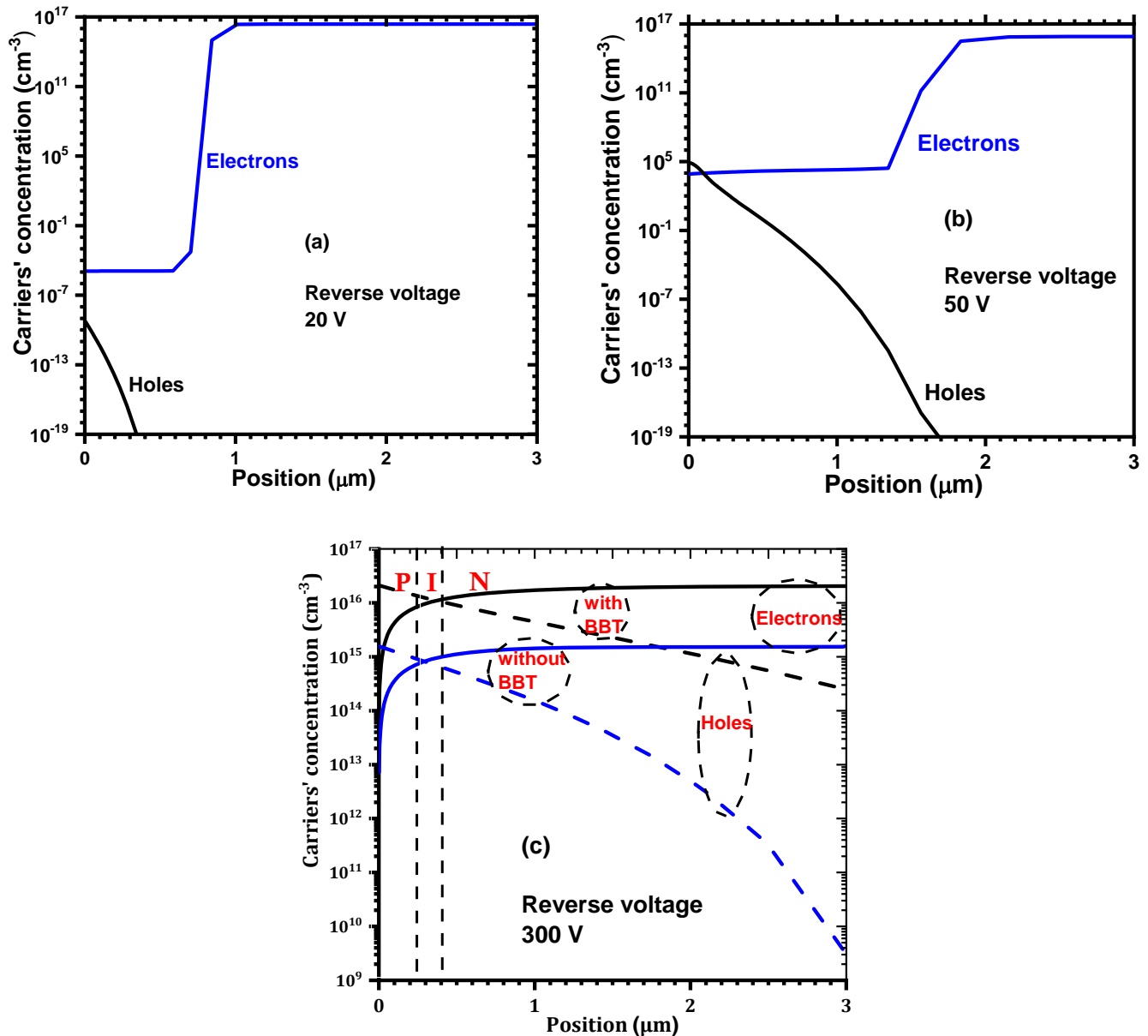
**Figure 5. 13 Free carries concentration distribution under (a) 20 V, (b) 50 V and (c) for 300 V reverse voltage with and without BBT being considered.**

For post-inversion voltage ($\geq$50 V reverse bias), the current depends on the conduction mechanism considered in the simulation. Since a p-type inversion layer is formed (**Figure 5.13 (b)**)and the barrier is higher (because of the high reverse voltage), it is expected that band to band tunnelling (BBT) to play an important role in the conduction mechanism. Therefore, it is seen that the simulated current fits measurement only when this mechanism is considered. When it is absent the simulated

current is inferior to measurement indicating a missing current component, which is no other than band to band tunneling current. This current is also enhanced by the increased carriers' density either side of the newly formed PIN structure as show in **Figure 5.13 (c)** where the carrier's concentration increases when BBT is considered.

Now the breakdown voltage appearance in the simulated current is clarified. As it can be seen in **Figure 5.12**, when SELB is not considered avalanche breakdown does not occur. However, combining the three models, a better fitting of simulated breakdown voltage to measurement is achieved as well as the whole variation of leakage current versus reverse voltage. The breakdown voltage and ON resistance ($R_{ON}$) extracted from the simulated curve using all models are 434 V and 2.13 $m\Omega \cdot cm^2$, respectively. $R_{ON}$ is extracted from the slope of the forward current versus voltage in the series resistance region of these characteristics. The obtained values from simulation are fairly close to those extracted from measurement which are 440 V and 2.79 $m\Omega . cm^2$ respectively.

### 5.2.3. Schottky barrier diode parameters modelling

As demonstrated in section 5.2.1, a model was proposed to achieve good agreement between simulated and measured temperature-dependent I-V characteristics, as shown in **Figure 5.9**. Usually, the extracted SBD parameters differ from the ideal case defined by the Schottky-Mott rule ( $\phi_B^0 = \phi_M - \chi$) and the unity ($\eta = 1$). But in reality, these are different.

This deviation from ideality is due to the effect of interfacial states due to plasma and Ar atoms bombardment. The ideality factor and the barrier height can be described by [83–85]:

$$n = \left[1 + \sum_t \frac{q\delta_t N_{ss}(t)}{\varepsilon_i}\right] \tag{5.5}$$

$$\phi_B = \phi_B^0 - \Delta\phi_B - \sum_t \frac{q\delta_t Q(t)}{\varepsilon_i} \tag{5.6}$$

Where $\phi_B^0 = 1.55 \ eV$ and $N_{ss}(t), \delta_t, \varepsilon_i, \Delta\phi_B$ and $Q(t)$ are the densities of interface states, the thickness of the interfacial layer, the dielectric constant of the interfacial layer, the Schottky barrier lowering related to the image force effect and the trapped charge per unit area, respectively. The Schottky barrier height $\phi_B$ and series resistance $R_s$ versus temperature are determined by the Sato and Yasumura method [107] in which, from the current-voltage equation, a function $F(V,T)$ is defined as [107]:

## Chapter 5: Results and discussion

$$F(V,T) = \frac{V}{2} - \frac{K_B T}{q} \ln\left(\frac{J}{A^* T^2}\right) = \phi_B + \frac{J.R_S}{n} + V\left(\frac{1}{\eta} - \frac{1}{2}\right) \tag{5.7}$$

This function (**Figure 5.14**) is used for $\phi_B(T)$ and $R_s(T)$ extraction.
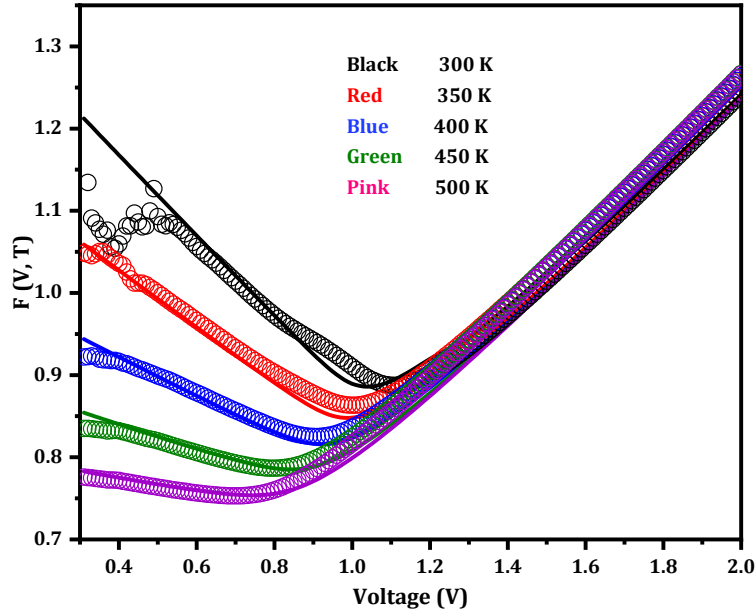


**Figure 5. 14 F(V, T) variation versus temperature and voltage for simulation (solid lines) and measurement SBD deposited by CMFS.**

Now, from equation (5.7), it can be shown that the barrier height $\phi_B(T)$ is given by [107]:

$$\phi_B(T) = F_{min}(V,T) - \left(\frac{2}{\eta} - 1\right)\frac{K_B T}{q} + V(F_{min})\left(\frac{1}{\eta} - \frac{1}{2}\right) \tag{5.8}$$

The series resistance is extracted from F(V, T) function as [107]:

$$R_S = \frac{(2-\eta)\,K_B T}{q\,J(F_{min})} \tag{5.9}$$

Where $J(F_{min})$ is the current corresponding to the minimum value of F(V, T) at a fixed temperature. The ideality factor is calculated from the slope of the linear region of low forward bias ln (J) versus voltage and can be written as [108]:

$$\eta = \frac{q}{K_B T}\left(\frac{dV}{d(\ln(J))}\right) \tag{5.10}$$

The extracted parameters are shown in **Figure 5.15**. All parameters are temperature dependent. The ideality factor is almost constant at $\approx 1.08$. This increase is related to the series resistance increase (shown in the same figure) and related to the inhomogeneous of $\phi_B$ which is attributed to the defects at the Ni/$\beta$-Ga$_2$O$_3$ interface [109,110].

To understand $R_s$ increasing with increasing temperature, it is accepted that $R_s$ is the sum of Nickel-metal, β-$Ga_2O_3$ and interfacial layers resistances, and thus given by:

$$R_s(T) \approx R_{Ga_2O_3}(T) + R_{Nickel}(T) + R_{\text{interfacial-layer}}(T) \qquad (5.11)$$

$R_{Ga_2O_3}(T)$ increases with increasing temperature because the free electrons concentration decreases because of the recombination in the defects near the interface with the defected layer as shown in **Figure 5.16** but becomes constant further away from this interface.
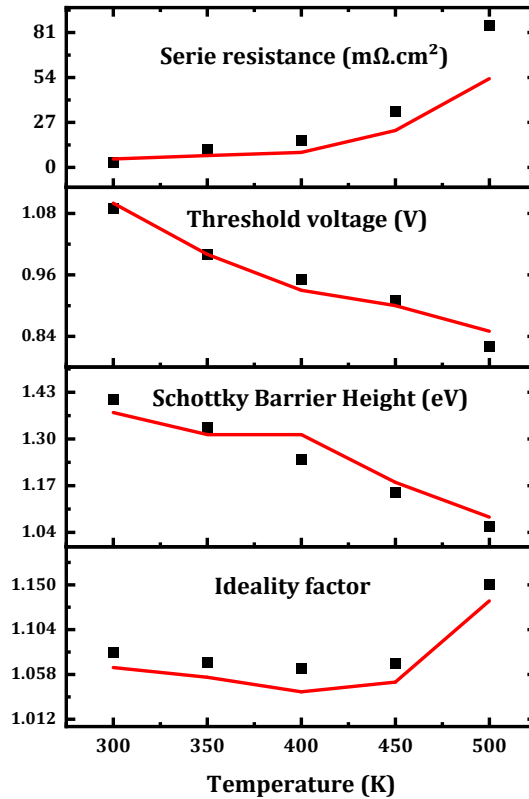


**Figure 5. 15 The temperature-dependent SBD parameters (ideality factor, Schottky barrier height, threshold voltage and series resistance).**

But the overall resistance increases with increasing temperature. $R_{Nickel}(T)$ decreases because of the increased collisions (reduced mobility) in the metal (Nickel) contact. Meanwhile, the free electron concentration decreases in the interfacial layer so that its resistance $R_{\text{interfacial-layer}}(T)$ increases. This free electron concentration decrease is related to the increased recombination in the interfacial defected layer because of the presence of the intrinsic and extrinsic traps in the interfacial layer. With increasing temperature, the recombination rate in the interfacial layer increases, and this leads to a

decrease in free electrons concentration as presented in **Figure 5.16** and thus an increase in $R_{\text{interfacial−layer}}(T)$. Thus, the overall increase in resistance (series resistance) is the result of the increase in $R_{\text{Nickel}}(T)$ and $R_{\text{interfacial−layer}}(T)$.
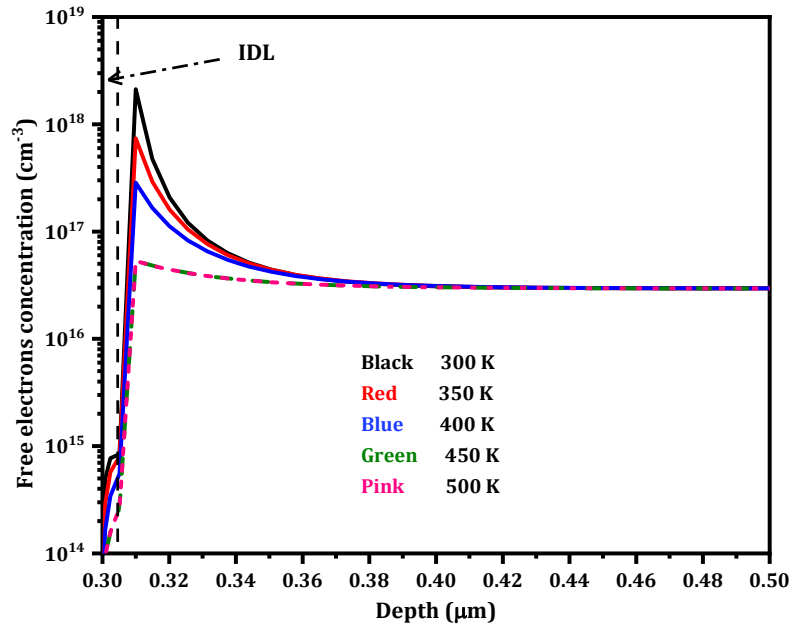


**Figure 5. 16 Free electrons profile in the surface of the SBD (IDL and β-Ga₂O₃ surface) at a forward voltage of 2.5 V.**

As for $\phi_B(T)$, it decreases as the temperature is increased from 300 K to 500 K . This is explained by the Gaussian distribution of the barrier height (inhomogeneity) [11, 25] as schematized in **Figure 5.17**. At low temperatures, carriers are located near the peak of the inhomogeneous barrier and can be transferred to Nickel easily, because it needs only a low thermal energy. When temperature increases, more carriers at lower energies surmount the barrier and hence the barrier appears to be smaller. Also when temperature increases the saturation current $(J_s)$ increase, which leads to a $\phi_B$ decrease. To further analyse the temperature dependent of $\phi_B$, for the inhomogeneous barrier, the current is given by [8,109]:

$$J(V) = \int_{-\infty}^{+\infty} J(\phi_B, V, T)P(\phi_B)d\phi_B \qquad (5.12)$$

Where $P(\phi_B)$ is the Gaussian distribution of inhomogeneous barrier and $J(\phi_B, V, T)$ is the thermionic current density. From this model, the apparent Schottky barrier height is given by [110–113]:

$$\phi_{app}^B(T) = \overline{\phi_{app}^B}(T) - \frac{\sigma_s^2}{2K_B T/q} \tag{5.13}$$

Where $\overline{\phi_{app}^B}(T)$ and $\sigma_s$ are the mean barrier height and standard deviation within the Gaussian distribution, respectively. With the assumption of temperature-dependent, $\overline{\phi_{app}^B}(T)$ is given by [111]:

$$\overline{\phi_{app}^B}(T) = \overline{\phi_{app}^B}(T = 0\ K) + \alpha_{\overline{\phi_B}}T \tag{5.14}$$
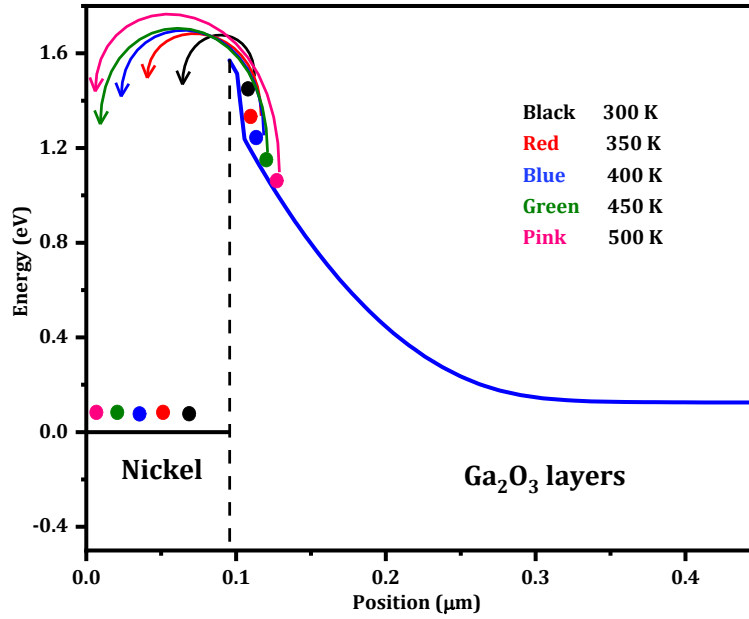


**Figure 5. 17 The Gaussian distribution of barrier height inhomogeneity resulting from Ga₂O₃:NiO compound interfacial layer.**

By substituting $\overline{\phi_{app}^B}(T)$ equation into $\phi_{app}^B(T)$ equation, the following relation is obtained:

$$\phi_{app}^B(T) = \overline{\phi_{app}^B}(T = 0\ K) + \alpha_{\overline{\phi_B}}T - \frac{\sigma_s^2}{\frac{2K_B}{q}}\frac{1}{T}$$

$$\approx \overline{\phi_{app}^B}(T = 0\ K) + \alpha_{\overline{\phi_B}}T - \delta\frac{1}{T} \tag{5.15}$$

To find the value of each coefficient, three temperatures were chosen and equation (5.15) is converted to a matrix, thus:

$$\begin{bmatrix} \overline{\phi_{app}^B}(T = 0\ K) \\ \alpha_{\overline{\Phi_B}} \\ \delta \end{bmatrix} = \begin{bmatrix} 1 & T_1 & \frac{1}{T_1} \\ 1 & T_2 & \frac{1}{T_2} \\ 1 & T_3 & \frac{1}{T_3} \end{bmatrix}^{-1} \begin{bmatrix} \phi_{app}^B(T_1) \\ \phi_{app}^B(T_2) \\ \phi_{app}^B(T_3) \end{bmatrix} \tag{5.16}$$

The obtained coefficients are presented in **Table 5.2**.

**Table 5. 2 Extracted mean barrier height $\overline{\phi_{app}^{B}}$ , standard deviation $\sigma_s$ and $\alpha_{\overline{\phi_B}}$ according to Gaussian distribution.**

|  | $\sigma_s (meV)$ | $\alpha_{\overline{\phi_B}}$ (mV/K) | $\overline{\phi_{app}^{B}}(T = 0\ K)(eV)$ |
|---|---|---|---|
| **Experimental** | 153 | $-2$ | 1.90 |
| **Simulation** | 161 | $-2.3$ | 1.87 |

Finally, the threshold voltage is determined from, the linear region tangent intersection with the voltage axis. The decrease in the threshold voltage is related to the decrease in Schottky barrier height ($\phi_{app}^{B}$) versus temperature as shown in **Figure 5.15**. The following relation gives an explanation of this dependence [13]:

$$V_{Th}(T) \approx \phi_{app}^{B}(T) - K_B T ln(\frac{2}{N_d}.(\frac{2\pi m_e^* K_B T}{h^2})^{3/2})  \tag{5.17}$$

Where $N_d$, $m_e^*$, $h$ and $K_B$ are doping concentration, electron effective mass, Blank constant and Boltzmann constant respectively.

### 5.2.4. Optimizations of Ni/β-Ga₂O₃ SBD deposited by CMFS

The simulated SBD J-V characteristics are successfully compared to measurement at room temperature for forward and reverse voltages. This good agreement is achieved by developing a model to represent the effect of Ni diffusion in the surface of β-Ga₂O₃. The validity of the proposed model is further demonstrated by simulating the temperature dependence of the J-V characteristics and comparison with measurement.

Now, optimizations are performed in the aim to reduce leakage current, enhance breakdown voltage and decrease on-resistance. The optimization is based firstly on the insertion of an undoped layer between Ni and Si doped β-Ga₂O₃ and its thickness effect on the leakage and forward current is studied. Then optimizations based on the insertion of $TiO_2$ Edge termination is considered.

### 5.2.4.1. Undoped layer insertion effect

Firstly, an optimization based on the insertion of an undoped layer between Ni and Si doped $\beta$-$Ga_2O_3$ As shown in **Figure 5.18** and its thickness effect on the leakage and forward current is studied.
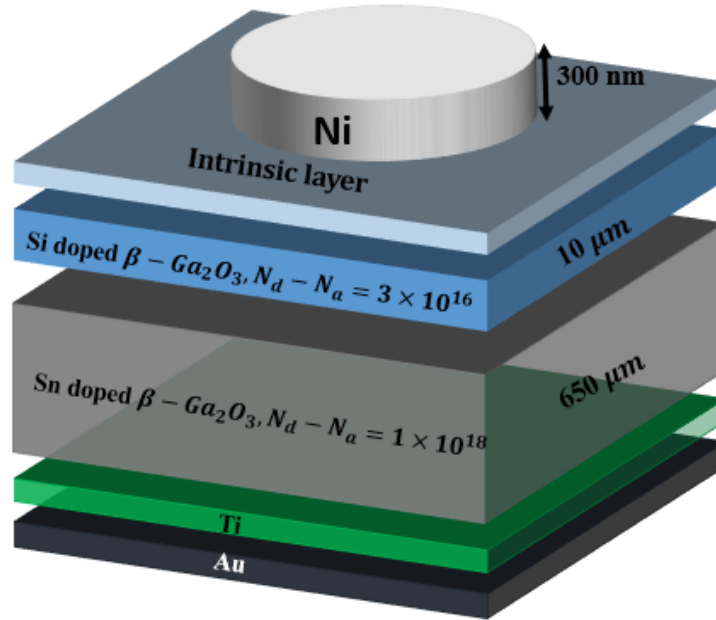


**Figure 5. 18  A schematic view of the structure with an undoped β-Ga₂O₃ layer between Ni and Si doped β-Ga₂O₃.**

**Figure 5.19** shows the obtained reverse leakage current variation with undoped layer thickness. With increasing thickness, leakage current decreases, and breakdown voltage attained 550 V for a thickness of 1.5 $\mu m$. These variations are due to the increase of the depletion region width as shown in the insert of **Figure 5.19.**
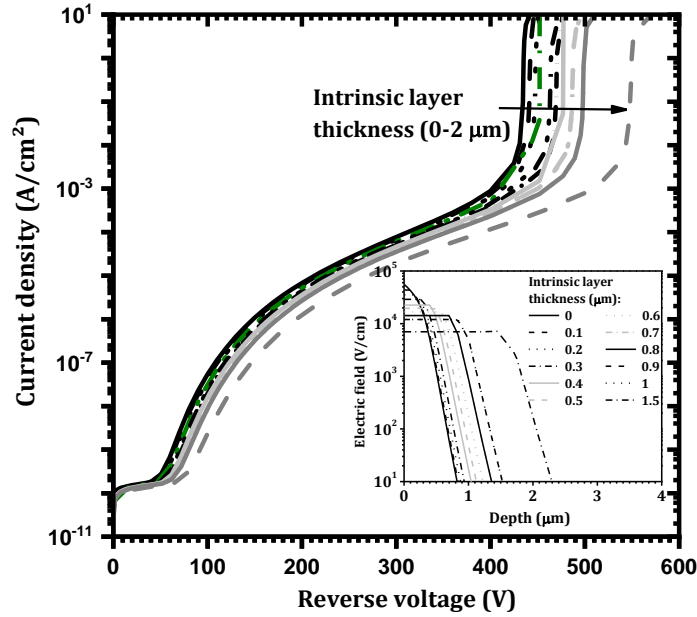
**Figure 5. 19 The effect of the undoped layer thickness, inserted between Ni and drift layer, on the simulated reverse characteristics. The inset is the effect on the depletion thickness and the electrical field of the PIN structure.**

In addition, when the undoped layer thickness increased the forward current is affected as presented in **Figure 5.20**.

Baliga's figure of merit (BFOM) is used to characterize the variation of on-resistance and breakdown voltage by the following equation[114]:

$$BFOM = \frac{\varepsilon \mu_n E_{cr}^3}{4} = \frac{V_b^2}{R_{ON}} \qquad (5.18)$$

Where, $V_b$ is the avalanche breakdown due to the impact ionization model, $R_{ON}$ is the specific on-resistance, $\varepsilon$ is the material permittivity, $\mu_n$ is the electron mobility and $E_{cr}$ is the critical electric field. *BFOM* reaches a maximum value of $9.48 \times 10^7 \, W/cm^2$ for an undoped layer thickness 0.4 $\mu m$ as presented in the insert of **Figure 5.20**. The corresponding $R_{ON}$ and breakdown voltage are 2.28 $m\Omega \cdot cm^2$ and -465 V, respectively. Thicknesses lower than 0.4 $\mu m$ provide low breakdown voltage and BFOM while above this limit $R_{ON}$ increases which leads to a BFOM decrease. Consequently, 0.4 µm is the optimal undoped layer thickness in this structure.
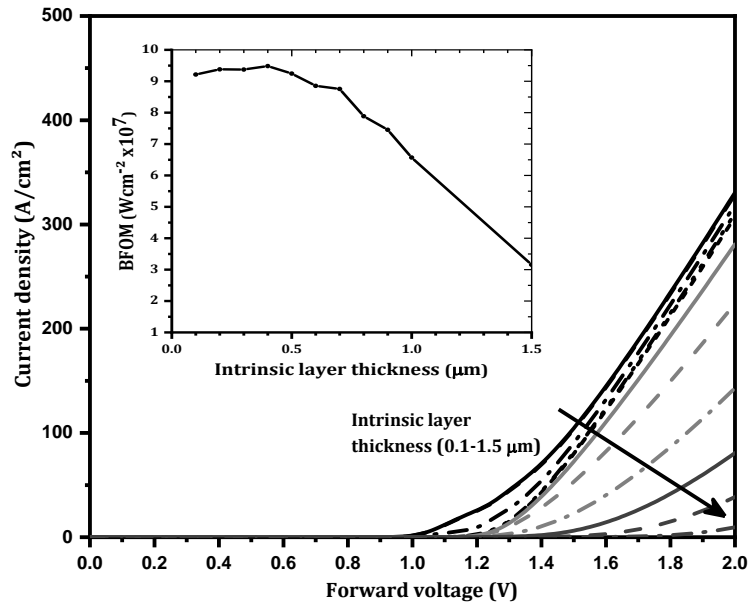
**Figure 5. 20 The effect of the undoped layer thickness on the simulated forward characteristics. The inset is the effect of the undoped layer thickness on the Baliga's figure of merit.**
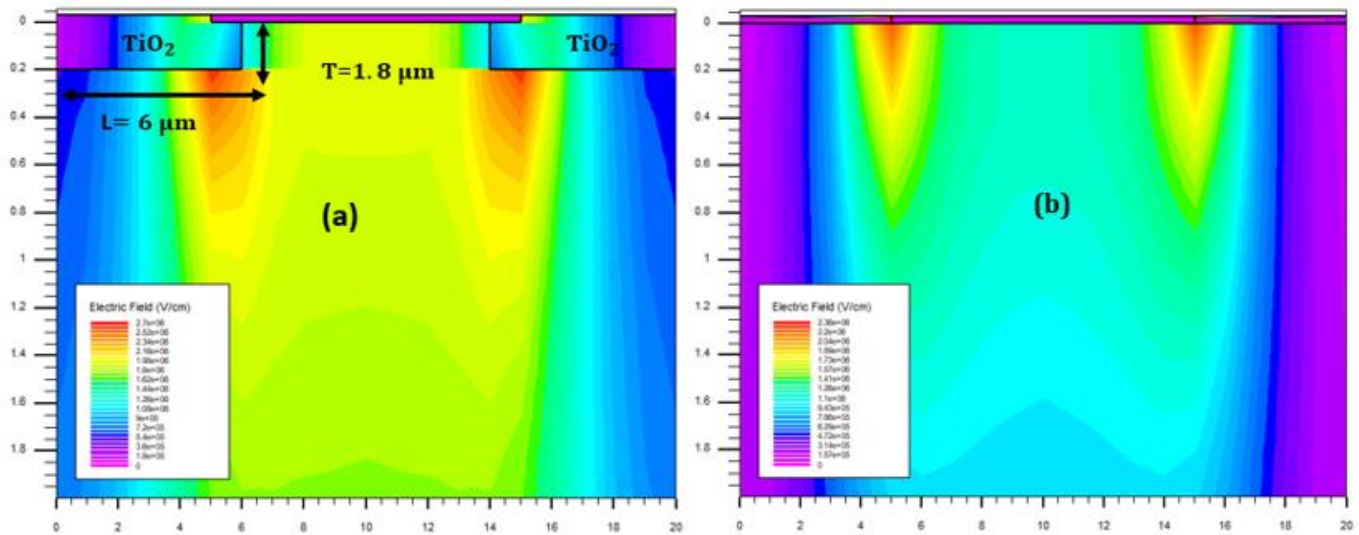


**Figure 5. 21 2D electric field distribution: (a) with (b) without TiO₂ as insulator surface edge termination structure.**

Experimentally, Galazka [3] demonstrated the formation of an electron depleted surface layer (surface insulating layer), while the bulk remains doped and semiconducting. This has been demonstrated by annealing $\beta$-$Ga_2O_3$ sample in an oxidizing atmosphere at or above 1000 °C for 20 h

Chapter 5: Results and discussion

[3]. As a suggestion for this undoped layer deposition in the SBD structure, the substrate and the drift layer system can be annealed under high temperature in an oxidizing atmosphere before the Ni contact deposition. The thickness of this undoped layer depends on temperature and oxidizing time.

### 5.2.4.2. TiO$_2$ Edge termination effect

To further enhance the SBD breakdown voltage, leakage current and *BFOM,* an edge termination technique has been proposed since there are many suitable designs [12,62,90,115]. It is known that SBD contains a sharp edge at the periphery of the front contact which induces an electric field higher than along the interface between the front contact and the bulk depletion region (corner field crowding). This causes a serious reduction of the breakdown voltage [12,90]. To avoid the corner field crowding, an insulator plate as edge termination is suggested. One of the candidate insulator is TiO$_2$ with a high dielectric constant between 30 and 100 [116,117] compared to other insulators (SiO$_2$, HfO$_2$ ...)[90]. The most important properties of insulating TiO$_2$ for edge termination role are the dielectric constant and the bandgap. The default dielectric constant and the bandgap considered are 80 and 3.2 eV respectively [117,118]. The proposed design based on TiO$_2$ plate (0.2µ$m$ thickness, 6µ$m$ length) as edge termination insulator is presented through the electric field distribution in **Figure 5.21 (a)** and **(b)**.

It is noted that the TiO$_2$ plate moves the highest electric field at corners to the bulk and this means that the breakdown occurs away from the surface of the Schottky diode. Consequently, as presented in **Figure 5.22,** the breakdown voltage and specific on-resistance reach 927 V and 1.85 $m\Omega \cdot cm^2$ respectively (compared to 465 V and 2.28 $m\Omega.cm^2$ without TiO$_2$ insulator) and the extracted *BFOM* is $4.4 \times 10^8 \ W/cm^2$**.**

The decrease in the specific on-resistance results from the decrease in the recombination rate at the surface of the SBD as presented in the vertical variation of recombination rate cutline at x= 15 µm (the dotted line); which corresponds to the edge of Ni Schottky contact; in **Figure 5.23**(a) after TiO2 insulating layer was inserted. The numerical vertical variation of recombination rate is shown in **Figure 5.23** (b) which shows a cutline of the contour of the recombination rate variation.
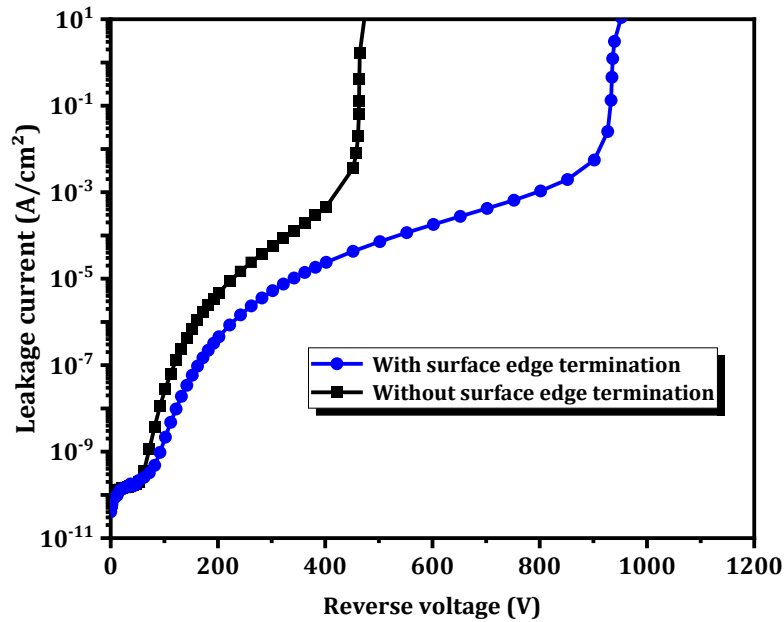
**Figure 5. 22 Reverse J-V characteristics of SBD with and without TiO$_2$ edge termination.**
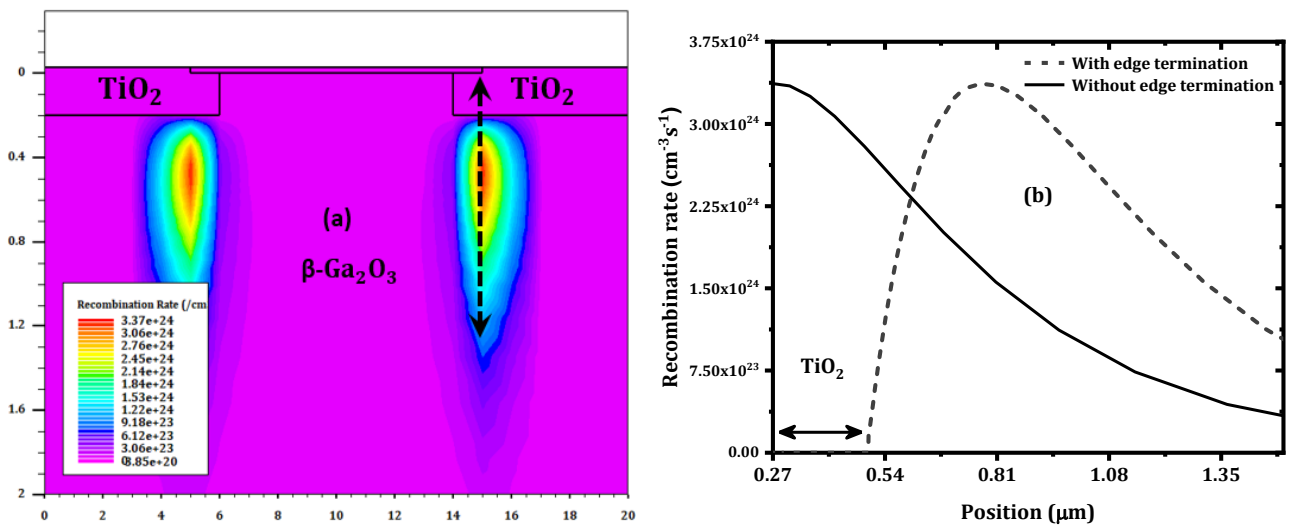


**Figure 5. 23 (a) Recombination rate contour when edge termination is considered and (b) cutline of the recombination rate distribution with and without edge termination for x=15 µm.**

This results in an increase in the carrier concentration which induces a decrease in the specific on-resistance. Furthermore, the specific on-resistance depends on the current variation and when edge termination is used, an increase in forward current was obtained as a result of the surface recombination decrease.

Further improvement can be made by increasing TiO$_2$ thickness. As shown in **Figure 5.24**, it can be observed that the leakage current decreases while breakdown voltage increases. The breakdown voltage reaches 1466 V for a 2 µm TiO$_2$ thickness. This is explained by further shifting of the electric field peak away from the edge of the front contact (located at x=15 µm) as shown in the insert of **Figure 5.24**.
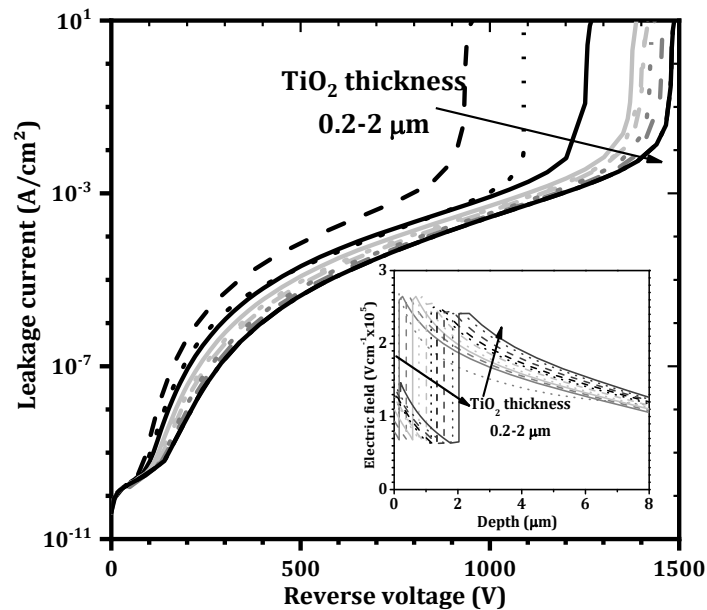


**Figure 5. 24 Reverse J-V characteristics of SBD for different TiO₂ thicknesses. The corresponding electric field is shown in the insert at x coordinate =15 µm.**

In addition to the leakage current and breakdown voltage enhancement, BFOM is extracted for different TiO₂ thicknesses and this relation is presented in **Figure 5.25**. BOFM saturates at $1.09 \times 10^9 \, W/cm^2$ at ≈1.8 µm with the corresponding $R_{ON} = 1.98 \, m\Omega.cm^2$. So the optimal value for TiO₂ thickness is ≈1.8 µm.
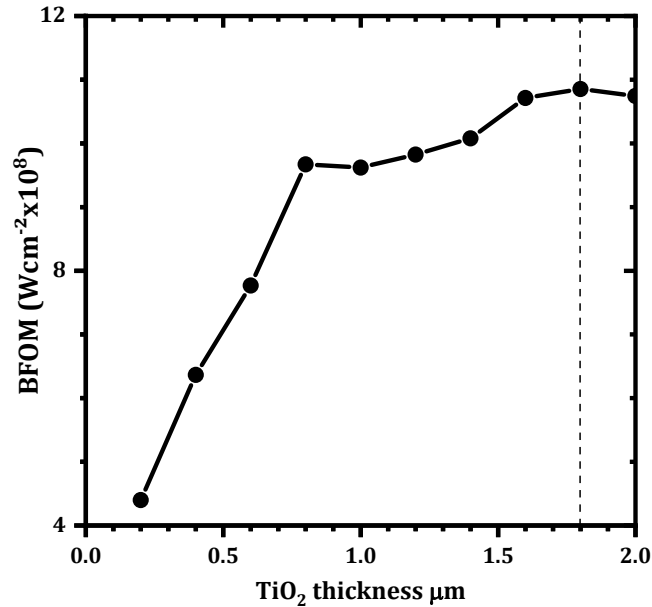
**Figure 5. 25 Baliga's figure of merit variation versus TiO$_2$ thickness.**

## 5.3. Modelling and optimization Ni/β-Ga$_2$O$_3$ SBD deposited by EBE

After modelling and optimization SBD deposited by CMFS, $(Ni_xGa_{1-x})_2O_3$ compound formation in the interface between Ni and β-Ga$_2$O$_3$ is used for SBD modeling in addition to traps related to plasma and Ar bombardment. The optimization based on the insertion of undoped layer between Ni and drift layer. Then the effect of TiO$_2$ Edge termination is studied. Now, the SBD deposited by EBE is studied. Consequntly, an optimization based on the insertion of graphene layer between Ni and Si-doped β-Ga$_2$O$_3$. However, Ahlberg et al.[119] reported the damage of graphene layer after exposed to Ar atoms. So, experimentally we expect the degradation of SBD when Ni deposited by CMFS after the graphene layer deposited on the Si-doped β-Ga$_2$O$_3$. Because as mentioned in the previous paragraphe CMFS deposition method is used Ar and plasma for deposition. So EBE method proposed for Ni contact deposition for this optimization because of the absence of plasma and Ar bombardment. For this study a new output J-V reprodused then the effect of graphene layer in the SBD outputs are studied.

### 5.3.1. Modelling Ni/β-Ga₂O₃ SBD deposited by EBE

As presented in **Figure 5.26,** a huge disagreement between simulation and measurement is studied . This deviation is related to the Nickel workfunction, interface traps concentrations and β-$Ga_2O_3$ surface electron affinity deviation from their real values as we will show in the next steps.
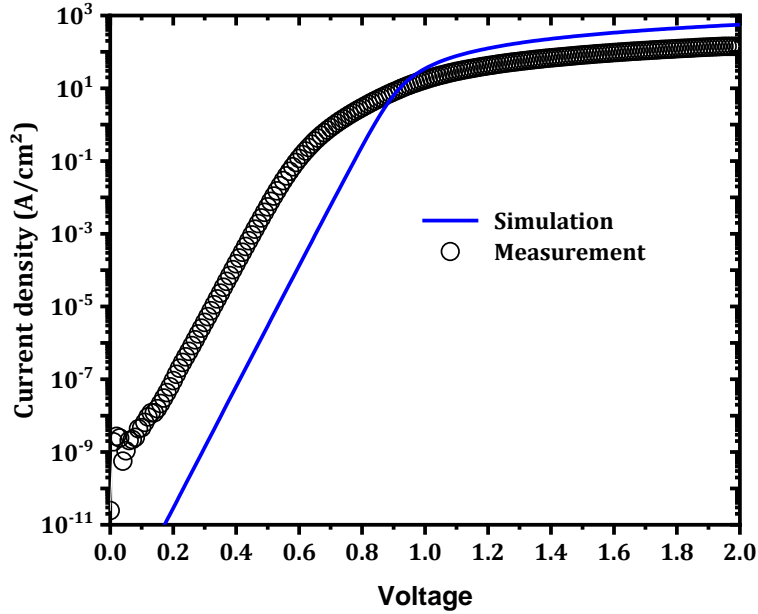


**Figure 5. 26 SBD simulated J-V characteristics and comparison with measurement.**

### 5.3.1.1. Effect of Ni workfunction

The effect of Ni workfunction was studied as presented in **Figure 5.27**. When the workfunction is increased from 4.8 to 5.5 eV, the current decreases. This decrease is related to the Schottky barrier height ($\phi_B$) increasing according to equation [78]:

$$\phi_B = \phi_{Ni} - \chi_{Ga_2O_3} \tag{5.19}$$

here $\phi_{Ni}$ and $\chi_{Ga_2O_3}$ are Nickel workfunction and β-$Ga_2O_3$ electron affinity respectively. An agreement between simulation and measurement results was observed at low voltage for $\phi_{Ni}$=5 eV. But for high voltage the agreement was not achieved. Hence other possible causes (Ni/β-$Ga_2O_3$ interface traps concentrations and β-$Ga_2O_3$ surface electron affinity) are investigated.
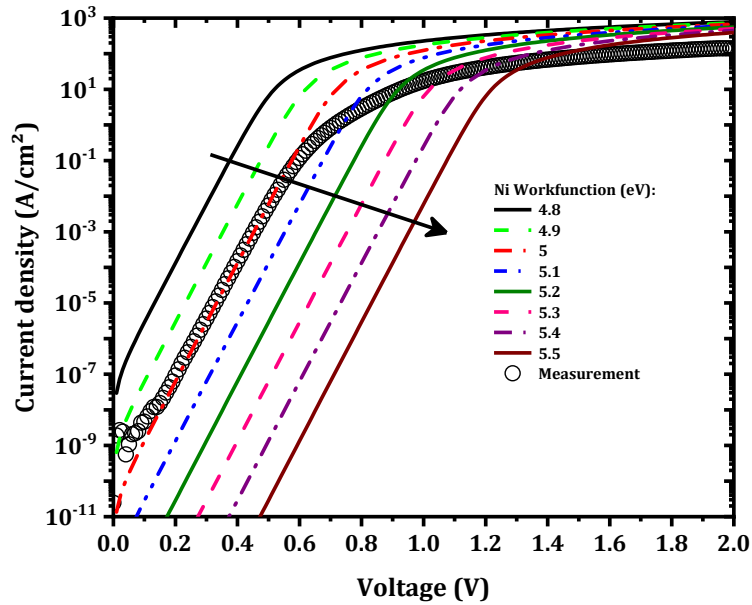
**Figure 5. 27 Simulated J-V characteristics for different Nickel work function and comparison with measurement in a semi-log scale. The insert is the linear scale.**

### 5.3.1.2. Effect of surface traps

The concentration of the $E_2$ ($E_c - 0.75$), $E_2^*$ ($E_c - 0.72$) and $E_3$ ($E_c - 1.05$) traps at the Ni/β-$Ga_2O_3$ interface effect on the thermionic current was studied. The choice of these traps is due to the fact that they were the most dominants in most samples[3]. The effect of these traps is shown in **Figure 5.28 (a),(b)** and **(c)** for $E_2$, $E_2^*$ and $E_3$ respectively. First with the traps concentrations increase the thermionic current decreased. But the disagreement between the simulation and measurement was still apparent at high voltages. The extracted interfacial traps densities were $8 \times 10^{15} cm^{-3}$ for each trap ($E_c - 0.75, E_c - 0.72$ and $E_c - 1.05$).
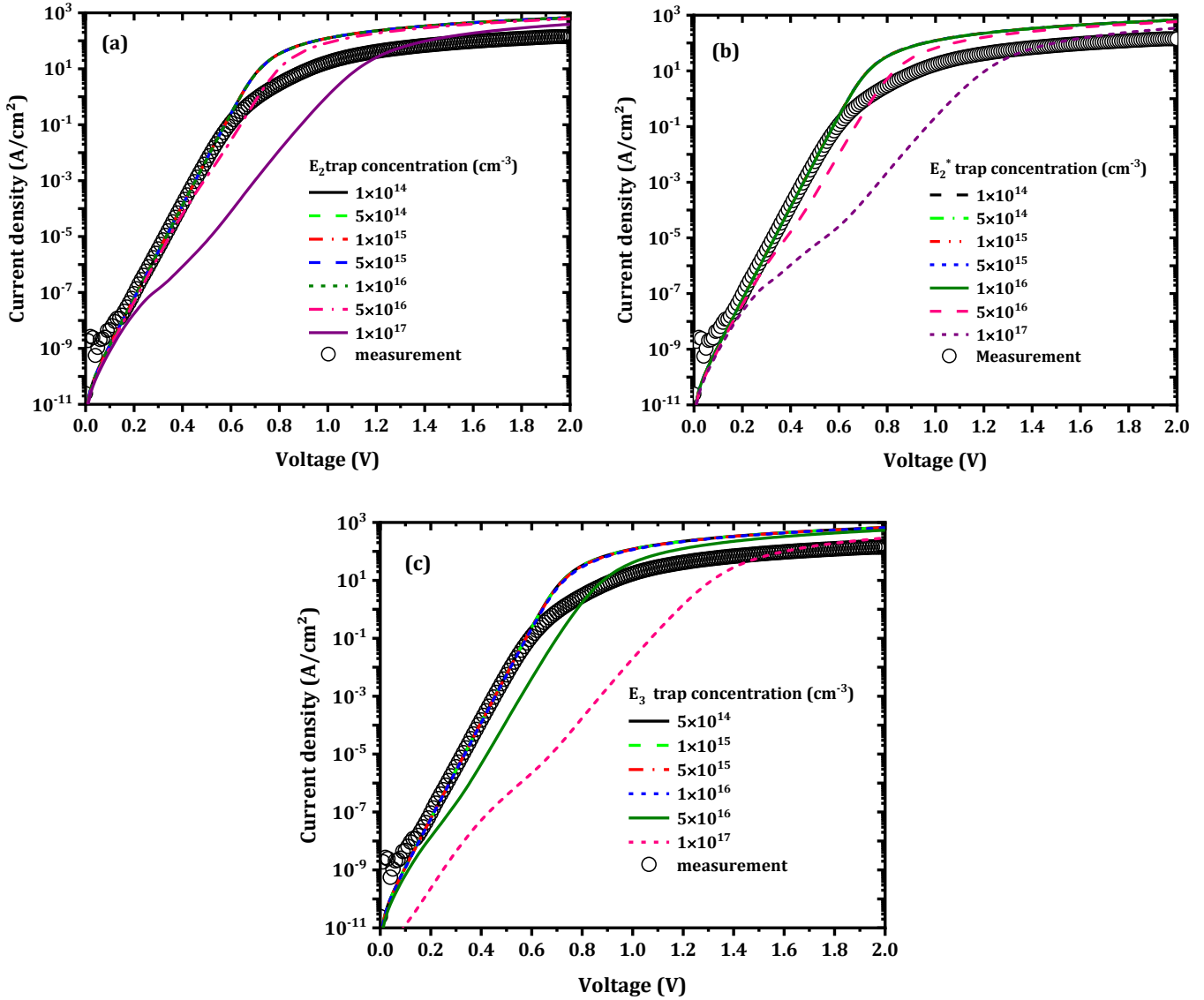
**Figure 5. 28 Effect of the traps density on the SBDs: (a) $E_c - 0.75\ eV$, (b) $E_c - 0.72\ eV$ and (c) $E_c - 1.05\ eV$ levels.**

### 5.3.1.3. Effect of surface electron affinity

Now, the surface electron affinity of Si-doped $\beta$-$Ga_2O_3$ was studied with the consideration of $8 \times 10^{15}\ cm^{-3}$ concentration for each trap. When the elecctron affinity decreased, the most affected region was the series resistance region of the J-V characteristics as **Figure 5.29** shows. This result is interpreted by the increase in the serie resistance with the surface electron affinity decrease.
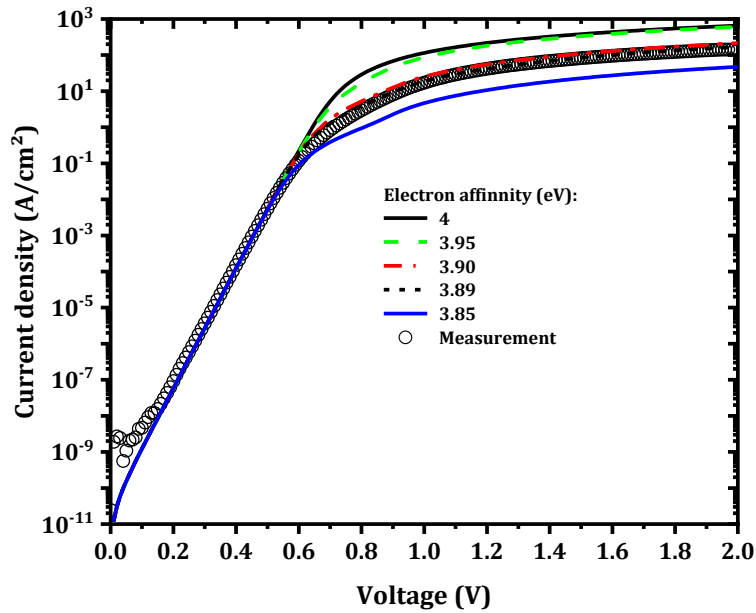
**Figure 5. 29 Simulated J-V characteristics for different Si-doped β-Ga₂O₃ surface electron affinity and comparison with measurement.**

For $\chi_{S,Ga_2O_3}$ = 3.89 eV a good agrement between simulation and measurement was obtained as **Figure 5.30** schows. The deviation between the simulation and measurement at low voltage (<0.1 V)is related to the low current density measurement which is outside the measurement domain of the analyzer. The extracted SBD paramaters from simulation and measurement are presented in **Table 5.3**.

**Table 5. 3 Outputs paramaters of Ni/β-Ga₂O₃ SBD for simulation and measurement.**

|  | n | $\phi_B$(eV) | $R_s$ (mΩ.cm²) | $R_{on}$ (mΩ.cm²) | $J_s$ (A/cm²) |
|---|---|---|---|---|---|
| **Measurement** | 1.07 | 1.30 | 67.8 | 7.19 | $1.89 \times 10^{-9}$ |
| **Simulation** | 1.06 | 1.32 | 60.3 | 7.47 | $1.26 \times 10^{-11}$ |
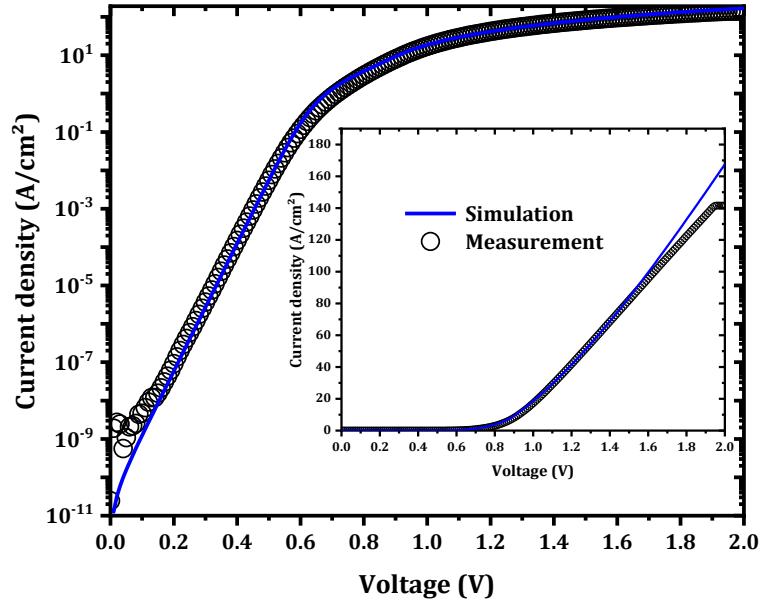
**Figure 5. 30 Best comparison between simulation and experimental results at room temperature for SBD deposited by E-beam evaporation.**

### 5.3.2. Effect of insertion of graphene layer

The effect of the insertion of a graphene monolayer between the Ni contact and the drift layer of the previous SBD (EBE SBD) is studied and the proposed structure is presented in **Figure 5.31**. This monolayer is able to form a low Schottky barrier contact with the n-type $\beta$-$Ga_2O_3$[120].
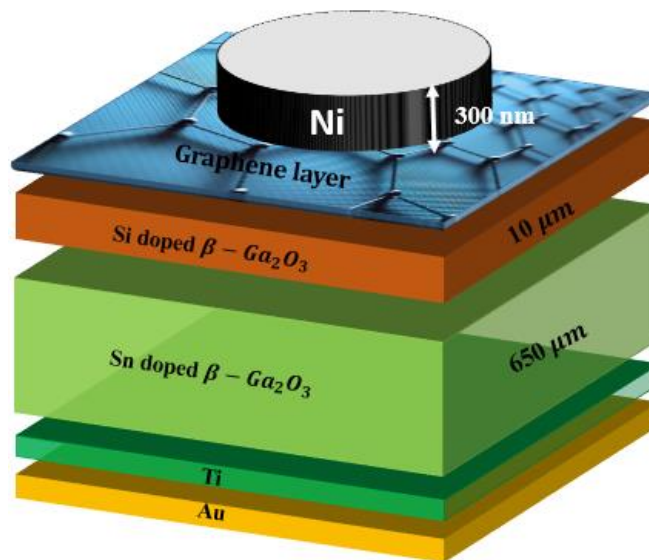
**Figure 5. 31 A schematic view of the structure when a graphene layer is inserted between Ni and Si-doped β-Ga₂O₃.**

As shown in **Figure 5.32**, a strong effect on the forward characteristics and a reduction of the Schottky barrier height from 1.32 to 0.43 eV were obtained, as well as a decrease in the series resistance ($R_s$) from 60.3 to 2.90 mΩ. cm². These variations agree with those obtained by Yuan et al.[120] for β-Ga₂O₃, GaN [121,122], SiC [123], and Si [124]. However, an increase in the saturation current from $1.26 \times 10^{-11}$ to $8.3 \times 10^{-7} (A/cm^2)$ was observed.
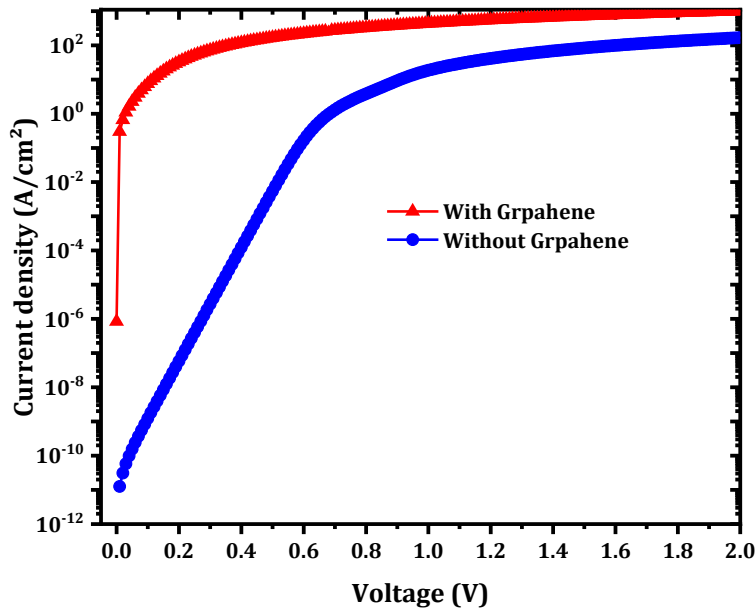


**Figure 5. 32 Effect of insertion a graphene layer on forward current.**

This decrease in $\phi_B$ and $R_s$ along with an increase in the saturation current can be explained by an increase in the tunneling rate in the SBD surface as presented in **Figure 5.33**.
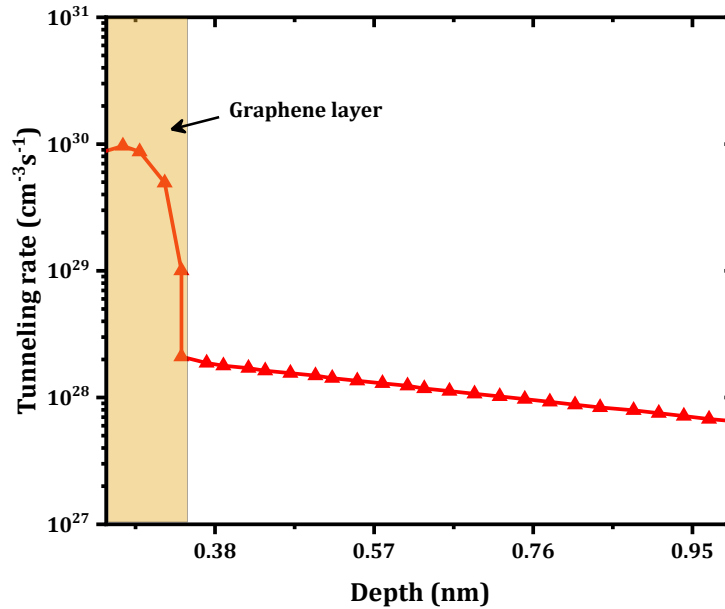
**Figure 5. 33 Tunneling rate variation when a graphene monolayer was inserted under 2 V of forward voltage.**

### 5.3.2.1. Effect of graphene bandgap

We have demonstrated that the graphene monolayer enhanced the outputs of the SBD by increasing the tunneling rate. We have now to take into account the fact that graphene has a tunable bandgap. Indeed, Takahashi *et al*.[125] found that the bandgap gradually increases with oxygen adsorption to as high as 0.45 eV at 2000 L oxygen exposure. Also by atomic and molecular doping control, such as simultaneous insertion of holes and electrons in hetero sites, one can increase the bandgap [126]. Based on this fact, the effect of graphene bandgap was investigated and when it is increased from 0 to 0.45 eV, the forward current is affected as shown in **Figure 5.34**.
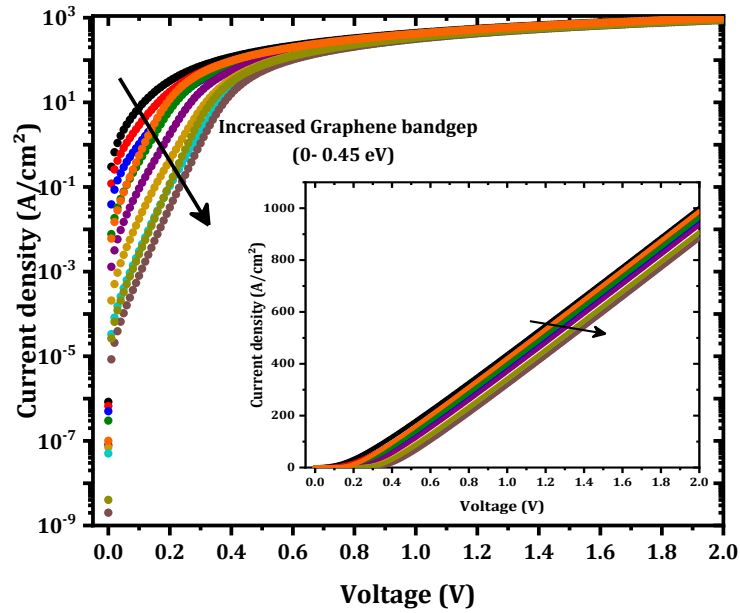
**Figure 5. 34 Effect of graphene bandgap on forward current.**

As the graphene bandgap was increased, the Schottky barrier height ($\phi_B$) increased from 0.43 eV to 0.69 eV as presented in **Figure 5.35**. This result can be interpreted by a decrease in the tunneling rate, as shown in **Figure 5.36**. This decrease in tunneling rate is related to the increase of the potential energy distribution of the Schottky barrier diode**.** The obtained values demonstrated the possibility of tuning the Schottky barrier height of Ni/ β-$Ga_2O_3$ Schottky diode, through the control of the tunneling rate in the graphene layer.
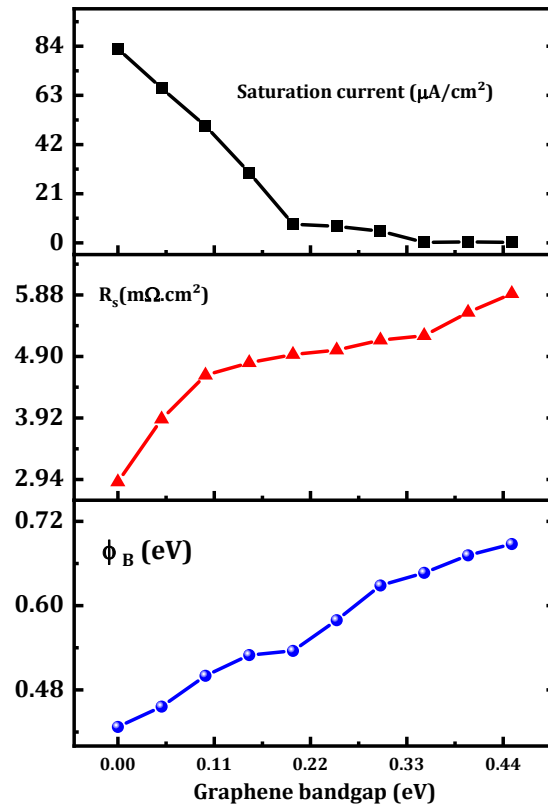
**Figure 5. 35 SBD outputs parameters variation with graphene bandgap (saturation current, serie resistance and Schottky barrier height).**

As shown in **Figure 5.35**, the series resistance increased from 2.90 to 5.90 m$\Omega$.cm$^2$, when the bandgap increased. This increase is related to the tunneling rate decrease and an increase in the extracted free electrons. In addition to the increase in R$_s$ and $\phi_B$ , the saturation current deceased as presented in **Figures 5.34** and **5.35**.
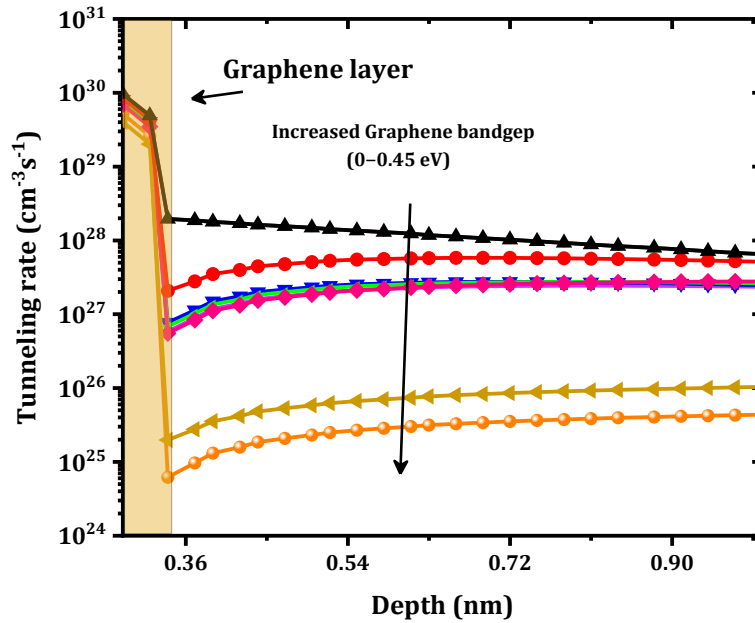
**Figure 5. 36 Tunneling rate variation with graphene bandgap.**

### 5.3.2.2. Effect of graphene workfunction

Now, we investigate the effect of another parameter that can play an important role in controlling the Schottky barrier height, which is the work function. A zero bandgap was considered for this study. When graphene workfunction increased from 4 to 4.8 eV, the forward current was affected (**Figure 5.37**) and $\phi_B$ increased from 0.320 eV to 0.545 eV as presented in **Figure 5.38**. The increase in Schottky barrier height is interpreted according to Schottky-Mott role ($\phi_B = W_{\text{graphene}} - \chi_{Ga_2O_3}$[124]) and due to the decrease in tunneling through graphene. Furthermore, a decrease in the saturation current was obtained with the increase of the workfunction. Also, $R_s$ increased from 0.89 to 3.9 mΩ.cm² with increasing the work function. This is related to the decrease in the tunneling rate in the graphene layer.
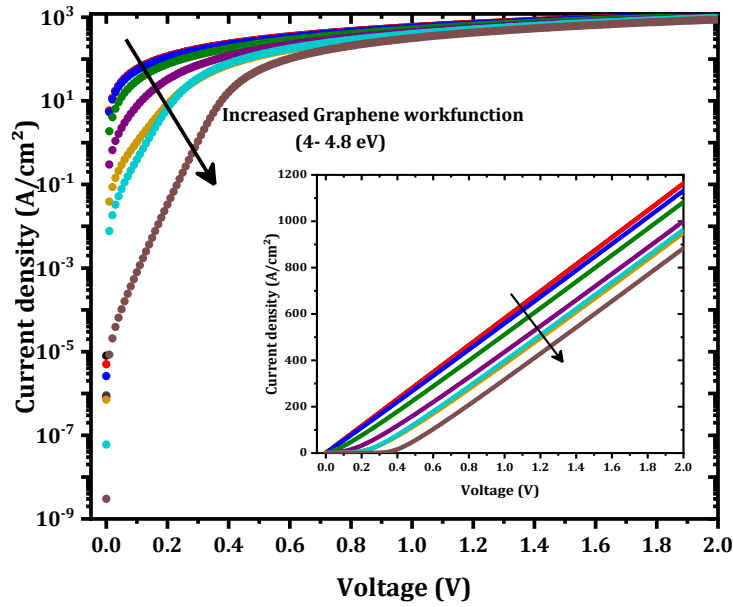
**Figure 5. 37 Effect of graphene workfunction on forward current.**

Also, $R_s$ increased from 0.89 to 3.9 m$\Omega$.cm$^2$ with increasing work function. This is related to the decrease in the tunneling rate in the graphene layer. We observed that the SBD with zero bandgap and low workfunction behaves as an Ohmic contact as the inset of **Figure 5.37** shows, because the forward current has a linear variation with forward voltage. It is therefore concluded that, the graphene layer with lower workfunction transits from a Schottky contact to an Ohmic contact, this result agree with that obtained by Yuan et al[120].
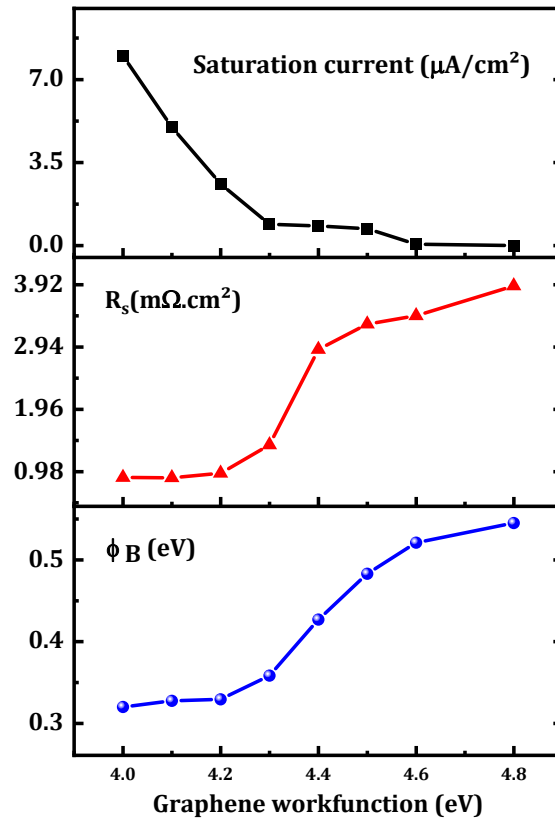
**Figure 5. 38 SBD outputs parameters variation with graphene workfunction (saturation current, serie resistance and Schottky barrier height).**

## 5.4. Summary

In summary, two Ni/β-Ga$_2$O$_3$ Schottky barrier diodes were investigated in this thesis. The difference between the two SBDs is the Schottky barrier metal method deposition; one is grown by CMFS while the second is by EBE. The investigation is carried out using Silvaco-Atlas and the modelling is compared to measurements.

For the first, an interfacial layer based on $(Ni_xGa_{1-x})_2O_3$ compound and traps related to plasma and Ar bombardment were considered for modeling the effect of Ni atoms diffusion in the surface of β-Ga$_2$O$_3$ when Ni deposited using CMFS at high and low temperature. Then, in addition to the proposed model with the consideration of Ni workfunction effect and band-to-band tunneling and other models in reverse bias a good agreement between simulation and measurement was obtained in forward and reverse domains. Then, optimizations based in insertion of undoped layer and edge termination layer a high performance SBD was obtained.

# Chapter 5: Results and discussion

For the second, SBD by considering the effects of Ni work function, interfacial traps concentrations and surface electron affinity a good agreement between simulation and measurement was obtained. The effect of insertion of a graphene monolayer in Ni/β-Ga$_2$O$_3$ interface proposed for controlling the SBD outputs parameters.

# General conclusion

In conclusion, the experimental current-voltage characteristics of two Ni/β-Ga₂O₃ Schottky barrier diodes, one produced by a confined magnetic field based sputtering (CMFS) and the other by electron-beam evaporation (EBE) are thoroughly investigated by Atlas numerical simulation.

Firstly, a model was developed for the CFMS diode to account for Ni diffusion from the Schottky metal to β-Ga₂O₃. In this model, Ni combines with oxygen of Ga₂O₃ to form a new $(Ni_xGa_{1-x})_2O_3$ layer at the interface between Ni and β-Ga₂O₃. This new compound has different energy gap and affinity than those of β-Ga₂O₃. Furthermore, Ni diffusion compensates Ga vacancy related defects; hence, the newly formed layer is less defected. The obtained simulation results are in good agreement with measurement in forward and reverse bias. This good comparison demonstrates the validity and soundness of the proposed model. Then, temperature dependence SBD parameters are investigated. Firstly, Schottky barrier height ($\phi_B$) decreased from 1.37 eV to 1.08 eV with increased temperature from 300 K to 500 K and the obtained result interpreted by a Gaussian distribution of the Schottky barrier  $\phi_B$ in the interfacial layer in which, with increasing temperature electrons located at low energy in the Gaussian energy distribution were activated because of the effect of $(Ni_xGa_{1-x})_2O_3$ interfacial layer and traps related to plasma and Ar bombardment. In addition, the extracted ideality factor is almost constant at ≈1.08. This behavior was related to the increase in the series resistance, and the latter increase was interpreted by the increase of the Ni metal resistance as well as the interfacial layer resistance which is due to the increased recombination through defects created by plasma and Ar bombardment. The Serie resistance (Rs) increased with increasing temperature. This variation is related to the increase of interfacial layer and Ni resistances. Finally, threshold voltage (Vth) decreased with increasing temperature; this decrease is related to the decrease in $\phi_B$. At low temperature, an ideality factor of 6.04 was obtained from the total current. The high ideality factor value is related to the tunneling effect since  an ideality factor of about 1.04 was extracted from the thermionic current component only. Then, optimizations were proposed in order to increase the breakdown voltage and decrease the leakage current and the on-resistance (Ron). The first optimization was considered by the insertion of a β-Ga₂O₃ undoped layer with different thicknesses between Ni and Si-doped β-Ga₂O₃. The intrinsic layer thickness of 0.4 $\mu m$ improves Baliga's figure of merit (BFOM) to $9.48 \times 10^7 \; W/cm^2$ with breakdown voltage and ON resistance of 465 V, 2.28 $m\Omega.cm^2$, respectively. Then, the proposed edge termination design based on a TiO₂ insulator

plate with a dielectric constant of about 80 gives further significant improvements of breakdown voltage, BFOM and specific on-resistance. The optimal value for TiO₂ thickness is ≈1.8 μm with BFOM and R_on reached $1.09 \times 10^9 \ W/cm^2$ and $1.98 \ m\Omega.cm^2$ respectively.

Secondly, SBD deposited by EBE was studied and compared with measurement in forward current. A good comparison between simulation and measurement was obtained with the consideration of effect of Ni workfunction, interfacial traps concentrations and surface electron affinity. The extracted Ni workfunction, interfacial traps concentrations and surface electron affinity were 5 eV, $8 \times 10^{15} cm^{-3}$ for $E_c - 0.75$, $E_c - 0.72$ and $E_c - 1.05$ and 3.89 eV respectively. Finally, a study based on the insertion of graphene layer between Ni and Si-doped β-Ga₂O₃ was proposed. However, Graphene is affected by plasma and Ar bombardment, so CMFS may not be suitable for fabrication of the mentioned structure. Therefore the optimisation by inserting a grafphene layer is limited to the E-beam SBD. A graphene layer was inserted between Ni and Si-doped β-Ga₂O₃. A strong effect on the forward current and a reduction of the Schottky barrier height from 1.32 to 0.43 eV were obtained, as well as a decrease in the series resistance (R_s) from 60.3 to 2.90 mΩ.cm². However, an increase in the saturation current from $1.26 \times 10^{-11}$ to $8.3 \times 10^{-7}$ A/cm² after inserting the graphene layer was observed. Then, the fact that the graphene has a tunable bandgap and workfunction is taken into account and the possibility to control $\phi_B$ from 0.43 eV to 0.69 eV with increasing graphene bandgap from 0 eV to 0.45 eV was demonstrated. In addition, $\phi_B$ can be controlled from 0.320 eV to 0.545 eV by increasing workfunction from 4 to 4.8 eV. Furthermore, we noticed that, when the inserted graphene has zero bandgap and low workfunction, SBD behaves as an Ohmic contact, because of the very low $\phi_B$ and R_s.

# References

[1]     H. Kim, S. Kyoung, T. Kang, J.Y. Kwon, K.H. Kim, Y.S. Rim, Effective surface diffusion of nickel on single crystal β-Ga$_2$O$_3$ for Schottky barrier modulation and high thermal stability, J. Mater. Chem. C. 7 (2019) 10953–10960. https://doi.org/10.1039/c9tc02922b.

[2]     S.J. Pearton, F. Ren, M. Tadjer, J. Kim, Perspective: Ga$_2$O$_3$ for ultra-high power rectifiers and MOSFETS, J. Appl. Phys. 124 (2018). https://doi.org/10.1063/1.5062841.

[3]     Z. Galazka, β-Ga$_2$O$_3$ for wide-bandgap electronics and optoelectronics, Semicond. Sci. Technol. 33 (2018) 113001. https://doi.org/10.1088/1361-6641/aadf78.

[4]     A.Y. Polyakov, I.-H. Lee, N.B. Smirnov, E.B. Yakimov, I. V. Shchemerov, A. V. Chernykh, A.I. Kochkova, A.A. Vasilev, P.H. Carey, F. Ren, D.J. Smith, S.J. Pearton, Defects at the surface of β-Ga$_2$O$_3$ produced by Ar plasma exposure, APL Mater. 7 (2019) 061102. https://doi.org/10.1063/1.5109025.

[5]     H. Xue, Q. He, G. Jian, S. Long, T. Pang, M. Liu, An Overview of the Ultrawide Bandgap Ga$_2$O$_3$ Semiconductor-Based Schottky Barrier Diode for Power Electronics Application, Nanoscale Res. Lett. 13 (2018) 290. https://doi.org/10.1186/s11671-018-2712-1.

[6]     A. Kyrtsos, M. Matsubara, E. Bellotti, On the feasibility of p-type Ga$_2$O$_3$, Appl. Phys. Lett. 112 (2018) 032108. https://doi.org/10.1063/1.5009423.

[7]     E. Chikoidze, C. Sartel, H. Mohamed, I. Madaci, T. Tchelidze, M. Modreanu, P. Vales-Castro, C. Rubio, C. Arnold, V. Sallet, Y. Dumont, A. Perez-Tomas, Enhancing the intrinsic p-type conductivity of the ultra-wide bandgap Ga$_2$O$_3$ semiconductor, J. Mater. Chem. C. 7 (2019) 10231–10239. https://doi.org/10.1039/C9TC02910A.

[8]     G. Jian, Q. He, W. Mu, B. Fu, H. Dong, Y. Qin, Y. Zhang, H. Xue, S. Long, Z. Jia, H. Lv, Q. Liu, X. Tao, M. Liu, Characterization of the inhomogeneous barrier distribution in a Pt/(100) β-Ga$_2$O$_3$ Schottky diode via its temperature-dependent electrical properties, AIP Adv. 8 (2018) 015316. https://doi.org/10.1063/1.5007197.

[9]     S.R. Thomas, G. Adamopoulos, Y.-H. Lin, H. Faber, L. Sygellou, E. Stratakis, N. Pliatsikas, P.A. Patsalas, T.D. Anthopoulos, High electron mobility thin-film transistors based on Ga$_2$O$_3$ grown by atmospheric ultrasonic spray pyrolysis at low temperatures, Appl. Phys. Lett. 105 (2014) 092105. https://doi.org/10.1063/1.4894643.

[10]    A. Grillo, J. Barrat, Z. Galazka, M. Passacantando, F. Giubileo, L. Iemmo, G. Luongo, F. Urban, C.

Dubourdieu, A. Di Bartolomeo, High field-emission current density from β-Ga$_2$O$_3$ nanopillars, Appl. Phys. Lett. 114 (2019) 193101. https://doi.org/10.1063/1.5096596.

[11]  E. Farzana, Z. Zhang, P.K. Paul, A.R. Arehart, S.A. Ringel, Influence of metal choice on (010) β-Ga$_2$O$_3$ Schottky diode properties, Appl. Phys. Lett. 110 (2017) 202102. https://doi.org/10.1063/1.4983610.

[12]  Y. Gao, A. Li, Q. Feng, Z. Hu, Z. Feng, K. Zhang, X. Lu, C. Zhang, H. Zhou, W. Mu, Z. Jia, J. Zhang, Y. Hao, High-Voltage β-Ga$_2$O$_3$ Schottky Diode with Argon-Implanted Edge Termination, Nanoscale Res. Lett. 14 (2019) 8. https://doi.org/10.1186/s11671-018-2849-y.

[13]  Q. He, W. Mu, H. Dong, S. Long, Z. Jia, H. Lv, Q. Liu, M. Tang, X. Tao, M. Liu, Schottky barrier diode based on β-Ga$_2$O$_3$ (100) single crystal substrate and its temperature-dependent electrical characteristics, Appl. Phys. Lett. 110 (2017) 093503. https://doi.org/10.1063/1.4977766.

[14]  J. Yang, S. Ahn, F. Ren, R. Khanna, K. Bevlin, D. Geerpuram, S.J. Pearton, A. Kuramata, Inductively coupled plasma etch damage in (-201) Ga$_2$O$_3$ Schottky diodes, Appl. Phys. Lett. 110 (2017) 1–5. https://doi.org/10.1063/1.4979592.

[15]  R. Roy, V.G. Hill, E.F. Osborn, Polymorphism of Ga$_2$O$_3$ and the System Ga$_2$O$_3$ -H$_2$O, J. Am. Chem. Soc. 74 (1952) 719–722. https://doi.org/10.1021/ja01123a039.

[16]  M. Zinkevich, F. Aldinger, Thermodynamic Assessment of the Gallium-Oxygen System, J. Am. Ceram. Soc. 87 (2004) 683–691. https://doi.org/10.1111/j.1551-2916.2004.00683.x.

[17]  S. Penner, C. Zhuo, R. Thalinger, M. Grünbacher, C. Hejny, S. Vanicek, M. Noisternig, Physico-chemical properties of unusual Ga$_2$O$_3$ polymorphs, Monatshefte Für Chemie - Chem. Mon. 147 (2016) 289–300. https://doi.org/10.1007/s00706-015-1628-z.

[18]  H.Y. Playford, A.C. Hannon, E.R. Barney, R.I. Walton, Structures of Uncharacterised Polymorphs of Gallium Oxide from Total Neutron Diffraction, Chem. – A Eur. J. 19 (2013) 2803–2813. https://doi.org/10.1002/chem.201203359.

[19]  S. Yoshioka, H. Hayashi, A. Kuwabara, F. Oba, K. Matsunaga, I. Tanaka, Structures and energetics of Ga$_2$O$_3$ polymorphs, J. Phys. Condens. Matter. 19 (2007) 346211. https://doi.org/10.1088/0953-8984/19/34/346211.

[20]  M. Bosi, P. Mazzolini, L. Seravalli, R. Fornari, Ga$_2$O$_3$ polymorphs: tailoring the epitaxial growth conditions, J. Mater. Chem. C. (2020). https://doi.org/10.1039/D0TC02743J.

[21]  M.R. Delgado, C.O. Areán, Infrared Spectroscopic Studies on the Surface Chemistry of High-Surface-Area Gallia Polymorphs, Zeitschrift Für Anorg. Und Allg. Chemie. 631 (2005) 2115–

2120. https://doi.org/10.1002/zaac.200570026.

[22]   I. Cora, F. Mezzadri, F. Boschi, M. Bosi, M. Čaplovičová, G. Calestani, I. Dódony, B. Pécz, R. Fornari, The real structure of ε-$Ga_2O_3$ and its relation to κ-phase, CrystEngComm. 19 (2017) 1509–1516. https://doi.org/10.1039/C7CE00123A.

[23]   I. Cora, Z. Fogarassy, R. Fornari, M. Bosi, A. Rečnik, B. Pécz, In situ TEM study of κ→β and κ→γ phase transformations in $Ga_2O_3$, Acta Mater. 183 (2020) 216–227. https://doi.org/10.1016/j.actamat.2019.11.019.

[24]   M. Marezio, J.P. Remeika, Bond Lengths in the α-$Ga_2O_3$ Structure and the High-Pressure Phase of $Ga_{2-x}Fe_xO_3$, J. Chem. Phys. 46 (1967) 1862–1865. https://doi.org/10.1063/1.1840945.

[25]   K. Pohl, Hydrothermale Bildung von γ-$Ga_2O_3$, Naturwissenschaften. 55 (1968) 82. https://doi.org/10.1007/BF00599490.

[26]   D. Shinohara, S. Fujita, Heteroepitaxy of Corundum-Structured α-$Ga_2O_3$Thin Films on α-$Al_2O_3$ Substrates by Ultrasonic Mist Chemical Vapor Deposition, Jpn. J. Appl. Phys. 47 (2008) 7311–7313. https://doi.org/10.1143/jjap.47.7311.

[27]   Y. Oshima, E.G. Víllora, Y. Matsushita, S. Yamamoto, K. Shimamura, Epitaxial growth of phase-pure ε- $Ga_2O_3$ by halide vapor phase epitaxy, J. Appl. Phys. 118 (2015) 085301. https://doi.org/10.1063/1.4929417.

[28]   C. Wu, D.Y. Guo, L.Y. Zhang, P.G. Li, F.B. Zhang, C.K. Tan, S.L. Wang, A.P. Liu, F.M. Wu, W.H. Tang, Systematic investigation of the growth kinetics of β-$Ga_2O_3$ epilayer by plasma enhanced chemical vapor deposition, Appl. Phys. Lett. 116 (2020) 072102. https://doi.org/10.1063/1.5142196.

[29]   S. Nakagomi, S. Kubo, Y. Kokubun, The orientational relationship between monoclinic β-$Ga_2O_3$ and cubic NiO, J. Cryst. Growth. 445 (2016) 73–77. https://doi.org/10.1016/j.jcrysgro.2016.04.023.

[30]   T. Oshima, K. Matsuyama, K. Yoshimatsu, A. Ohtomo, Conducting Si-doped γ-$Ga_2O_3$ epitaxial films grown by pulsed-laser deposition, J. Cryst. Growth. 421 (2015) 23–26. https://doi.org/https://doi.org/10.1016/j.jcrysgro.2015.04.011.

[31]   X. Zhang, H. Huang, Y. Zhang, D. Liu, N. Tong, J. Lin, L. Chen, Z. Zhang, X. Wang, Phase Transition of Two-Dimensional β-$Ga_2O_3$ Nanosheets from Ultrathin γ-$Ga_2O_3$ Nanosheets and Their Photocatalytic Hydrogen Evolution Activities, ACS Omega. 3 (2018) 14469–14476. https://doi.org/10.1021/acsomega.8b01964.

[32]  X. Wang, Q. Xu, F. Fan, X. Wang, M. Li, Z. Feng, C. Li, Study of the Phase Transformation of Single Particles of $Ga_2O_3$ by UV-Raman Spectroscopy and High-Resolution TEM, Chem. - An Asian J. 8 (2013) 2189–2195. https://doi.org/10.1002/asia.201300433.

[33]  Y. Oshima, E.G. Víllora, K. Shimamura, Quasi-heteroepitaxial growth of β-$Ga_2O_3$ on off-angled sapphire (0001) substrates by halide vapor phase epitaxy, J. Cryst. Growth. 410 (2015) 53–58. https://doi.org/https://doi.org/10.1016/j.jcrysgro.2014.10.038.

[34]  Y. Yao, S. Okur, L.A.M. Lyle, G.S. Tompa, T. Salagaj, N. Sbrockey, R.F. Davis, L.M. Porter, Growth and characterization of α-, β-, and ϵ-phases of $Ga_2O_3$ using MOCVD and HVPE techniques, Mater. Res. Lett. 6 (2018) 268–275. https://doi.org/10.1080/21663831.2018.1443978.

[35]  K. Nomura, K. Goto, R. Togashi, H. Murakami, Y. Kumagai, A. Kuramata, S. Yamakoshi, A. Koukitu, Thermodynamic study of β-Ga2O3 growth by halide vapor phase epitaxy, J. Cryst. Growth. 405 (2014) 19–22. https://doi.org/https://doi.org/10.1016/j.jcrysgro.2014.06.051.

[36]  H. Murakami, K. Nomura, K. Goto, K. Sasaki, K. Kawara, Q.T. Thieu, R. Togashi, Y. Kumagai, M. Higashiwaki, A. Kuramata, S. Yamakoshi, B. Monemar, A. Koukitu, Homoepitaxial growth of β-$Ga_2O_3$ layers by halide vapor phase epitaxy, Appl. Phys. Express. 8 (2014) 15503. https://doi.org/10.7567/apex.8.015503.

[37]  K. Konishi, K. Goto, R. Togashi, H. Murakami, M. Higashiwaki, A. Kuramata, S. Yamakoshi, B. Monemar, Y. Kumagai, Comparison of $O_2$ and $H_2O$ as oxygen source for homoepitaxial growth of β-$Ga_2O_3$ layers by halide vapor phase epitaxy, J. Cryst. Growth. 492 (2018) 39–44. https://doi.org/https://doi.org/10.1016/j.jcrysgro.2018.04.009.

[38]  Q.T. Thieu, D. Wakimoto, Y. Koishikawa, K. Sasaki, K. Goto, K. Konishi, H. Murakami, A. Kuramata, Y. Kumagai, S. Yamakoshi, Preparation of 2-in.-diameter (001) β-$Ga_2O_3$ homoepitaxial wafers by halide vapor phase epitaxy, Jpn. J. Appl. Phys. 56 (2017) 110310. https://doi.org/10.7567/JJAP.56.110310.

[39]  Y. Kokubun, K. Miura, F. Endo, S. Nakagomi, Sol-gel prepared β-$Ga_2O_3$ thin films for ultraviolet photodetectors, Appl. Phys. Lett. 90 (2007) 31912. https://doi.org/10.1063/1.2432946.

[40]  Y. OHYA, J. OKANO, Y. KASUYA, T. BAN, Fabrication of $Ga_2O_3$ thin films by aqueous solution deposition, J. Ceram. Soc. Japan. 117 (2009) 973–977. https://doi.org/10.2109/jcersj2.117.973.

[41]  H.W. Xue, Q.M. He, G.Z. Jian, S.B. Long, T. Pang, M. Liu, An Overview of the Ultrawide Bandgap $Ga_2O_3$ Semiconductor-Based Schottky Barrier Diode for Power Electronics Application,

Nanoscale Res. Lett. 13 (2018) 1–13. https://doi.org/10.1186/s11671-018-2712-1.

[42]  Z. Galazka, β-Ga$_2$O$_3$ for wide-bandgap electronics and optoelectronics, Semicond. Sci. Technol. 33 (2018) 113001. https://doi.org/10.1088/1361-6641/aadf78.

[43]  S. Geller, Crystal Structure of β-Ga$_2$O$_3$, J. Chem. Phys. 33 (1960) 676–684. https://doi.org/10.1063/1.1731237.

[44]  C. Cocchi, H. Zschiesche, D. Nabok, A. Mogilatenko, M. Albrecht, Z. Galazka, H. Kirmse, C. Draxl, C.T. Koch, Atomic signatures of local environment from core-level spectroscopy in β-Ga$_2$O$_3$, Phys. Rev. B. 94 (2016) 075147. https://doi.org/10.1103/PhysRevB.94.075147.

[45]  M. Mohamed, C. Janowitz, I. Unger, R. Manzke, Z. Galazka, R. Uecker, R. Fornari, J.R. Weber, J.B. Varley, C.G. Van de Walle, The electronic structure of β-Ga$_2$O$_3$, Appl. Phys. Lett. 97 (2010) 211903. https://doi.org/10.1063/1.3521255.

[46]  K. Yamaguchi, First principles study on electronic structure of β-Ga$_2$O$_3$, Solid State Commun. 131 (2004) 739–744. https://doi.org/https://doi.org/10.1016/j.ssc.2004.07.030.

[47]  H. He, R. Orlando, M.A. Blanco, R. Pandey, E. Amzallag, I. Baraille, M. Rérat, First-principles study of the structural, electronic, and optical properties of β-Ga$_2$O$_3$ in its monoclinic and hexagonal phases, Phys. Rev. B. 74 (2006) 195123. https://doi.org/10.1103/PhysRevB.74.195123.

[48]  J. Furthmüller, F. Bechstedt, Quasiparticle bands and spectra of β-Ga$_2$O$_3$ polymorphs, Phys. Rev. B. 93 (2016) 115204. https://doi.org/10.1103/PhysRevB.93.115204.

[49]  J.B. Varley, J.R. Weber, A. Janotti, C.G. Van de Walle, Oxygen vacancies and donor impurities in β-Ga$_2$O$_3$, Appl. Phys. Lett. 97 (2010) 142106. https://doi.org/10.1063/1.3499306.

[50]  J.B. Varley, H. Peelaers, A. Janotti, C.G. Van de Walle, Hydrogenated cation vacancies in semiconducting oxides, J. Phys. Condens. Matter. 23 (2011) 334212. https://doi.org/10.1088/0953-8984/23/33/334212.

[51]  J.B. Varley, A. Schleife, Bethe–Salpeter calculation of optical-absorption spectra of In$_2$O$_3$ and Ga$_2$O$_3$, Semicond. Sci. Technol. 30 (2015) 24010. https://doi.org/10.1088/0268-1242/30/2/024010.

[52]  F. Zhang, H. Li, Y.-T. Cui, G.-L. Li, Q. Guo, Evolution of optical properties and band structure from amorphous to crystalline Ga$_2$O$_3$ films, AIP Adv. 8 (2018) 45112. https://doi.org/10.1063/1.5021867.

[53]  X. Ma, Y. Zhang, L. Dong, R. Jia, First-principles calculations of electronic and optical properties of aluminum-doped β-Ga$_2$O$_3$ with intrinsic defects, Results Phys. 7 (2017) 1582–1589.

https://doi.org/10.1016/j.rinp.2017.04.023.

[54] M.R. Lorenz, J.F. Woods, R.J. Gambino, Some electrical properties of the semiconductor β-Ga₂O₃, J. Phys. Chem. Solids. 28 (1967) 403–404. https://doi.org/10.1016/0022-3697(67)90305-8.

[55] N. Ueda, H. Hosono, R. Waseda, H. Kawazoe, Synthesis and control of conductivity of ultraviolet transmitting β-Ga₂O₃ single crystals, Appl. Phys. Lett. 70 (1997) 3561–3563. https://doi.org/10.1063/1.119233.

[56] Z. Galazka, K. Irmscher, R. Uecker, R. Bertram, M. Pietsch, A. Kwasniewski, M. Naumann, T. Schulz, R. Schewski, D. Klimm, M. Bickermann, On the bulk β-Ga₂O₃ single crystals grown by the Czochralski method, J. Cryst. Growth. 404 (2014) 184–191. https://doi.org/10.1016/j.jcrysgro.2014.07.021.

[57] E.G. Víllora, K. Shimamura, Y. Yoshikawa, T. Ujiie, K. Aoki, Electrical conductivity and carrier concentration control in β-Ga₂O₃ by Si doping, Appl. Phys. Lett. 92 (2008) 202120. https://doi.org/10.1063/1.2919728.

[58] R. Schewski, M. Baldini, K. Irmscher, A. Fiedler, T. Markurt, B. Neuschulz, T. Remmele, T. Schulz, G. Wagner, Z. Galazka, M. Albrecht, Evolution of planar defects during homoepitaxial growth of β-Ga₂O₃ layers on (100) substrates- A quantitative model, J. Appl. Phys. 120 (2016) 225308. https://doi.org/10.1063/1.4971957.

[59] M.E. Ingebrigtsen, J.B. Varley, A.Y. Kuznetsov, B.G. Svensson, G. Alfieri, A. Mihaila, U. Badstübner, L. Vines, Iron and intrinsic deep level states in Ga₂O₃, Appl. Phys. Lett. 112 (2018) 042104. https://doi.org/10.1063/1.5020134.

[60] Y. Yao, R. Gangireddy, J. Kim, K.K. Das, R.F. Davis, L.M. Porter, Electrical behavior of β-Ga₂O₃ Schottky diodes with different Schottky metals , J. Vac. Sci. Technol. B, Nanotechnol. Microelectron. Mater. Process. Meas. Phenom. 35 (2017) 03D113. https://doi.org/10.1116/1.4980042.

[61] S. Ohira, N. Arai, Wet chemical etching behavior of β-Ga₂O₃ single crystal, Phys. Status Solidi. 5 (2008) 3116–3118. https://doi.org/10.1002/pssc.200779223.

[62] J. Du, Z. Li, D. Liu, Z. Bai, Y. Liu, Q. Yu, Design of high breakdown voltage vertical GaN p-n diodes with high-K/low-K compound dielectric structure for power electronics applications, Superlattices Microstruct. 111 (2017) 302–309. https://doi.org/10.1016/j.spmi.2017.06.045.

[63] J. Yang, F. Ren, R. Khanna, K. Bevlin, D. Geerpuram, L.-C. Tung, J. Lin, H. Jiang, J. Lee, E. Flitsiyan, L. Chernyak, S.J. Pearton, A. Kuramata, Annealing of dry etch damage in metallized and bare (-

201) Ga$_2$O$_3$, J. Vac. Sci. Technol. B. 35 (2017) 51201. https://doi.org/10.1116/1.4986300.

[64] M.A. Scarpulla, K.G. Lynn, S. Krishnamoorthy, Schottky Barrier Height Engineering in β-Ga$_2$O$_3$ Using SiO 2 Interlayer Dielectric, 8 (2020). https://doi.org/10.1109/JEDS.2020.2974260.

[65] T. Harada, A. Tsukazaki, Control of Schottky barrier height in metal/β-Ga$_2$O$_3$ junctions by insertion of PdCoO$_2$ layers, APL Mater. 8 (2020) 41109. https://doi.org/10.1063/1.5145117.

[66] W. Li, D. Saraswat, Y. Long, K. Nomoto, D. Jena, H.G. Xing, Near-ideal reverse leakage current and practical maximum electric field in β-Ga$_2$O$_3$ Schottky barrier diodes, Appl. Phys. Lett. 116 (2020) 192101. https://doi.org/10.1063/5.0007715.

[67] E.L. Murphy, R.H. Good, Thermionic Emission, Field Emission, and the Transition Region, Phys. Rev. 102 (1956) 1464–1473. https://doi.org/10.1103/PhysRev.102.1464.

[68] L. Zhou, X. Lu, L. Chen, X. Ouyang, B. Liu, J. Xu, H. Tang, Leakage Current by Poole–Frenkel Emission in Pt Schottky Contacts on ($\bar{2}$01) β-Ga$_2$O$_3$ Grown by Edge-Defined Film-Fed Growth, ECS J. Solid State Sci. Technol. 8 (2019) Q3054–Q3057. https://doi.org/10.1149/2.0111907jss.

[69] H. Fu, H. Chen, X. Huang, I. Baranowski, J. Montes, T.-H. Yang, Y. Zhao, A Comparative Study on the Electrical Properties of Vertical ($\bar{2}$01) and (010) β-Ga$_2$O$_3$ Schottky Barrier Diodes on EFG Single-Crystal Substrates, IEEE Trans. Electron Devices. 65 (2018) 3507–3513. https://doi.org/10.1109/TED.2018.2841904.

[70] Z. Hu, Q. Feng, Z. Feng, Y. Cai, Y. Shen, G. Yan, X. Lu, C. Zhang, H. Zhou, J. Zhang, Y. Hao, Experimental and Theoretical Studies of Mo/Au Schottky Contact on Mechanically Exfoliated β-Ga$_2$O$_3$ Thin Film, Nanoscale Res. Lett. 14 (2019) 2. https://doi.org/10.1186/s11671-018-2837-2.

[71] R. Lingaparthi, K. Sasaki, Q.T. Thieu, A. Takatsuka, F. Otsuka, S. Yamakoshi, A. Kuramata, Surface related tunneling leakage in β-Ga$_2$O$_3$ (001) vertical Schottky barrier diodes, Appl. Phys. Express. 12 (2019) 074008. https://doi.org/10.7567/1882-0786/ab2824.

[72] M. Ravinandan, P.K. Rao, V. Rajagopal Reddy, Analysis of the current–voltage characteristics of the Pd/Au Schottky structure on n-type GaN in a wide temperature range, Semicond. Sci. Technol. 24 (2009) 035004. https://doi.org/10.1088/0268-1242/24/3/035004.

[73] U. Parihar, J. Ray, C.J.P. Naresh, Influence of temperature on Al / p-CuInAlSe$_2$ thin-film Schottky diodes, Appl. Phys. A. 122 (2016) 1–7. https://doi.org/10.1007/s00339-016-0105-9.

[74] M. Garg, A. Kumar, S. Nagarajan, M. Sopanen, R. Singh, Investigation of significantly high barrier height in Cu/GaN Schottky diode, AIP Adv. 6 (2016). https://doi.org/10.1063/1.4939936.

[75] E. Arslan, Ş. Altındal, S. Özçelik, E. Ozbay, Tunneling current via dislocations in Schottky diodes on AlInN/AlN/GaN heterostructures, Semicond. Sci. Technol. 24 (2009) 075003. https://doi.org/10.1088/0268-1242/24/7/075003.

[76] P.R.S. Reddy, V. Janardhanam, K.H. Shim, V.R. Reddy, S.N. Lee, S.J. Park, C.J. Choi, Temperature-dependent Schottky barrier parameters of Ni/Au on n-type (001) β-Ga$_2$O$_3$ Schottky barrier diode, Vacuum. 171 (2020) 109012. https://doi.org/10.1016/j.vacuum.2019.109012.

[77] H. Sheoran, B.R. Tak, N. Manikanthababu, R. Singh, Temperature-Dependent Electrical Characteristics of Ni/Au Vertical Schottky Barrier Diodes on β-Ga$_2$O$_3$ Epilayers, ECS J. Solid State Sci. Technol. 9 (2020) 55004. https://doi.org/10.1149/2162-8777/ab96ad.

[78] S.M. Sze, K.K. Ng, Metal-Semiconductor Contacts, in: Phys. Semicond. Devices, John Wiley & Sons, Inc., Hoboken, NJ, USA, 2006: pp. 134–196. https://doi.org/10.1002/9780470068328.ch3.

[79] K. Goto, K. Sasaki, A. Koukitu, Y. Kumagai, H. Murakami, Method for growing β-Ga$_2$O$_3$ single crystal film and crystalline layered structure, US20210404086A1, 2021.

[80] J.H. Leach, K. Udwary, J. Rumsey, G. Dodson, H. Splawn, K.R. Evans, Halide vapor phase epitaxial growth of β-Ga$_2$O$_3$ and α-Ga$_2$O$_3$ films, APL Mater. 7 (2018) 22504. https://doi.org/10.1063/1.5055680.

[81] R.T. Tung, The physics and chemistry of the Schottky barrier height, Appl. Phys. Rev. 1 (2014) 11304. https://doi.org/10.1063/1.4858400.

[82] Donald A. Neamen, Semiconductor physics and devices: Basic principles, 4th ed., 2012. https://doi.org/10.1017/CBO9781107415324.004.

[83] A. Tataro, The role of interface states and series resistance on the I – V and C – V characteristics in Al / SnO$_2$ /p-Si Schottky diodes, 47 (2003) 1847–1854. https://doi.org/10.1016/S0038-1101(03)00182-5.

[84] J.R. Nicholls, S. Dimitrijev, P. Tanner, J. Han, The Role of Near-Interface Traps in Modulating the Barrier Height of SiC Schottky Diodes, IEEE Trans. Electron Devices. 66 (2019) 1675–1680. https://doi.org/10.1109/TED.2019.2896216.

[85] V.L. Rideout, C.R. Crowell, Effects of image force and tunneling on current transport in metal-semiconductor (Schottky barrier) contacts, Solid. State. Electron. 13 (1970) 993–1009. https://doi.org/https://doi.org/10.1016/0038-1101(70)90097-3.

[86] S.M. Sze, K.K. Ng, Physics of semiconductor devices, 3rd ed., John wiley & sons, Hoboken, NJ,

USA, 2006.

[87]  J.B. Roldán, F. Gámiz, J.A. López-Villanueva, J.E. Carceller, P. Cartujo, The dependence of the electron mobility on the longitudinal electric field in {MOSFETs}, Semicond. Sci. Technol. 12 (1997) 321–330. https://doi.org/10.1088/0268-1242/12/3/014.

[88]  S. Rafique, L. Han, S. Mou, H. Zhao, Temperature and doping concentration dependence of the energy band gap in $\beta$-$Ga_2O_3$ thin films grown on sapphire, Opt. Mater. Express. 7 (2017) 3561–3570. https://doi.org/10.1364/OME.7.003561.

[89]  S.C. Jain, D.J. Roulston, A simple expression for band gap narrowing (BGN) in heavily doped Si, Ge, GaAs and $Ge_xSi_{1-x}$ strained layers, Solid State Electron. 34 (1991) 453–465. https://doi.org/10.1016/0038-1101(91)90149-S.

[90]  J.-H. Choi, C.-H. Cho, H.-Y. Cha, Design consideration of high voltage $Ga_2O_3$ vertical Schottky barrier diode with field plate, Results Phys. 9 (2018) 1170–1171. https://doi.org/10.1016/j.rinp.2018.04.042.

[91]  M.K. Ieong, P.M. Solomon, S.E. Laux, H.S.P. Wong, D. Chidambarrao, Comparison of raised and Schottky source/drain MOSFETs using a novel tunneling contact model, Tech. Dig. - Int. Electron Devices Meet. (1998) 733–736. https://doi.org/10.1109/iedm.1998.746461.

[92]  K.-H. Kao, A.S. Verhulst, W.G. Vandenberghe, B. Soree, G. Groeseneken, K. De Meyer, Direct and Indirect Band-to-Band Tunneling in Germanium-Based TFETs, IEEE Trans. Electron Devices. 59 (2012) 292–301. https://doi.org/10.1109/TED.2011.2175228.

[93]  X. Huang, F. Liao, L. Li, X. Liang, Q. Liu, C. Zhang, X. Hu, 3.4 kV Breakdown Voltage $Ga_2O_3$ Trench Schottky Diode with Optimized Trench Corner Radius, ECS J. Solid State Sci. Technol. 9 (2020) 045012. https://doi.org/10.1149/2162-8777/ab8b4a.

[94]  A.J. Scholten, G.D.J. Smit, M. Durand, R. Van Langevelde, D.B.M. Klaassen, The physical background of JUNGAP2, IEEE Trans. Electron Devices. 53 (2006) 2098–2107. https://doi.org/10.1109/TED.2005.881004.

[95]  G.K. Wachutka, Rigorous Thermodynamic Treatment of Heat Generation and Conduction in Semiconductor Device Modeling, IEEE Trans. Comput. Des. Integr. Circuits Syst. 9 (1990) 1141–1149. https://doi.org/10.1109/43.62751.

[96]  Silvaco TCAD, ATLAS User ' s Manual, (2018).

[97]  Z. Wang, H. Gong, C. Meng, X. Yu, X. Sun, C. Zhang, X. Ji, F. Ren, S. Gu, Y. Zheng, R. Zhang, J. Ye, Majority and Minority Carrier Traps in NiO/$\beta$-$Ga_2O_3$ $p^+$-n Heterojunction Diode, IEEE Trans.

Electron Devices. 69 (2022) 981–987. https://doi.org/10.1109/TED.2022.3143491.

[98] M. Tachiki, T. Hosomi, T. Kobayashi, Room-Temperature Heteroepitaxial Growth of NiO Thin Films using Pulsed Laser Deposition, Jpn. J. Appl. Phys. 39 (2000) 1817–1820. https://doi.org/10.1143/jjap.39.1817.

[99] K.-C. Wang, P.-S. Shen, M.-H. Li, S. Chen, M.-W. Lin, P. Chen, T.-F. Guo, Low-Temperature Sputtered Nickel Oxide Compact Thin Film as Effective Electron Blocking Layer for Mesoscopic NiO/$CH_3NH_3PbI_3$ Perovskite Heterojunction Solar Cells, ACS Appl. Mater. Interfaces. 6 (2014) 11851–11858. https://doi.org/10.1021/am503610u.

[100] H. Peelaers, J.B. Varley, J.S. Speck, C.G. Van de Walle, Structural and electronic properties of $Ga_2O_3$ -$Al_2O_3$ alloys, Appl. Phys. Lett. 112 (2018) 242101. https://doi.org/10.1063/1.5036991.

[101] D.-H. Kwon, S.R. Lee, Y.S. Choi, S.-B. Son, K.H. Oh, K. Char, M. Kim, Observation of the $Ni_2O_3$ phase in a NiO thin-film resistive switching system, Phys. Status Solidi – Rapid Res. Lett. 11 (2017) 1700048. https://doi.org/10.1002/pssr.201700048.

[102] K. Jouini, A. Raouafi, W. Dridi, M. Daoudi, B. Mustapha, R. Chtourou, F. Hosni, Investigation of gamma-ray irradiation induced phase change from NiO to $Ni_2O_3$ for enhancing photocatalytic performance, Optik (Stuttg). 195 (2019) 163109. https://doi.org/10.1016/j.ijleo.2019.163109.

[103] C. Sun, L. Yan, B. Yue, H. Liu, Y. Gao, The modulation of metal–insulator transition temperature of vanadium dioxide: a density functional theory study, J. Mater. Chem. C. 2 (2014) 9283–9293. https://doi.org/10.1039/C4TC00778F.

[104] B.J. Boyle, E.G. King, K.C. Conway, Heats of Formation of Nickel and Cobalt Oxides (NiO and CoO) of Combustion Calorimetry, J. Am. Chem. Soc. 76 (1954) 3835–3837. https://doi.org/10.1021/ja01643a072.

[105] B.G. Baker, B.B. Johnson, G.L.C. Maire, Photoelectric work function measurements on nickel crystals and films, Surf. Sci. 24 (1971) 572–586. https://doi.org/10.1016/0039-6028(71)90282-2.

[106] E. Farzana, Z. Zhang, P.K. Paul, A.R. Arehart, S.A. Ringel, Influence of metal choice on (010) β-$Ga_2O_3$ Schottky diode properties, Appl. Phys. Lett. 110 (2017). https://doi.org/10.1063/1.4983610.

[107] K. Sato, Y. Yasumura, Study of forward I-V plot for Schottky diodes with high series resistance, J. Appl. Phys. 58 (1985) 3655–3657. https://doi.org/10.1063/1.335750.

[108] J.M. Dhimmar, H.N. Desai, B.P. Modi, The Effect of Interface States Density Distribution and Series Resistance on Electrical Behaviour of Schottky Diode, Mater. Today Proc. 3 (2016) 1658–1665. https://doi.org/10.1016/j.matpr.2016.04.056.

[109] J.H. Werner, H.H. Güttler, Barrier inhomogeneities at Schottky contacts, J. Appl. Phys. 69 (1991) 1522–1533. https://doi.org/10.1063/1.347243.

[110] T.-H. Yang, H. Fu, H. Chen, X. Huang, J. Montes, I. Baranowski, K. Fu, Y. Zhao, Temperature-dependent electrical properties of $\beta$-$Ga_2O_3$ Schottky barrier diodes on highly doped single-crystal substrates, J. Semicond. 40 (2019) 12801. https://doi.org/10.1088/1674-4926/40/1/012801.

[111] J.H. Werner, H.H. Güttler, Barrier inhomogeneities at Schottky contacts, J. Appl. Phys. 69 (1991) 1522–1533. https://doi.org/10.1063/1.347243.

[112] E. Arslan, Y. Badali, M. Aalizadeh, Ş. Altındal, E. Özbay, Current transport properties of (Au/Ni)/$HfAlO_3$/n-Si metal–insulator–semiconductor junction, J. Phys. Chem. Solids. 148 (2021) 109758. https://doi.org/https://doi.org/10.1016/j.jpcs.2020.109758.

[113] Ç.Ş. Güçlü, A.F. Özdemir, Ş. Altindal, Double exponential I–V characteristics and double Gaussian distribution of barrier heights in (Au/Ti)/$Al_2O_3$/n-GaAs (MIS)-type Schottky barrier diodes in wide temperature range, Appl. Phys. A. 122 (2016) 1032. https://doi.org/10.1007/s00339-016-0558-x.

[114] M.E. Coltrin, R.J. Kaplar, Transport and breakdown analysis for improved figure-of-merit for AlGaN power devices, J. Appl. Phys. 121 (2017) 55706. https://doi.org/10.1063/1.4975346.

[115] R.-S. Ki, J.-G. Lee, H.-Y. Cha, K.-S. Seo, The effect of edge-terminated structure for lateral AlGaN/GaN Schottky barrier diodes with gated ohmic anode, Solid. State. Electron. 166 (2020) 107768. https://doi.org/https://doi.org/10.1016/j.sse.2020.107768.

[116] S.K. Kim, W.-D. Kim, K.-M. Kim, C.S. Hwang, J. Jeong, High dielectric constant $TiO_2$ thin films on a Ru electrode grown at 250 °C by atomic-layer deposition, Appl. Phys. Lett. 85 (2004) 4112–4114. https://doi.org/10.1063/1.1812832.

[117] T.E. Taouririt, A. Meftah, N. Sengouga, M. Adaika, S. Chala, A. Meftah, Effects of high-k gate dielectrics on the electrical performance and reliability of an amorphous indium–tin–zinc–oxide thin film transistor (a-ITZO TFT): an analytical survey, Nanoscale. 11 (2019) 23459–23474. https://doi.org/10.1039/C9NR03395E.

[118] C. Dette, M.A. Pérez-Osorio, C.S. Kley, P. Punke, C.E. Patrick, P. Jacobson, F. Giustino, S.J. Jung, K.

Kern, TiO$_2$ Anatase with a Bandgap in the Visible Region, Nano Lett. 14 (2014) 6533–6538. https://doi.org/10.1021/nl503131s.

[119] P. Ahlberg, F.O.L. Johansson, Z.-B. Zhang, U. Jansson, S.-L. Zhang, A. Lindblad, T. Nyberg, Defect formation in graphene during low-energy ion bombardment, APL Mater. 4 (2016) 46104. https://doi.org/10.1063/1.4945587.

[120] H. Yuan, J. Su, R. Guo, K. Tian, Z. Lin, J. Zhang, J. Chang, Y. Hao, Contact barriers modulation of graphene/β-Ga2O3 interface for high-performance Ga$_2$O$_3$ devices, Appl. Surf. Sci. 527 (2020) 146740. https://doi.org/https://doi.org/10.1016/j.apsusc.2020.146740.

[121] H. Zhong, K. Xu, Z. Liu, G. Xu, L. Shi, Y. Fan, J. Wang, G. Ren, H. Yang, Charge transport mechanisms of graphene/semiconductor Schottky barriers: A theoretical and experimental study, J. Appl. Phys. 115 (2014) 13701. https://doi.org/10.1063/1.4859500.

[122] J.X. Ran, B.Y. Liu, X.L. Ji, A. Fariza, Z.T. Liu, J.X. Wang, P. Gao, T.B. Wei, Impact of graphene interlayer on performance parameters of sandwich structure Pt/GaN Schottky barrier diodes, J. Phys. D. Appl. Phys. 53 (2020) 404003. https://doi.org/10.1088/1361-6463/ab9a9b.

[123] M. Inaba, K. Suzuki, M. Shibuya, C.-Y. Lee, Y. Masuda, N. Tomatsu, W. Norimatsu, A. Hiraiwa, M. Kusunoki, H. Kawarada, Very low Schottky barrier height at carbon nanotube and silicon carbide interface, Appl. Phys. Lett. 106 (2015) 123501. https://doi.org/10.1063/1.4916248.

[124] J. Courtin, S. Le Gall, P. Chrétien, A. Moréac, G. Delhaye, B. Lépine, S. Tricot, P. Turban, P. Schieffer, J.-C. Le Breton, A low Schottky barrier height and transport mechanism in gold–graphene–silicon (001) heterojunctions, Nanoscale Adv. 1 (2019) 3372–3378. https://doi.org/10.1039/C9NA00393B.

[125] T. Takahashi, K. Sugawara, E. Noguchi, T. Sato, T. Takahashi, Band-gap tuning of monolayer graphene by oxygen adsorption, Carbon N. Y. 73 (2014) 141–145. https://doi.org/https://doi.org/10.1016/j.carbon.2014.02.049.

[126] A. Hussain, S. Ullah, M.A. Farhan, Fine tuning the band-gap of graphene by atomic and molecular doping: a density functional theory study, RSC Adv. 6 (2016) 55990–56003. https://doi.org/10.1039/C6RA04782C.

## Publications and conferences

- M. Labed, N. Sengouga, M. Labed, A. Meftah, S. Kyoung, H. Kim, Y.S. Rim, Modeling a Ni/$\beta$-Ga$_2$O$_3$ Schottky barrier diode deposited by confined magnetic-field-based sputtering, J. Phys. D Appl. Phys. 54 (2021) 115102, https://doi.org/ 10.1088/1361-6463/abce2c.

- M. Labed, N. Sengouga, M. Labed, A. Meftah, S. Kyoung, H. Kim, Y.S. Rim, Modeling and analyzing temperature-dependent parameters of Ni/$\beta$-Ga$_2$O$_3$ Schottky barrier diode deposited by confined magnetic field-based sputtering, Semicond. Sci. Technol. 36 (2021) 35020, https://doi.org/10.1088/1361-6641/.

- M. Labed, N. Sengouga, A. Meftah, M. Labed, S. Kyoung, H. Kim, Y.S. Rim, Leakage current modelling and optimization of $\beta$-Ga$_2$O$_3$ Schottky barrier diode with Ni contact under high reverse voltage, ECS J. Solid State Sci. Technol. 9 (2020) 125001, https://doi.org/10.1149/2162-8777/abc834.

- M. Labed, J.H. Park, A. Meftah, N. Sengouga, J.Y. Hong, Y.-K. Jung, Y.S. Rim, Low Temperature Modeling of Ni/ $\beta$-Ga$_2$O$_3$ Schottky Barrier Diode Interface, ACS Appl. Electron. Mater. 3 (2021) 3667–3673. https://doi.org/10.1021/acsaelm.1c00647.

- M. Labed, N. Sengouga, Y.S. Rim, Control of Ni/$\beta$-Ga$_2$O$_3$ Vertical Schottky Diode Output Parameters at Forward Bias by Insertion of a Graphene Layer, Nanomaterials. 12 (2022) 827. https://doi.org/10.3390/nano12050827.

- M. Labed. H. Kim, J. H. Park, M. Labed, A. Meftah, N. Sengouga, Y.S. Rim. Physical Operations of a Self-Powered IZTO/$\beta$-Ga$_2$O$_3$ Schottky Barrier Diode Photodetector. *Nanomaterials*. 12 (2022) 1061. https://doi.org/10.3390/nano12071061.

- M. Labed, A. Meftah, N. Sengouga, J. H. Park, S. Kyoung, H. Kim,  Y. S. Rim, Modeling temperature dependent Ni/$\beta$-Ga$_2$O$_3$ Schottky barrier diode interface properties, Materials Science and Engineering B, under review.

- 6th International Conference on Advances in Functional Materials (AFM2021) with oral presentation entitled: "Control of Schottky Barrier Height of Ni/$\beta$-Ga$_2$O$_3$ Schottky Barrier Diode by Insertion of Graphene Layer" February 15-17, 2021. Venue Sono Belle Jeju (formerly Daemyung Resort Jeju), South Korea.

- 8th International Conference on Materials Science and Nanotechnology for Next Generation with oral presentation entitled: " Modeling $Ni/\beta\text{-}Ga_2O_3$ Schottky Barrier Diode deposited by confined magnetic field based sputtering" July 14-16, 2021, Elazığ, Turkey.

- International Conference on Advanced Materials Science and Engineering and High-Tech Device Applications (ICMATSE2020) with oral presentation entitled: "Leakage Current Modelling and Optimization of $Ni/\beta\text{-}Ga_2O_3$ Schottky barrier Diode under High Reverse Voltage" October 02-04, 2020. Ankara, Turkey.

- International Conference on Advanced Materials Science and Engineering and High-Tech Device Applications (ICMATSE2020) with oral presentation entitled: "Open Circuit Voltage Improvement of a NiO/Si Heterojunction Solar Cell" October 02-04, 2020. Ankara, Turkey.

- 1st International Conference on Sustainable Energy and Advanced Materials (IC-SEAM'21)," Modelling $InZnSnO/\beta\text{-}Ga_2O_3$ Schottky barrier diode", April 21-22, 2021, Ouargla, ALGERIA (Virtual conference).

- 16th Conference on PhD Research in Microelectronics and Electronics (IEEE), Prime2021: "Modeling $Ni/\beta\text{-}Ga_2O_3$ SBD interface properties", 19 – 22 July 2021, Germany (Online event).

# Modeling a Ni/β-Ga$_2$O$_3$ Schottky barrier diode deposited by confined magnetic-field-based sputtering

**Madani Labed**[1] [ID]**, Nouredine Sengouga**[1] [ID]**, Mohamed Labed**[1]**, Afak Meftah**[1]**, Sinsu Kyoung**[3]**, Hojoong Kim**[2] **and You Seung Rim**[2] [ID]

[1] Laboratory of Semiconducting and Metallic Materials (LMSM), University of Biskra, Biskra 07000, Algeria
[2] Department of Intelligent Mechatronics Engineering and Convergence Engineering for Intelligent Drone, Sejong University, 209 Neungdong-ro, Gwangjin-gu, Seoul 05006, Republic of Korea
[3] Research and Development, Powercubesemi Inc., Sujeong-gu, Seongnam-si, Gyeonggi-do 13449, Republic of Korea

E-mail: n.sengouga@univ-biskra.dz and youseung@sejong.ac.kr

CrossMark

## Abstract

In this work, a detailed numerical simulation is carried out to model the current–voltage characteristics of a nickel/β-Ga$_2$O$_3$ Schottky barrier diode at different temperatures. These SBDs are produced using confined magnetic-field-based sputtering to deposit the nickel (Ni) Schottky contact of the diode. This method reduces the thickness of the defect area created by plasma and argon bombardment, and consequently, the electrical characteristics are less affected by temperature changes or annealing (i.e. the device is more stable). During annealing, Ni diffuses into β-Ga$_2$O$_3$. A model for this diffusion is proposed in this work, in which Ni diffusion reduces the defects produced by plasma and argon bombardment by filling the Ga vacancy. Furthermore, Ni diffusion produces a new interfacial compound, namely (Ni$_x$Ga$_{1-x}$)$_2$O$_3$ at the interface between the Ni and the β-Ga$_2$O$_3$. This new compound layer has different properties than those of β-Ga$_2$O$_3$, in particular, those of the bandgap and the affinity. Finally, the temperature-dependent current-density–voltage ($J$–$V$) characteristics are simulated, taking the proposed model into account. A good agreement with measured values is achieved, especially at low forward voltages, which demonstrates the soundness of the proposed model.

Keywords: Ni/β-Ga$_2$O$_3$ SBD, CMFS, defects, modeling, $J$–$V$ characteristics, temperature

(Some figures may appear in colour only in the online journal)

## 1. Introduction

Wide-bandgap compound semiconductors have made huge improvements to the extended functionality of both electronic and optoelectronic devices due to their high-voltage operation, fast-switching behavior, and thermal stability [1, 2]. Wide-bandgap materials, such as GaN, InGaN and SiC have been used in many applications in the last decade, in particular in nitrides. Recently, research has concentrated on ultra-wide bandgap (UWBG) semiconducting materials for which the energy gap exceeds 4 eV [3]. Several UWBG materials have attracted particular attention, including AlGaN, AlN,

diamond, and β-Ga$_2$O$_3$ [3]. β-Ga$_2$O$_3$ has excellent intrinsic properties such as a wide bandgap of ~4.8 eV, a high breakdown electric field of ~8 MV cm$^{-1}$, and a high saturation velocity of $1 \times 10^7$ cm s$^{-1}$ [3–5]. It is also a low-cost material and produced on a large scale, compared to GaN, InGaN and SiC [3, 5]. However, this material has the serious drawback of developing p-type [6, 7], thus hindering its application in bipolar devices (p–n junctions, bipolar junction transistor (BJT)) [5]. Currently, β-Ga$_2$O$_3$ is therefore mainly used in unipolar devices (Schottky barrier diodes (SBDs) [3, 8], metal oxide semiconductor field effect transistors (MOSFETs) [2], thin film transistors (TFTs) [9] and field emission devices

# Modeling and analyzing temperature-dependent parameters of Ni/$\beta$-Ga$_2$O$_3$ Schottky barrier diode deposited by confined magnetic field-based sputtering

**Madani Labed**[1] [ID], **Nouredine Sengouga**[1] [ID], **Mohamed Labed**[1], **Afak Meftah**[1], **Sinsu Kyoung**[3], **Hojoong Kim**[4] **and You Seung Rim**[2] [ID]

[1] Laboratory of Semiconducting and Metallic Materials (LMSM), University of Biskra, Biskra 07000, Algeria
[2] Department of Intelligent Mechatronics Engineering, and Convergence Engineering for Intelligent Drone, Sejong University, Seoul 05006, Republic of Korea
[3] Research and Development, Powercubesemi Inc., Sujeong-gu, Seongnam-si, Gyeonggi-do 13449, Republic of Korea
[4] George W. Woodruff School of Mechanical Engineering, Institute for Electronics and Nanotechnology, Georgia Institute of Technology, Atlanta, GA 30332, United States of America

E-mail: n.sengouga@univ-biskra.dz and youseung@sejong.ac.kr

## Abstract

In this work, the temperature-dependent parameters of Ni/$\beta$-Ga$_2$O$_3$ Schottky barrier diode (SBD) were analyzed and modeled. The simulation is to elucidate the physical phenomenon behind this temperature dependence. At room temperature, the deviation of SBD parameters from the ideal case is due to the Schottky barrier height ($\phi_B$) inhomogeneity. A model is developed for this inhomogeneity in which an interfacial defected layer (IDL) is formed. Defects (extrinsic states) are related to plasma and Ar atom bombardment used in the confined magnetic field-based sputtering to realize the Ni Schottky contact diffusion in $\beta$-Ga$_2$O$_3$. Ni diffuses, upon annealing, to compensate defects in this IDL. It was found that the Schottky barrier height ($\phi_B$) and threshold voltage ($V_{Th}$) decrease with increasing temperature. This decrease is related to intrinsic and extrinsic states (plasma and Ar bombardment). However, the ideality factor ($\eta$) increases which is related to the series resistance ($R_S$) increase. The increase is related to the interfacial layer and nickel resistance increase with increasing temperature.

Keywords: Ni/$\beta$-Ga$_2$O$_3$ SBD, temperature, inhomogeneity barrier height, traps, interface layer

(Some figures may appear in colour only in the online journal)

## 1. Introduction

Gallium oxide (Ga$_2$O$_3$), a transparent semiconducting oxide, attracted high interest for a wide range of applications, including solar-blind UV photodetectors, solar cells, sensors, metal-oxide-semiconductor-field effect transistors, thin-film transistors, and Schottky diodes [1–3]. Ga$_2$O$_3$ has six polymorphs ($\alpha, \beta, \gamma, \delta, \varepsilon$, and k) [4]. Monoclinic $\beta$-Ga$_2$O$_3$ is the most stable polymorph at high temperature and can be grown easily from the melt. These characteristics, in addition to its electrical and optical properties, have made $\beta$-Ga$_2$O$_3$ more attractive than other polymorphs. The basic optical properties

# Leakage Current Modelling and Optimization of *β-Ga₂O₃* Schottky Barrier Diode with Ni Contact under High Reverse Voltage

**Madani Labed,**[1] **Nouredine Sengouga,**[1,z] **Afak Meftah,**[1] **Mohamed Labed,**[1] **Sinsu Kyoung,**[2] **Hojoong Kim,**[3] **and You Seung Rim**[3,z]

[1]*Laboratory of Semiconducting and Metallic Materials (LMSM), University of Biskra 07000, Algeria*
[2]*Research and Development, Powercubesemi Inc., Sujeong-gu, Seongnam-si, Gyeonggi-do 13449, Republic of Korea*
[3]*Department of Intelligent Mechatronics Engineering, Sejong University, Gwangjin-gu, Seoul 05006, Republic of Korea*

The reverse leakage current under high reverse voltage of a Ni/*β-Ga₂O₃* Schottky barrier diode (SBD) is numerically modelled and compared to measurements. universal Schottky tunnelling, thermionic emission and image-force lowering were taken into account. Furthermore, when type conversion under high reverse voltage has occurred at the top interface between Ni and *β-Ga₂O₃* and the SBD behaved as P–i–N diode, band to band tunnelling is proposed in association with the usually used Selberherr's Impact ionization to model avalanche breakdown. The obtained breakdown voltage and specific on-resistance value are 434 V and 2.13 mΩ·cm², respectively, fairly close to measurement values of 440 V and 2.79 mΩ·cm². Optimization is performed based on the insertion of an intrinsic layer between Ni and the *β-Ga₂O₃* drift layer. It was found that 0.4 *μ*m gave better Baliga's figure of merit of 9.4810⁷ W·cm⁻² with breakdown voltage and specific on-resistance of 465 V and 2.28 mΩ·cm², respectively. Finally, a surface edge termination design based on TiO₂ insulator plate is adopted and the best obtained breakdown voltage, Baliga's figure of merit and specific on-resistance were 1466 V, 1.98 × 10⁹ W·cm⁻² and 1.98 mΩ·cm² respectively.
© 2020 The Electrochemical Society ("ECS"). Published on behalf of ECS by IOP Publishing Limited. [DOI: 10.1149/2162-8777/abc834]

In the last decade, interest in ultra-wide bandgap gallium oxide (*Ga₂O₃*), has increased significantly[1–3] due to several good properties. There are several types of *Ga₂O₃* polymorphs investigated in detail both experimentally and theoretically.[2] Among these polymorphs, monoclinic beta-gallium oxide (*β-Ga₂O₃*) is considered to be the most stable structure.[2] In addition to its ultra-wide bandgap, *β-Ga₂O₃* has tolerable electron mobility and leftover high breakdown field (≈8 MV·cm⁻¹).[3] The most important feature is its low cost and possibility of a large growth of bulk single crystals directly from melt.[2,4,5] However, this material has serious drawbacks for example poor thermal conductivity[2,6] and the difficulty of developing p-type.[7,8] These characteristics made *β-Ga₂O₃* suitable in most unipolar devices for example metal oxide field-effect transistor,[3] Thin film transistor,[9] photodetectors,[10] and Schottky barrier diode (SBD).[11] There are may reports of high breakdown voltage *β-Ga₂O₃* SBDs that are temperature dependent. Previous modeling studies on the leakage transport mechanisms in *β-Ga₂O₃* SBD have been proposed, including thermionic emission (TE) and thermionic field emission (TFE) considered for *β-Ga₂O₃* SBDs under high reverse voltage.[12,13] In addition, due to the presence of trap states located near the metal/*β-Ga₂O₃* interface, Zhou et al. used Poole–Frenkel emission mechanism to analyse the leakage current for Pt/($\overline{2}01$) *β-Ga₂O₃*.[14] Fu et al. used trap-assisted tunneling (TAT) mechanism for leakage current analysis of vertical ($\overline{2}01$) and (010) *Ga₂O₃* SBDs on EFG single-crystal substrates.[15] Li et al. included tunneling process, TE and TFE models under high reverse voltage in addition to the doping effect and image force lowering (IFL) model.[12] Hu et al.[16] studied the reverse current emission mechanism of the Mo/*β-Ga₂O₃* SBD through the temperature dependent current-voltage (I–V) characteristics from 298 to 423 K. The variation of reverse current with the electric field indicates that the Schottky emission is the dominant carrier transport mechanism under reverse bias rather than the Frenkel–Poole trap-assisted emission model. Other work combined all the mentioned models.[17] It is well known that under high reverse voltage an inversion layer at the surface of the semiconductor near the front contact is formed[18–20] which inevitably has an effect on the leakage current of the SBD.

In this work, we propose a new consideration of leakage models in *β-Ga₂O₃* including band to band transport model (BBT) andthe inversion layer formation between Ni and (001) *β-Ga₂O₃* under high

reverse voltage. The BBT model associated with the Selberherr's Impact ionization (SELB) model usually used for avalanche breakdown, gives good agreement with current-voltage measurement. Furthermore, optimizations in the leakage current, breakdown voltage and specific on-resistance are carried out with the insertion of an intrinsic *β-Ga₂O₃* layer at the interface between Ni and Si-doped *β-Ga₂O₃*, and by adopting a TiO₂ insulator plate as edge termination.

## SBD Structure and Modelling

The simulated *β-Ga₂O₃* SBD was fabricated on 650 *μ*m Sn doped (001) *β-Ga₂O₃* ($N_d - N_a = 1 \times 10^{18}$ cm⁻³) and 10 *μ*m Si-doped (001) *β-Ga₂O₃* ($N_d - N_a = 3 \times 10^{16}$ cm⁻³) as a drift layer, this epitaxial layer was deposited by halide vapour phase epitaxy (HVPE). Then, a Ti/Au electrode at the bottom of *β-Ga₂O₃* is deposited by an E-beam evaporation method. The Ni layer (300 nm) was deposited on the top of the drift layer using confined magnetic field-based spurting. This technique is based on the exposed the surface of *β-Ga₂O₃* over the plasma and Ar bombardment. Finally, the whole structure was annealed at 400 °C. A simple schematic illustration of the *Ni/β-Ga₂O₃* SBD is shown in Fig. 1. The electrical current density-voltage (J–V) characteristics were measured by a semiconductor analyser and a source meter (4200A-SCS parameter analyser and 2410 source meter, Keithley). Further details are given in Ref. 11.

To model the leakage current under high reverse bias, physical expressions of each model included in the simulation which was performed by SILVACO-Atlas commercial simulator are detailed. The simple simulated structure and its doping profile generated by the simulation software are presented in Figs. 2a and 2b respectively.

Tunnelling is considered using universal Schottky Tunneling (UST) model and the tunneling current is given by[17,21,22]:

$$J_T = \frac{A^* T_L}{K_B} \int_\epsilon^\infty \Gamma(E') \ln\left(\frac{1 + F_s(E')}{1 + F_m(E')}\right) dE' \quad [1]$$

The tunnelling generation rate ($G_T$) is given by[21,22]:

$$G_T = \frac{1}{q} \nabla J_{TE} \quad [2]$$

where $A^*$, $T_L$, $K_B$, ∈, $F_s(E')$ and $F_m(E')$ are effective Richardson's coefficient (41.11 $Acm^{-2}K^{-2}$), lattice temperature, Boltzmann constant, electrons energy, and Maxwell- Boltzmann distribution in the

ᶻE-mail: n.sengouga@univ-biskra.dz

*Article*

# Control of Ni/β-Ga$_2$O$_3$ Vertical Schottky Diode Output Parameters at Forward Bias by Insertion of a Graphene Layer

Madani Labed [1], Nouredine Sengouga [1] and You Seung Rim [2,*]

[1]  Laboratory of Semiconducting and Metallic Materials (LMSM), University of Biskra, Biskra 07000, Algeria;
    madani.labed@univ-biskra.dz (M.L.); n.sengouga@univ-biskra.dz (N.S.)
[2]  Department of Intelligent Mechatronics Engineering and Convergence Engineering for Intelligent Drone,
    Sejong University, Seoul 05006, Korea
*  Correspondence: youseung@sejong.ac.kr

**Abstract:** Controlling the Schottky barrier height ($\phi_B$) and other parameters of Schottky barrier diodes (SBD) is critical for many applications. In this work, the effect of inserting a graphene interfacial monolayer between a Ni Schottky metal and a β-Ga$_2$O$_3$ semiconductor was investigated using numerical simulation. We confirmed that the simulation-based on Ni workfunction, interfacial trap concentration, and surface electron affinity was well-matched with the actual device characterization. Insertion of the graphene layer achieved a remarkable decrease in the barrier height ($\phi_B$), from 1.32 to 0.43 eV, and in the series resistance ($R_S$), from 60.3 to 2.90 mΩ.cm$^2$. However, the saturation current ($J_S$) increased from $1.26 \times 10^{-11}$ to $8.3 \times 10^{-7}$ (A/cm$^2$). The effects of a graphene bandgap and workfunction were studied. With an increase in the graphene workfunction and bandgap, the Schottky barrier height and series resistance increased and the saturation current decreased. This behavior was related to the tunneling rate variations in the graphene layer. Therefore, control of Schottky barrier diode output parameters was achieved by monitoring the tunneling rate in the graphene layer (through the control of the bandgap) and by controlling the Schottky barrier height according to the Schottky–Mott role (through the control of the workfunction). Furthermore, a zero-bandgap and low-workfunction graphene layer behaves as an ohmic contact, which is in agreement with published results.

**Keywords:** SBD; β-Ga$_2$O$_3$; electron-beam evaporation; interfacial traps; graphene; workfunction; bandgap

*Article*

# Physical Operations of a Self-Powered IZTO/β-Ga$_2$O$_3$ Schottky Barrier Diode Photodetector

**Madani Labed** [1], **Hojoong Kim** [2,3], **Joon Hui Park** [2], **Mohamed Labed** [4], **Afak Meftah** [1], **Nouredine Sengouga** [1] **and You Seung Rim** [2,*]

[1] Laboratory of Semiconducting and Metallic Materials (LMSM), University of Biskra, Biskra 07000, Algeria; madani.labed@univ-biskra.dz (M.L.); af.meftah@univ-biskra.dz (A.M.); n.sengouga@univ-biskra.dz (N.S.)
[2] Department of Intelligent Mechatronics Engineering, and Convergence Engineering for Intelligent Drone, Sejong University, Seoul 05006, Korea; hkim3023@gatech.edu (H.K.); julia980406@gmail.com (J.H.P.)
[3] George W. Woodruff School of Mechanical Engineering, Institute for Electronics and Nanotechnology, Georgia Institute of Technology, Atlanta, GA 30332, USA
[4] High Collage of Food Sciences and Food Industries, Algiers 16200, Algeria; labed@essaia.dz
* Correspondence: youseung@sejong.ac.kr

**Abstract:** In this work, a self-powered, solar-blind photodetector, based on InZnSnO (IZTO) as a Schottky contact, was deposited on the top of Si-doped β-Ga$_2$O$_3$ by the sputtering of two-faced targets with InSnO (ITO) as an ohmic contact. A detailed numerical simulation was performed by using the measured J–V characteristics of IZTO/β-Ga$_2$O$_3$ Schottky barrier diodes (SBDs) in the dark. Good agreement between the simulation and the measurement was achieved by studying the effect of the IZTO workfunction, β-Ga$_2$O$_3$ interfacial layer (IL) electron affinity, and the concentrations of interfacial traps. The IZTO/β-Ga$_2$O$_3$ (SBDs) was tested at a wavelength of 255 nm with the photo power density of 1 mW/cm$^2$. A high photo-to-dark current ratio of $3.70 \times 10^5$ and a photoresponsivity of 0.64 mA/W were obtained at 0 V as self-powered operation. Finally, with increasing power density the photocurrent increased, and a 17.80 mA/W responsivity under 10 mW/cm$^2$ was obtained.

**Keywords:** IZTO/β-Ga$_2$O$_3$ Schottky diode; solar-blind; self-powered; photodetector; modeling

Madani Labed
Laboratory of Semiconducting and Metallic Materials
Physics
Labed Elhaddi street bouchagroune, Biskra, Algeria
07022 biskra
Algeria

Jeju, South Korea, 23/Apr/2021

## To Whom It May Concern

Dear Madam or Sir,

This is to certify that **Madani Labed** participated at Advances in Functional Materials 2021.

Madani Labed is author/co-author of the following accepted contribution(s):

**Abstract ID:** 120
Control of Schottky barrier height of Ni/β-Ga2O3 Schottky barrier diode by insertion of graphene layer.
**Author(s):** Labed, Madani; Sengouga, Nouredine; Meftah, Afak; Rim, You Seung
**Presenting Author:** Labed, Madani
**Conference Track:** Symposium 7: Low dimensional, Nano and 2D materials
**Status:** This abstract has been accepted for oral presentation
**Session Details:** ORAL-6, **Time:** Tuesday, 16/Feb/2021: 1:30pm - 3:30pm, **Location:** Ruby-1

PS: If no session details are presenting, it means authors didn't show up or didn't present their work at AFM-21.

With best regards,
Organizing Committee
Advances in Functional Materials Conference 2021
Sono Belle (formerly Daemyung Resort) Jeju, South Korea
https://functionalmaterials.org/afm-2020/
afm2021@functionalmaterials.org

**MSnG-2021**

MATERIALS SCIENCE AND NANOTECHNOLOGY
FOR NEXT GENERATION

# CERTIFICATE
## OF ATTENDANCE

This is to certify that

## Madani LABED

### Has attended
8th international conference on materials science and nanotechnology
for next generation held in Elazığ, Turkey.
14-16 July 2021

Prof. Dr. Fahrettin YAKUPHANOĞLU

# ICMATSE

**ICMATSE 2020 International Conference On Advanced Materials Science & Engineering And High Tech Device Applications**

## Certificate of Participation

### This is to certify that
### Madani LABED

**participated at ICMATSE, and made a presentation entitled**
**ID61 - Leakage Current Modelling and Optimization of Ni/ β-Ga₂O₃**
**Schottky Barrier Diode Under High Reverse Voltage**
*hereby the contributions awarded with this certificate.*

**Prof. Dr. Hakan ATES**
*Gazi University*
*Chairman*

**Assoc. Prof. Dr. Ersin BAHCECI**
*İskenderun Technical University*
*Chairman*

121

# ICMATSE

ICMATSE 2020 International Conference On Advanced Materials Science & Engineering And High Tech Device Applications

## Certificate of Participation

This is to certify that
**Madani LABED**

participated at ICMATSE, and made a presentation entitled
*ID62 - Open Circuit Voltage Improvement of A NiO/Si Heterojunction Solar Cell*

hereby the contributions awarded with this certificate.

**Prof. Dr. Hakan ATES**
*Gazi University*
*Chairman*

**Assoc. Prof. Dr. Ersin BAHCECI**
*İskenderun Technical University*
*Chairman*

122

# Modeling Ni/β-$Ga_2O_3$ SBD interface properties

Madani Labed
Laboratory of Semiconducting and
Mettalic Materials
University of Biskra,07000
Algeria
*madani.labed@univ-biskra.dz*

Nouredine Sengouga
Laboratory of Semiconducting and
Mettalic Materials
University of Biskra,07000
Algeria
n.sengouga@univ-biskra.dz

Afak Meftah
Laboratory of Semiconducting and
Mettalic Materials
University of Biskra,07000
Algeria
af.meftah@univ-biskra.dz

Jun Hui Park
Department of Intelligent
Mechatronics Engineering, and
Convergence Engineering for
Intelligent Drone
Sejong university
Seoul 05006, Republic of Korea
julia980406@gmail.com

Sinsu Kyoung
Research and Development,
Powercubesemi Inc
Sujeong-gu, Seongnam-si,
Gyeonggi-do 13449
Republic of Korea
sskyoung@powercubesemi.com

Hojoong Kim
Department of Intelligent
Mechatronics Engineering, and
Convergence Engineering for
Intelligent Drone
Sejong university
Seoul 05006, Republic of Korea
hojoongkim@sejong.ac.kr

You Seung Rim
Department of Intelligent
Mechatronics Engineering, and
Convergence Engineering for
Intelligent Drone
Sejong university
Seoul 05006, Republic of Korea
youseung@sejong.ac.kr

*Abstract*— In this work, Ni/β-$Ga_2O_3$ Schottky diode deposited by electron-beam evaporation was studied. A detailed numerical simulation is carried out to reproduce the current-voltage measurement of Ni/β- $Ga_2O_3$ Schottky diode and extract the Ni/β- $Ga_2O_3$ interface properties. For more agreement between simulation and measurement the effect of Ni workfunction, Si-doped β-$Ga_2O_3$ surface electron affinity and traps concentration were studied.

*Keywords— β-$Ga_2O_3$, SBD, Interface, Traps, Silvaco-Atlas*

## I. INTRODUCTION

Gallium oxide ($Ga_2O_3$) is a new oxide semiconductor material with a long rich history [1]. Pioneer studies were

effect on the electrical characteristics of Ni/β-$Ga_2O_3$ SBD were studied to reproduce the current-voltage measurement.

## II. DEVICE STRUCTURE AND SIMULATION

The β-$Ga_2O_3$ Schottky barrier diode (SBD) structure, based on an experimental structure[16], is investigated. It consists of a 300 nm thick Nickel (its work function is $\Phi_m$=5.25 eV), a Si-doped β-$Ga_2O_3$ layer deposited on a Sn-doped β-$Ga_2O_3$ substrate by halide vapor phase epitaxy (HVPE) which is used as a drift layer in this SBD. This layer is used due to its high purity and provides a low resistance, a low on-resistance and a high breakdown voltage. Then, 300 nm Nickel layer deposited on the top of the drift layer by electron beam evaporation, followed by annealing at 400 ℃[16]. The electrical current